Stratification and mixing in the Rhine Region of Freshwater Influence

Analysing two parallel transects

MASTER OF SCIENCE THESIS
Section of Environmental Fluid Mechanics
Department of Hydraulic Engineering
Faculty of Civil Engineering & Geosciences
Delft University of Technology

In association with:
Port of Rotterdam Authority, Projectorganisatie Maasvlakte 2
Deltares, Zee- en Kust systemen
NIOZ Royal Netherlands Institute for Sea Research

AUTHOR
S. Rijnsburger

COMMITTEE MEMBERS
Prof. Dr. J.D. Pietrzak
Dr. Ir. B.C. van Prooijen
Prof. Ir. T. Vellinga
Dr. Ir. G.J. de Boer
Dr. O. van Tongeren
Ir. W. G. Borst
Ir. C. M. van der Hout

May, 2014

Abstract

The Rhine River and the Meuse River discharge into the southern North Sea, and form the Rhine Region of Fresh Water Influence (ROFI) in front of the Dutch coast. A complex hydrodynamic system is generated, dominated by mixing from strong tides, wind and waves and the stratifying influence of the freshwater and solar heating. This influences the distribution and dynamics of fine sediments. A proper understanding of the system is required to evaluate the effects of human interferences, such as the dredging for Maasvlakte 2. Previous years more insight is gained into the interaction between the tide and the stratification by numerical modelling (De Boer et al., 2008). Furthermore, various measurement campaigns are carried out to determine the effect of dredging activities for Maasvlakte 2.

This Master Thesis presents the analysis of a unique in-situ dataset focused on the different cross- and alongshore processes which induce the onset and breakdown of stratification. The aim of this study is to gain more insight into the complex four dimensional nature of the Rhine ROFI, in order to generate a better understanding of the behaviour of Suspended Particluate Matter (SPM). In October 2011 the Port of Rotterdam Authority (PoR) and NIOZ (Royal Netherlands Institute for Sea Research) sailed simultaneously on two parallel cross-shore transects in order to conduct measurements, one near Egmond and one near Wijk aan Zee. Salinity, temperature, SPM and velocities were measured. The advantage of measuring along two transects is the extra dimension in alongshore direction. Therefore, a dataset is obtained allowing analysis in four dimensions. In the previous years the four dimensional nature of the ROFI has only been studied with numerical modelling. However, data analysis was only performed with data from a single mooring or a single transect, both of which do not give spatial information in cross- and alongshore direction.

The contribution of alongshore advection and straining is investigated with a simplified form of the three-dimensional Potential Energy Anomaly Equation (PEA) (De Boer et al., 2008), influenced by wind, waves and tide. Tidal analysis is used to investigate the presence of ellipses, which indicate the presence of the plume.

After analysis it has become clear that the Northern transect is far more stratified than the expected. It was anticipated that the waters this far north were well-mixed. Instead it is shown that the Northern transect is even more stratified than the Southern transect. The simplified three-dimensional Potential Energy Anomaly analysis shows that cross-shore straining is the dominant process inducing stratification and mixing. Although the other cross- and alongshore processes are also observed and these prove significant as well. However, the alongshore advection works different than expected; it enhances stratification during ebb instead of during flood. This is the result of the more stratified Northern transect in comparison with the more homogeneous Southern transect. Tidal ellipses are observed in front of the coast. The ellipses show that the state of the water column is spring-like, stratification is yet observed.

Using two vessels to obtain information in four dimensions is on the verge of what is currently possible with the ships available to the Dutch community. This first measurement in four dimensions with two vessels and using the three-dimensional Potential Energy Anomaly Equation has led to more insights. This study highlights the dynamic and unpredictable behaviour of the Rhine ROFI, as the measurements have led to surprising outcomes.

Acknowledgements

This Master Thesis has been carried out as the final part of the Master Hydraulic Engineering at the Faculty of Civil Engineering and Geoscience, Delft University of Technology. The project has been funded by the Port of Rotterdam Authority in the context of the Maasvlakte 2 project. The project has been carried out at the offices of the Port of Rotterdam Authority and Deltares. In-situ data is used from both the Port of Rotterdam Authority and NIOZ. The collaboration between Delft University, the Port of Rotterdam Authority, Deltares and NIOZ gave me the opportunity to develop my knowledge, learned me to approach problems from different viewpoints and made me enthusiastic about the subject.

I would like to thank my graduation committee for their supervision, advice and enthusiasm during my research. Everyone encouraged me in their own way and were really helpful. My expressions of gratitude go to Prof. dr. J. D. Pietrzak who was always very interested in my work, encouraged me, helped me with writing and guided me through the entire project. I want to thank dr. ir. G.J. de Boer for his valuable input, his advice to prioritize, his clear and enthusiastic explanations and his passion for the Rhine ROFI. I would like to thank dr. O. van Tongeren for being critical, always being there to help and encouraging me to think deeper and from different perspectives. I really appreciate the critical questions from ir. W.G. Borst and his knowledge on many different fields.

I look back on an interesting trip to Brussel with ir. W.G. Borst and dr. O. van Tongeren who invited me to join them for a meeting for the MoS^2 project. Ir. C. van der Hout thanks you for using your data and giving very useful feedback and advice for my report and project. My appreciations go to dr. ir. B.C. van Prooijen for his help, useful remarks and making sure I kept to the schedule. In addition I would like to thank Prof. ir. T. Vellinga for his interest and input.

Finally, I would like to thank the Port of Rotterdam Authority and Deltares for providing me with an inspiring working environment. Finally, I want to show my expressions of thanks to L. Keijzer for his editorial advices. I look back on an interesting and valuable experience.

Delft, May 2014

S. Rijnsburger

Contents

Abstract iii

Acknowledgements v

Framework 1

1 Introduction 2

2 Theoretical Background 8
2.1 Introduction . . . 8
2.2 Rhine ROFI . . . 8
2.3 Potential Energy Anomaly . . . 10
2.4 Tide . . . 11
2.5 Wind . . . 15
2.6 Waves . . . 18

3 Methodology 21
3.1 Introduction . . . 21
3.2 Measurements . . . 21
3.3 Potential Energy Anomaly Analysis . . . 36
3.4 Tidal Analysis . . . 42

4 Results 45
4.1 Introduction . . . 45
4.2 Velocity distribution . . . 45
4.3 Salinity Distribution . . . 58
4.4 Temperature . . . 63
4.5 Potential Energy Anomaly Analysis . . . 65
4.6 Suspend Particulate Matter . . . 75

5 Discussion 78

6 Conclusions and recommendations 86

A Mathematical support 88
A.1 Steady-state equations/Navier-Stokes Equations . . . 88
A.2 Heaps . . . 88
A.3 Prandle . . . 89
A.4 Wave Theory . . . 91

B Snapshot of the entire dataset of the Port of Rotterdam Authority 93
B.1 Scatter Plots . . . 93

C Measurement Campaign Port of Rotterdam Aurthority 102

D Supporting figures 109

Bibliography **109**

Framework

The Maasvlakte has been extended seawards by the Port of Rotterdam Authority (PoR). This extension, the Maasvlakte 2, is for deep water port facilities and is located between the mouths of the Rotterdam New Waterway and the Haringvliet, where the freshwater of the Rhine-Meuse system is discharged into the Southern North Sea. The Rhine Region of Fresh Water Influence (ROFI) is created (e.g. Souza and Simpson (1997)). For the construction of Maasvlakte 2 an amount of 240 million m^3 of sand was required. This sand was excavated from a pit situated off the 20 meter depth contour away from the Rotterdam Harbour entrance. Possible effects of the construction of Maasvlakte 2 are investigated and written down in an environmental impact assessment.

The extracted sand contains fines which are released by the sand mining activities and come into the water column as suspended particulate matter (SPM). The increase of SPM in the water column will lead to an increase of turbidity. It influences the biotic environment and is therefore the subject of interest. PoR is interested in the effects of sand mining and construction activities on the distribution of SPM. Therefore, they started a monitoring programme, where hydrodynamics, water quality and ecological parameters were determined by means of spot measurements by ship surveys.

The in-situ measurements were extended by numerical modelling. The project Model Supported Monitoring of SPM (MoS^2) was started in 2009 to obtain more insight into temporal and spatial patterns of SPM concentrations. The MoS^2 project was carried out by Deltares and combines information from different observational data sets, with a numerical model for the hydrodynamics and for the transport model of SPM. The aim of this project was to present a clear picture of the distribution of SPM before, during and after construction of Maasvlakte 2.

The MoS^2 project was completed in December 2013. During the last few years, the PoR has gained more insight into the collected data, the impact of the Maasvlakte 2, the results of the numerical modeling and the distribution of SPM. Still, many questions are not answered yet. During MoS^2 the numerical model was adapted and improved. Still bias was observed between model results and observations (van Tongeren, pers. comm) . The model overestimate SPM at the surface and underestimate SPM near the bottom, with respect to the measured data. Several physical processes in the Dutch coastal zone determine the SPM distribution that might be able to explain this bias.

To improve the numerical modelling of the southern North Sea a better understanding of this system needs to be established. Therefore, this project has been carried out together with PoR and Deltares in order to improve our understanding of the Rhine ROFI and to gain more insight into the distribution of SPM along the Dutch coast. The study presented here is implemented in the context of the Maasvlakte 2.

Chapter 1

Introduction

Rivers release large quantities of fresh water into coastal seas and oceans. In the Northern Hemisphere the Earth's rotation causes the fresh water discharge to turn to the right upon entering the open sea, forming a downstream plume (e.g. Chao and Boicourt (1986)). River plumes are also referred to as Regions of Fresh water Influence (ROFI), a term introduced by Simpson et al. (1993). Simpson (1997) introduced a formal definition of these ROFI's as "the region between the shelf sea regime and the estuary where the local input of freshwater buoyancy from the coastal source is comparable with, or exceeds, the seasonal input of buoyancy as heat which occurs all over the shelf". The fresh water outflow acts in favour of stratification. The competition between stratifying and stirring processes determines the variation of the ROFI's in time and space. This interaction together with the shape of the receiving basin determines the evolution of the ROFI. It determines whether the ROFI forms downstream of the river mouth as happens for the Rhine ROFI, or whether it fills up the basin, as in the case of the Po river, as it discharges into the Adriatic Sea. These topographic constrains are discussed by Simpson (1997).

The Rhine River and the Meuse River discharge into the Southern North Sea creating the Rhine ROFI in front of the Dutch coast (figure 1.1). A complex hydrodynamic system is generated, where strong tides interact with wind, waves and buoyancy input. An average quantity of 2300 m^3/s is discharged through the Rotterdam Waterway and the Haringvliet into the Southern North Sea, forming a 20 to 40 km wide plume, which extends 100 km northwards (De Ruijter et al., 1997). The Rhine ROFI switches between a well-mixed and a stratified state as a result of competition between different processes. The system acts like a classical ROFI, but it is highly dominated by friction and tides. The strongest stratification is observed at 3 to 5 km from the shoreline (De Ruijter et al., 1997), at the same location where Giessen et al. (1990) found maximum values for coastal current velocities. This observation is explained by the higher mixing energy due to the wind, waves and tide as the coast is approached.

In the last few decades, more insight has been gained into the hydrodynamics of the Rhine ROFI and different theories have been developed to describe the interaction between the tide and stratification. Simpson et al. (1993) showed that the system switched between a stratified and a mixed ROFI during the fortnightly spring-neap tidal cycle. During spring tide with increased stirring energy, a well-mixed water column is observed. However, during neap tide, when the kinetic energy is low, the ROFI shows more stratification. During these stratified conditions, another phenomenon is observed that causes mixing on a semi-diurnal time scale. In addition to the mean stratification a semi-diurnal signal of stratification and mixing is present. The pycnocline causes a partial decoupling of the water column, resulting in cross-shore tidal currents in the Rhine ROFI as described by Visser et al. (1994). These cross-shore currents act on the horizontal density gradient through a process known as tidal straining Simpson et al. (1990), which is differential advection.

Visser et al. (1994) investigated the vertical structure of tidal currents in the Rhine ROFI. They found significant differences in structure between stratified and well-mixed conditions. The tide in the North Sea is governed by a Kelvin wave propagating along the Dutch coast. In the case

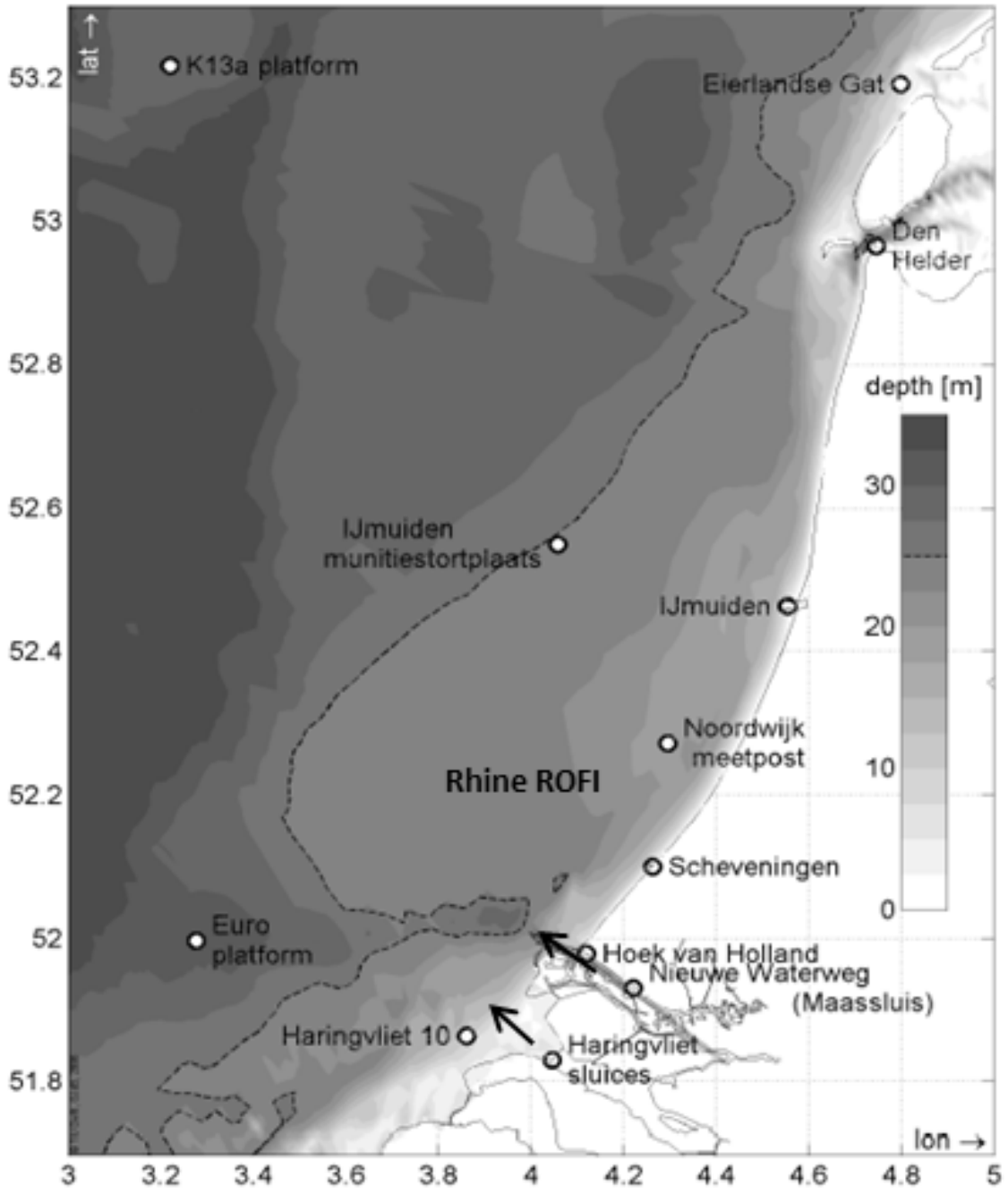

Figure 1.1: Overview of the Rhine ROFI, where the Rhine water discharges into the North Sea at Hoek van Holland and the Harinvliet sluices. The ROFI turns towards the right, flowing northwards and it stretches alongshore to Den Helder. Figure by De Boer (2009)

of well-mixed waters the tides are rectilinear, with the currents propagating in the alongshore direction on the ebb and the flood. Therefore during well-mixed conditions there is negligible interaction between the alongshore tidal currents and the cross-shore density gradients. However during stratified conditions, the tidal ellipses counter rotate between the surface and the bed, causing cross-shore currents. The magnitude of these cross-shore currents was almost 40 percent of the alongshore currents. The direction of the currents at the surface and near the bottom of the Rhine ROFI changes during the ebb-flood tidal cycle due to the counter rotating tidal ellipses. This leads to cross-shore currents that are directed offshore at the surface and onshore at the bed from low

water (LW) to high water (HW) and in the opposite directions from high water (HW) to low water (LW) (see figure 1.2). Simpson and Souza (1995) were the first to make the connection between tidal straining theory and the cross-shore velocity shear during stratified conditions in the Rhine ROFI.

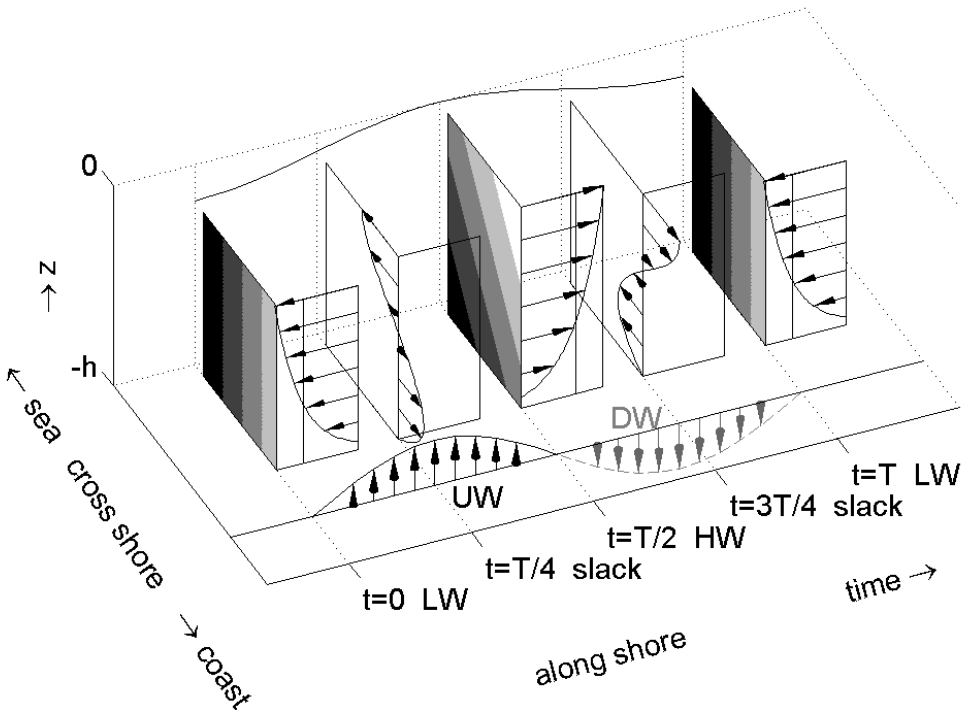

Figure 1.2: Concept of cross-shore tidal straining in the Rhine ROFI (Simpson and Souza, 1995). Figure by De Boer (2009)

The magnitude and direction of the wind is an important factor with respect to ROFI's. Different studies showed the influence of wind on the position of the river plume (e.g. Berdeal et al. (2002), Fong and Geyer (2002), Pietrzak and De Boer (in prep.), Van Wiechen (2011)). The importance of wind along the Dutch coast was first investigated by Pietrzak and de Boer (pers. comm) using the idealised model of De Boer et al. (2006). They explored the response of the Rhine ROFI to different wind directions and magnitudes. These authors found that the Rhine ROFI responded to wind in accordance with Ekman dynamics (Pietrzak and De Boer, in prep.). This work was extended in the Master's thesis by Van Wiechen (2011) who investigated the competition of the wind with the ebb-flood tidal cycle in the Rhine ROFI during neap tide. He used the MoS^2 model, a more realistic model set-up of the southern North Sea, to investigate the response of the plume to different wind directions and magnitudes. This study shows a rapid response to the wind, which is different for each wind direction.

Potential Energy Anomaly

Potential energy has been used in the past to study the onset and breakdown of stratification. Simpson and Hunter (1974) used a potential energy criterion to define the position of fronts in the Irish Sea. Within this study they derived a widely used criterion, h/u^3, for the formation of fronts. In this criterion h is the water depth and u is the surface tidal velocity amplitude. Since then, the use of potential energy has been applied by others within this field. Simpson and Bowers (1981) investigated the influence of the competing factors controlling stratification and mixing, by taking changes in potential energy relative to the well-mixed condition as a key indicator. Consequently, they introduced a scalar parameter, φ [J/m^3], the potential energy anomaly. It is defined as the

depth averaged potential energy required to obtain a well-mixed water column

$$\varphi = \frac{1}{H}\int_{-h}^{\eta}(\overline{\rho}-\rho)gzdz \tag{1.1}$$

where $H = h + \eta$ is the total water depth [m], η is the free surface [m], h the distance between the bed and the mean water level [m], g is the gravitational acceleration (9,81 m^2/s), z is the depth interval [m], ρ is the water density [kg/m^3] and $\overline{\rho}$ the depth averaged density. φ defines the actual state of the water column. The potential energy anomaly equation is the change of φ over time [W/m^3],

$$\frac{\partial\varphi}{\partial t} = \frac{g}{H}\int_{-h}^{\eta}\frac{\partial(\overline{\rho}-\rho)}{\partial t}zdz \tag{1.2}$$

It gives information on the processes of mixing and stratification over the water column. De Boer et al. (2008) concluded from earlier observations (Van Alphen et al., 1988; Simpson and Souza, 1995) that both cross-shore and along-shore processes were present in the Rhine ROFI at the same time, inducing stratification. To get a better impression of the contribution of these processes De Boer et al. (2008) derived the potential energy anomaly equation suitable for three-dimensional flows.

Suspended Particulate Matter

Insight into the distribution of SPM is of importance for the definition of ecosystems as SPM influences light penetration and therefore the primary growth of algae (phytoplankton). Various studies were focused on the influence of ROFI's on the distribution of SPM. Numerical modelling (Geyer, 1993) showed that stratification shuts down turbulence at the pycnocline. This causes SPM to sink, such that SPM is found beneath the thermocline. Burchard and Baumert (1998) elaborated on this topic. De Nijs et al. (2010, 2011) was the first who used in-situ data, collected at the Rotterdam Waterway, to show this mechanism. Pietrzak et al. (2011) used remote sensing images to investigate the distribution of surface SPM in the southern North Sea. They concluded that haline stratification plays an important role with respect to surface SPM. When the region is stratified, low values of surface SPM are observed. During periods with high turbulent kinetic energy high surface SPM concentrations are found instead. Moreover, Souza et al. (2007) found higher levels of SPM beneath the pycnocline during stratified conditions in the North-West European Shelf. Their numerical model study showed a clear seasonal variation, a clear tidal signal in the spatial distribution and re-suspension of SPM. As follows from previous research stratification seems to have an influence on the distribution of SPM (i.e. where the particles are located within the water column).

Port of Rotterdam Authority & NIOZ

The distribution of SPM along the Dutch coast has been the subject of intense fieldwork by the Port of Rotterdam Authority (PoR) as part of the Maasvlakte 2 project. As a result a large scale dataset is available. In order to interpret this dataset it is important to understand the background of the physical processes controlling the flow and therefore the distribution of SPM along the Dutch coast. Many factors in the Dutch coastal region influence this distribution, i.e. fresh river discharge, tide, wind, waves and heating up of the surface by the sun (figure 1.3). Within the context of the Maasvlakte 2 project Smolders (2011) analysed a sub-set of the large in-situ dataset. The focus of his research was on the development and breakdown of stratification near Noordwijk. He showed the importance of tidal straining in front of the Dutch coast for the onset and breakdown of stratification, by using the three-dimensional Potential Energy Anomaly equation in the cross-shore direction. Furthermore, he introduced a first suggestion with respect to the distribution of SPM. He stated that the observed movement of a SPM cloud and the movement of a freshwater bulge in combination with the measured tidal currents indicate the presence of the upwelling and downwelling mechanisms. Upwelling and downwelling as a result of tidal straining as explained by De Boer et al. (2009).

In addition NIOZ (Royal Netherlands Institute for Sea Research) is interested in the distribution of SPM as well. They implemented a measuring campaign in front of the North Holland coast, as part of the Building with Nature research programme, with the aim to define the annual net transport of SPM along the Dutch coast. Within this context Van der Hout et al. (subm.) observed hotspots of SPM at different locations far downstream from the river mouth. As a result of the findings of Van der Hout et al. (subm.) and Smolders (2011) the PoR and NIOZ implemented a joint measurement campaign in front of the North Holland coast during Autumn 2011. Their objective was to understand the SPM hotspots and the distribution of SPM along the Dutch coast. This thesis connects both studies and uses the obtained dataset by PoR and NIOZ to meet the aim of this study.

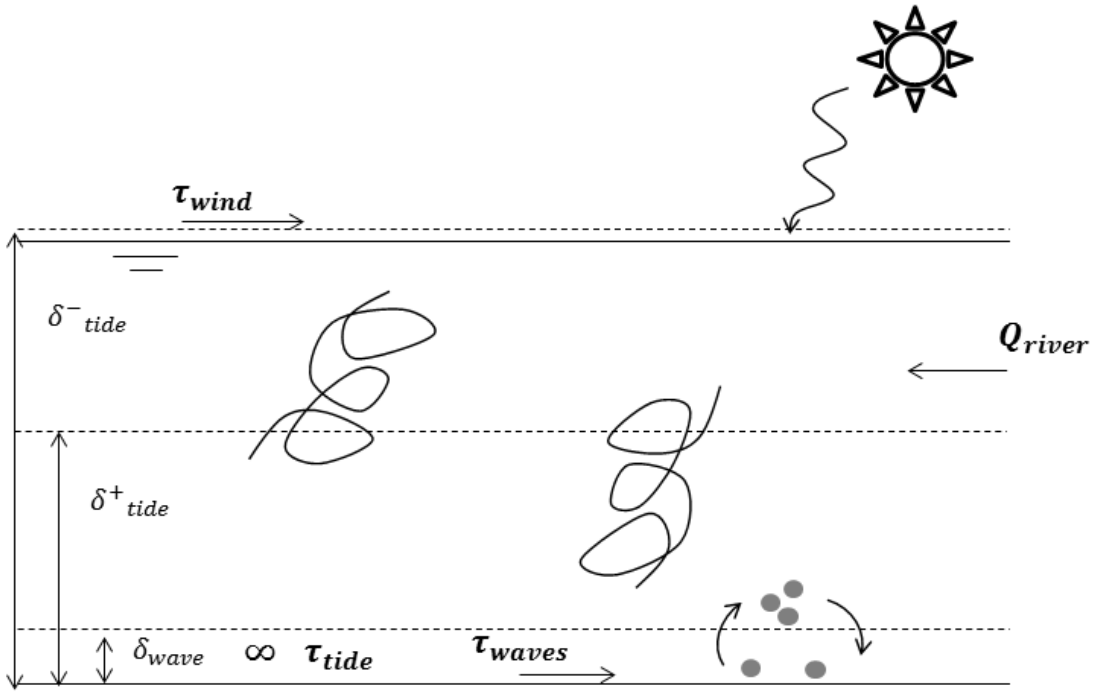

Figure 1.3: A sketch of all the processes involved in the Dutch coastal zone, such as the tide, wind, waves, river discharge (Q_{river}) and the sun. τ_{wind} is the wind stress on the water surface, τ_{tide} indicates the tidal stirring of the tide and τ_{waves} is the bed shear stress of the waves. δ_{wave} is the wave boundary layer induced by the waves. δ_{tide} is the boundary layer induced by the tide, where δ^-_{tide} determines the boundary of the clockwise component of the tide and δ^+_{tide} the anti-clockwise component of the tide (see section 2.4).

Unique in-situ dataset

The aim of this study is to gain more insight into the complex four dimensional nature of the Rhine ROFI, in order to allow a better understanding of the behaviour of SPM. To achieve this the movement and the role of the plume near Egmond and Wijk aan Zee in the Northern part of the Dutch coastal zone is studied, using a unique in-situ dataset. In October 2011 the Port of Rotterdam Authority and NIOZ sailed simultaneously on two parallel cross-shore transects, one near Egmond and one near Wijk aan Zee, 70 and 82 km from Hoek van Holland. The measurements took thirteen hours, both transects were sailed eight times. Salinity, temperature, SPM and velocities were collected. This campaign results in information over depth, time, cross- and alongshore direction, allowing analysis in four dimensions. This has, as far as we know, never done before and gives extra information in the alongshore direction.

A Potential Energy Anomaly analysis is carried out to investigate the onset and breakdown of stratification and the different processes influencing this. The contribution of alongshore advection and straining is investigated with a simplified form of the three-dimensional Potential Energy Anomaly Equation (De Boer et al., 2008), influenced by wind, waves and tide. This is the first time this equation is used on in-situ data in both the along- and cross-shore direction. Therefore, it extends Smolders (2011) his study, where the three-dimensional Potential Energy Anomaly equation was used in cross-shore direction only. In addition, the presence of tidal ellipses is demonstrated with the use of tidal analysis.

This research is a building block for future research regarding the distribution of SPM. In this thesis attention is focussed on an in-depth understanding of the processes causing stratification and mixing within the Rhine ROFI, over 80 km from the mouth of the Rotterdam Waterway. This knowledge is then applied to a preliminary analysis of the measured SPM concentrations. The focus is only on the relation of the distribution of SPM to the tidal and wind driven currents and stratification. No attention is paid to the flocculation of the particles, or to mechanisms such as erosion and sedimentation. This is a preliminary investigation into the distribution of SPM only.

First an overview of the large scale dataset is made and a preliminary analysis is performed. However, this study focuses on a detailed analysis of the unique in-situ dataset obtained by the PoR and NIOZ in the Northern part of the Dutch coastal zone, in order to help to interpret this large scale dataset in future research.

Outline

In the following sections a literature review is first presented in Chapter 2. This chapter provides details of previous research and the theory necessary to understand the complexity of the physical processes within the Rhine ROFI. This theory is used to analyse the in-situ data set, which is described in Chapter 3. Here, the used methods to analyse the data are described in detail. In addition to the results of the dataset, the Potential Energy Anomaly analysis and the tidal analysis are given in Chapter 4. These results are discussed in Chapter 5. The role of the downstream plume and the different cross- and alongshore processes are highlighted. Conclusions, including ideas on the methodology and recommendations for future research are presented in Chapter 6. In Appendix B a preliminary analysis of the large scale dataset obtained by the PoR is presented.

Chapter 2

Theoretical Background

2.1 Introduction

This chapter presents an overview of the theory used in this thesis. It provides an overview of the physical processes influencing stratification and mixing in the Rhine ROFI and their impact on the distribution of Suspended Particulate Matter (SPM). In Section 3.2 an overview of the Rhine ROFI is presented. This is followed by an explanation of the Potential Energy Anomaly in Section 3.3. Section 3.4 and 3.6 discuss the different processes which play an important role in the Rhine ROFI. An overview of all the processes in the Rhine ROFI is presented in figure 1.3. Section 3.4 considers tides, while Sections 3.5 and 3.6 wind and waves respectively. The distribution of SPM is reviewed in the last section.

2.2 Rhine ROFI

The rivers Rhine and Meuse are discharging freshwater in the North Sea. Together they have an average discharge of 2300 m^3/s. The amount of freshwater is discharged in the North Sea by the Rotterdam Waterway and the Haringvliet. The largest contribution is from the Rotterdam Waterway and a smaller amount of water is discharged intermittently by the Haringvliet sluices. The combined freshwater discharge results in a body of low salinity water in front of the Dutch coast. This body of fresh water is called the Rhine ROFI, it has a width varying from 20 to 40 km and extends 100 km northwards from the river mouth (De Boer et al., 2006). The freshwater discharge acts as a source of buoyancy in the Dutch coastal zone.

The Rhine ROFI is affected by changes in discharge and temperature. During winter and spring the largest discharges occur (Visser et al., 1991). Solar radiation influences the seasonal warming of the Rhine ROFI. During the summer, when the solar radiation is larger, the shallow Dutch coastal zone heats up faster than deeper surrounding waters. During the winter the ROFI is colder than the surrounding waters, in March the ROFI switches back to be warmer than the adjacent waters (Pietrzak et al., 2011). A larger discharge can be linked to a larger amount of fresh water in the system, more energy will be needed to mix the entire water column. The difference in temperature and salinity of the plume affects the density distribution along the Dutch coast. According to De Kok et al. (2001) the density field in the Rhine ROFI is dominated by the salinity structure.

Due to the Coriolis force, caused by the rotation of the Earth, the freshwater outflow turns to the right (in the Northern Hemisphere) and subsequently flows northward along the Dutch coast. The Coriolis force gives rise to a residual alongshore current, the coastal current (Simpson et al., 1993). Due to these alongshore currents the cross-shore density structure of the Rhine ROFI reaches a hundred kilometers from the source. The river discharge and the Coriolis force affect the density field close to the Dutch coast. Horizontal density differences are in cross- and alongshore direction. According to Suijlen and Duin (2002) density differences cross shore are larger than alongshore. The time averaged density field is approximately uniform in alongshore direction.

However, the instantaneous density field is more complicated. Both density gradients diminish in offshore direction. The shape of the Rhine ROFI is divided into a bulge region, around the mouth, and a plume downstream. The location of the plume and the bulge depends on different factors, like the river discharge, wind velocity and tidal phase.

The horizontal density gradients described above cause residual currents. Heaps (1972) derived a simple hydrodynamic theory of density-induced motion in an idealized coastal sea. He was interested in the vertical velocity structure. For this theory a straight infinitely long coast with cross-shore sections that all have the same geometry is considered. The alongshore dependency of y can be eliminated considering that all conditions in the cross-shore sections are the same. The derived set of equations can be found in appendix A. The situation of horizontal density differences causes a baroclinic density gradient. A barotropic pressure gradient arises due to the difference in height of the free surface.

When bed friction is limited, the force induced by the pressure gradient can only be balanced by the Coriolis force, induced by the Earth's rotation. The flow will be deflected towards the right and results in an alongshore flow towards the north (for the Northern Hemisphere) as the river flows in westerly direction. This balance is also known as the "Thermal wind balance". When friction is the dominating force, the pressure gradient is balanced by the internal friction, a non-linear velocity shear. This results in a cross-shore current which is directed offshore at the surface and onshore at the bottom. This limited case is called "estuarine circulation". Heaps set of equations combines these two limiting cases. Internal friction and the Earth's rotation seem to be important factors determining the structure of the density current. It leads to a residual current which has an onshore direction at the bottom and a northerly at the surface.

In the Rhine ROFI the horizontal density gradients are not uniform. The cross-shore density gradients are larger than the alongshore density gradients. To apply Heaps' theory to the Rhine ROFI only the cross-shore density gradients are taken into account, which diminish rapidly offshore. The magnitude of the currents diminish offshore as well, because its magnitude is determined by the density gradient. Figure 2.1 shows the three-dimensional residual current field in front of the Dutch coast according Heaps. Heaps took horizontal density differences into account only, thus with vertical stratification this simple theory does not hold anymore. The Rhine River mouth is more complex and cannot be described with Heaps' theory (De Boer, 2009).

The fresh water discharge causes stratification in the Rhine ROFI, when the fresh water flows over the more saline water. During stable stratification the pycnocline, a steep change of density with depth, is visible. Stratification shuts down turbulence at the pycnocline (Geyer, 1993; Burchard and Baumert, 1998; De Nijs et al., 2010, 2011). This has an effect on the velocity profile and the distribution of SPM. The velocity profile is decoupled. This gives rise to the existence of ellipses which are rotating independent from each other (Simpson et al., 1993). Due to the diminished turbulence the SPM is trapped below the pycnocline (Joordens et al., 2001).

In the Rhine ROFI there is a competition between stratification and mixing over the vertical. The stratifying factors are the buoyancy forces of the fresh water inflow, global radiation and tidal straining. The wind, waves and tidal stirring are the factors which try to mix the whole water column (Souza and Simpson, 1997). Simpson and Bowers (1981) studied stratification caused by surface heating. They introduced a parameter to investigate the influence of the competing factors in stratification and mixing, as some coastal waters have fresh water input as buoyancy force, like the Dutch coastal zone. Simpson et al. (1990) adapted the energy considerations for stratification caused by fresh water input. This parameter, the Potential Energy Anomaly, is a good measure for the state of the water column. This parameter is further used and developed by different researchers (Simpson et al., 1990; Burchard and Hofmeister, 2008; De Boer et al., 2008). The Potential Energy Anomaly is further discussed in the next section.

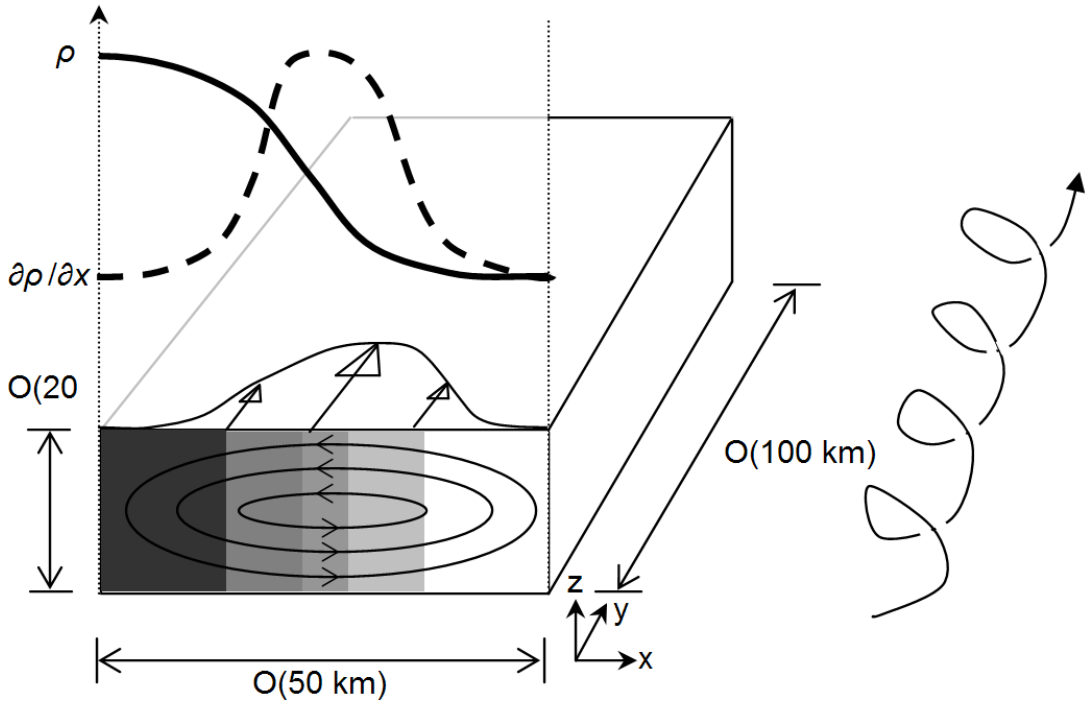

Figure 2.1: Concept of the three-dimensional residual current field in the Rhine ROFI. The s-shaped density structure ρ results in a cross-shore density gradient $\frac{\partial \rho}{\partial x}$ which exhibits a Gaussian curve. The alongshore 'thermal wind' velocity and the cross-shore 'estuarine circulation' follow a cross-shore Gaussian distribution as well. The right figure shows the path a non-buoyant particle will follow in this three-dimensional current field. Figure by De Boer (2009), after Visser (1993).

2.3 Potential Energy Anomaly

The Potential Energy Anomaly (PEA), introduced by Simpson and Bowers (1981), is a simple measure to show how much energy is required to mix the entire water column. Simpson et al. (1990) followed this approach and investigated the influence of different stratifying and mixing factors. These approaches were only for one- or two-dimensional models. De Boer et al. (2008) derived the potential energy anomaly for three-dimensional flows. The equation is derived from the Reynolds averaged advection-diffusion equation for density and the potential energy anomaly equation, taking barotropic effects into account. This gives the following equation:

$$\begin{aligned}\frac{\partial \varphi}{\partial t} = \frac{g}{H}\int_{-h}^{\eta}\left(\begin{array}{l}\overbrace{\tilde{u}\frac{\partial \bar{\rho}}{\partial x}}^{S_x}\overbrace{+\bar{u}\frac{\partial \tilde{\rho}}{\partial x}}^{A_x}\overbrace{+\tilde{u}\frac{\partial \tilde{\rho}}{\partial x}}^{N_x}\overbrace{-\frac{1}{H}\frac{\partial \bar{\tilde{u}}\bar{\tilde{\rho}}H}{\partial x}}^{C_x}\overbrace{+w\frac{\partial \rho}{\partial z}}^{W_z}+\ldots \\ \underbrace{\tilde{v}\frac{\partial \bar{\rho}}{\partial y}}_{S_y}\underbrace{+\bar{v}\frac{\partial \tilde{\rho}}{\partial y}}_{A_y}\underbrace{+\tilde{v}\frac{\partial \tilde{\rho}}{\partial y}}_{N_y}\underbrace{-\frac{1}{H}\frac{\partial \bar{\tilde{u}}\bar{\tilde{\rho}}H}{\partial y}}_{C_y}\underbrace{+\frac{\partial \langle \rho' w' \rangle}{\partial z}}_{M_z}\end{array}\right) z dz + \ldots \\ \int_{-h}^{\eta}\left(\underbrace{\frac{\partial \langle \rho' u' \rangle}{\partial x}}_{D_x}+\underbrace{\frac{\partial \langle \rho' u' \rangle}{\partial x}}_{D_y}-\frac{1}{H}\left(\underbrace{\langle \rho' w' \rangle|_s}_{D_s}\underbrace{-\langle \rho' w' \rangle|_b}_{D_b}\right)\right) z dz - \underbrace{\frac{\varphi}{H}\frac{\partial \varphi}{\partial t}}_{B_H} - \underbrace{\left(\frac{g}{H}\right)\left(\rho(\eta)\eta\frac{\partial \eta}{\partial t}\right)}_{B_\eta}\end{aligned} \tag{2.1}$$

Where $\tilde{\rho} = \rho - \bar{\rho}$,$\tilde{u} = u - \bar{u}$ and $\tilde{v} = v - \bar{v}$ are the deviations from the depth mean values. u is the cross-shore velocity and v the velocity alongshore. The terms S_x and S_y represent cross-shore and alongshore straining respectively. S_x is the tidal straining term introduced by Simpson et al. (1990). Advection in cross- and alongshore direction is denoted by the terms A_x and A_y. The

terms N_x,N_y,C_x and C_y originate from the advection-diffusion equation and describe the non-linear interaction between the deviation of both density and velocity over the vertical. The effect of vertical mixing, due to turbulence, on the density profile is described by the term M_z. Up- and downwelling is related to the term W_z. D_x and D_y are the horizontal depth averaged dispersion terms. The terms D_s and D_b represent the surface density and bed density fluxes. The last two terms, B_H and B_η, are due to changes in water depth and surface elevation in time. A similar equation is derived by Burchard and Hofmeister (2008).

2.4 Tide

The tide contributes significantly to the hydrodynamics of the North Sea. It is an important process for the onset and breakdown of stratification and therefore for the distribution and behaviour of SPM. De Boer (2009) has investigated the interaction between tides and stratification. Simpson et al. (1993) defined two different time scales for the influence of the tide, respectively the spring-neap tidal cycle and the semi-diurnal tidal cycle. This section will discuss the knowledge gained during previous research. First some general information about tides is given, followed by the tidal cycle, the vertical structure of tidal currents and tidal straining.

2.4.1 Tides in general

In the North Sea twice daily there is high and low water, also called a semi-diurnal tide. This is mainly caused by two main tidal components, M2 and S2. M2 is the tide which is influenced by the moon twice a day. S2 is the contribution to the semi-diurnal tide from the sun. Their amplitudes and phases are different for every location at the earth. The sun and the moon are causing tidal amplitudes on earth. Their contribution can strengthen or weaken the signal of the tide. When the sun, earth and moon are positioned in one line the amplitudes of the tide are largest, this is called spring tide. The M2 and S2 components are in phase and reinforce each other. Neap tide, when the tides have smaller amplitudes, happens when the M2 and S2 constituents are out of phase. For more information about the generation of the tide and the constituents see for example (Bosboom and Stive, 2012).

The tide is a phenomenon where water levels rise and fall. The period from the lowest to the highest elevation is called the rising period. The falling period is the period from the highest to the lowest water level. The horizontal movement is called the horizontal tide or the tidal current, which moves forward during flood and backward during ebb. Therefore flood currents are in the same direction as the propagation of the tidal wave and ebb currents are in the opposite direction. Slack water refers to the tidal flow reversal (low water slack = reversal from ebb to flood; high water slack = reversal from flood to ebb) (Bosboom and Stive, 2012). Every coast has its own specific tidal curve, because it depends on the size, shape and depth of the basin. The tide along the Dutch coast is a Kelvin wave, which can be defined as follows:

$$\begin{aligned} \eta(x,y,t) &= \eta_0 e^{\frac{fx}{c}} \cos(\omega t - ky) \\ v(x,y,t) &= \tfrac{c}{h} e^{\frac{fx}{c}} \cos(\omega t - ky) \end{aligned} \tag{2.2}$$

The equations show that for a symmetrical tide the tidal velocity is in phase with the tidal amplitude. The flood velocities are maximum around high water and the ebb velocities around low water. The Kelvin wave can be described as a trapped wave, it follows the coastline. In the Northern Hemisphere the wave propagates northward and has its maximum amplitude at the coast (η_0). The amplitude decays with distance from the coast.

The Dutch coastal waters are shallow and friction plays a role. Therefore the Kelvin wave is distorted and becomes asymmetrical. As a result of bed friction the tidal elevation and velocities are out of phase. Bed friction as well leads to a distortion in amplitude and shape of the tidal elevation. Figure 2.2 shows that the tide deforms running northwards along the Dutch coast. The tidal range differs and the falling period is longer than the rising period. The exact differences vary

for each location along the coast. Both tidal elevation and tidal velocity display tidal asymmetry over the vertical and horizontal axis.

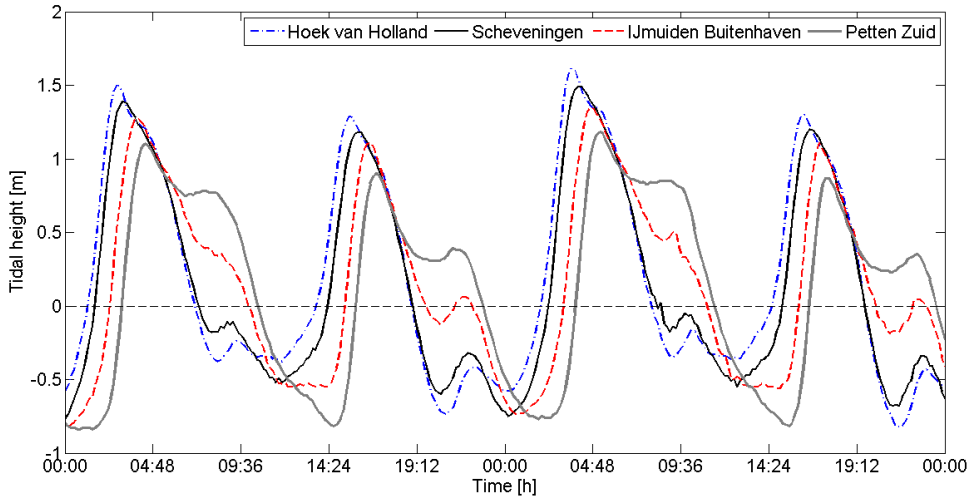

Figure 2.2: The deformation of the tidal elevation along the Dutch coast, on the 23rd and 24th of July 2009. The tidal elevation is displayed at Hoek van Holland, Scheveningen, IJmuiden Buitenhaven and Petten Zuid. (Tidal data from www.waterbase.nl)

2.4.2 Tidal cycle

The tide causes a periodic change in the state of the Rhine ROFI. Simpson et al. (1993) defined two different time scales for the influence of the tide. The first one is the fortnightly spring-neap cycle. The second time scale is the semi-diurnal ebb-flood tidal cycle. Both are explained in this section. Simpson et al. (1993) observed an alternation of stratification and mixing in vertical direction on a scale of the spring-neap tidal cycle. During spring, stirring is large, the water column is well-mixed over the vertical. Around the mouth the water column remains stratified. In horizontal direction density gradients are visible, from fresh water close to the coast to more saline water offshore. When the turbulent kinetic energy is low, during neap tide and weak winds, the density gradient relaxes and the water column becomes stratified. These observations showed the periodic change of the tide. The state of the Rhine ROFI is also controlled by wind and discharge. Wind can enhance stirring, therefore during neap and strong winds the water column can remain well-mixed (Smolders, 2011).

During the observations, (Simpson et al., 1993), another phenomenon was observed. When the water column was vertically mixed, there was a strong correlation between the near-surface and near-bottom residual currents. With the onset of stratification the bottom and surface currents were decoupled. From their observations it follows that during well-mixed conditions the surface currents are rectilinear and parallel to the coast. When the water column is stratified the tidal currents show a cross-shore component. In this situation the bottom and surface currents are out of phase. Visser et al. (1994) and Simpson and Souza (1995) observed this phenomenon.

The second timescale is the semi-diurnal tidal cycle. This time cycle causes an alteration of a stratified and well-mixed plume, due to the ebb and flood currents of the Kelvin wave. At high water the plume is maximally stratified. During low water the plume is well-mixed. Simpson et al. (1993) showed that this semi-diurnal signal is only visible during neap tide. This process is called tidal straining by Simpson and Souza (1995) and is explained in further detail in subsection 2.4.4. During spring tide, well-mixed conditions, the semi-diurnal signal is not visible.

2.4.3 Vertical structure of tidal currents

In shallow water tidal currents have a marked vertical structure and can be explained by Ekman Dynamics. The tidal current vectors cover a horizontal elliptical path during a tidal cycle, as is explained in 2.4.2. Prandle (1982a,b) investigated this vertical structure, with the assumption of a vertically uniform eddy viscosity. To observe the behaviour of the ellipses, he decomposed the tidal current vectors into a clockwise and an anti-clockwise motion (R^+ and R^-). Mathematically this is easier than decoupling the cross- and alongshore velocities (u and v), because the u and v momentum equations are linked by the Coriolis parameter. When the amplitudes are the same, only an alongshore velocity is visible. An ellipse is established when R^+ and R^- have different amplitudes. The terms clockwise and anti-clockwise can also be defined in respect to the rotation of the earth. Rotation in the direction of the planetary earth rotation is called cyclonic and in opposite direction anti-cyclonic. More background of Prandle's his mathematical derivation can be found in appendix A.

The presence of the coast requires adaptation of Prandle's theory for the Rhine ROFI. By the presence of the coast depth-averaged cross-shore tidal transport must be zero. This holds both during well-mixed and stratified conditions. As a result the surface and bottom velocities cannot be directed in the same direction. Therefore a current in the upper layer is compensated by an opposite current in the lower layer. During well-mixed conditions vertical mixing compresses the cross-shore currents, as a result of large eddy viscosity and turbulence. This leads to alongshore currents, parallel to the coast. During stratified situations turbulent kinetic energy is dissipated around the pycnocline, which results in decoupling of the velocity profile.

Souza and Simpson (1996) investigated the modification of the tidal ellipses. The boundary layer for the cyclonic and anti-cyclonic components is defined. For the Rhine ROFI this results in different boundary layer thickness for the two components. The frictional boundary for the anti-cyclonic component covers the entire water depth. While the cyclonic component extends to half of the water column. The difference in boundary layer thickness causes an ellipse to rotate more anti-cyclonic with increasing distance from the bed. This results for a well-mixed situation in a degenerate ellipse at the surface and a reduced cyclonic ellipse at the bottom. This is shown in figure 3.22, where the C stands for clockwise and A/C for anti-clockwise. This is different when the water column is stratified. The eddy viscosity is reduced due to the presence of the pycnocline. Turbulent motions within the pycnocline are suppressed and therefore momentum transfer is inhibited. The anti-cyclonic component above the pycnocline is no- longer affected by bed friction and rotates with its so called free-stream velocity. Below the pycnocline bed friction has an impact and reduces the motion of the anti-cyclonic component. The cyclonic motion is not affected by the pycnocline, it has almost it's free-stream velocity. As a result an anti-cyclonic ellipse in the surface layer and a cyclonic ellipse in the bottom layer arises during stratified conditions. Figure 3.22 shows the rotation of the velocity vector, describing an elliptical path, in a well-mixed and stratified water column.

2.4.4 Tidal straining

The process where cross-shore currents advect fresher surface water offshore and more saline bottom water onshore is called tidal straining. Cross-shore tidal currents act on the horizontal density gradient and cause periodic stratification. Simpson et al. (1990) described the tidal straining theory, based on their research in the Liverpool Bay area. Here the tide can be seen as a standing wave. Therefore the density gradient and the tidal currents are in the same direction. The velocity profile has a logarithmic shape. The faster fresher surface water is transported offshore and flows over the more saline bottom water. At the end of ebb the water column is maximally stratified. Water is pushed back during flood. At the end of flood the water column is mixed again. The interaction between the cross-shore tidal current and the density gradient is defined as tidal straining. Tidal stirring will oppose the development of stratification on the ebb and accelerate the breakdown on the flood (Simpson et al., 1990). Figure 2.4 shows the process of tidal straining.

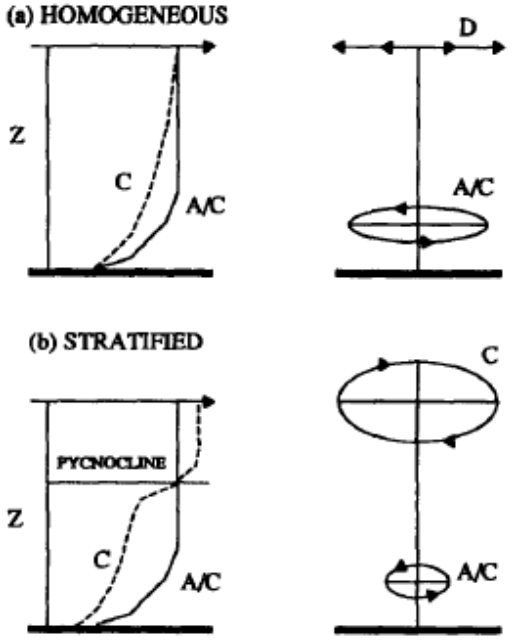

Figure 2.3: Scheme of the vertical profile of the clockwise (C) and anti-clockwise (A/C) rotary components and ellipse configuration. (a) For the homogeneous case when N_z is constant.(b) For the stratified case when N_z is reduced at the pycnocline. Figure by Souza and Simpson (1996).

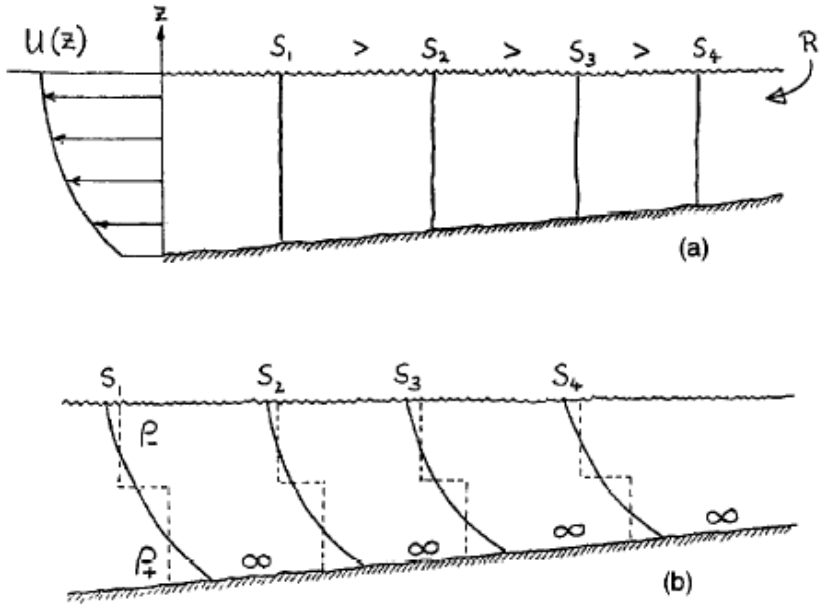

Figure 2.4: Schematic picture of tidal straining: (a) isohalines of density on a cross-shore section at the start of the ebb; (b) stratification induced by differential advection on the ebb and modified by mixing at top and bottom boundaries. Figure by Simpson (1997).

In the Rhine ROFI the situation is different. The tide is a Kelvin wave, therefore the tidal currents are in alongshore direction and the density gradient is cross-shore. Simpson and Souza (1995) tried to apply the tidal straining theory to the Rhine ROFI. Simpson et al. (1993) already observed the

semi-diurnal oscillations in the stratification. Simpson and Souza (1995) linked the strain-induced stratification to the observed existence of tidal ellipses. The periodic cross-shore velocity interacts with the average cross-shore density gradients. From low to high water the surface currents are offshore, this advection moves the fresh water offshore. The water column is maximally stratified at high water. From high to low water the surface currents are directed onshore and pushes the freshwater back to shore. Therefore at low water the water column is well-mixed again and the plume is closest to the shore.

Simpson et al. (1990) introduced strain induced periodic stratification (SIPS), caused by tidal and alongshore straining. De Boer et al. (2008) discovered that advection can play a role in the onset and breakdown of stratification, therefore they defined advection and strain induced periodic stratification (ASIPS) instead of only SIPS. A_x and A_y are the terms representing the cross- and alongshore advection in the potential energy anomaly, explained in section 2.3. According to De Boer et al. (2008) the cross- and alongshore straining and advection terms are all important for describing the hydrodynamics in the Rhine ROFI and cannot be neglected. Figure 2.6 shows ASIPS, the combined effect of cross-shore straining and alongshore advection and - straining, for the downstream region of the Rhine ROFI.

2.5 Wind

The wind has an influence on the behaviour of the Dutch coastal system. The wind can have the tendency to stratify or mix the water column. This section will explain the role of the wind in the Rhine ROFI. First the Ekman and frictional response to the wind are explained, followed by the explanation of upwelling and downwelling. The last subsection explains the influence of the direction and magnitude of the wind on the Rhine ROFI and its response.

2.5.1 Ekman and frictional response to the wind

When the wind blows over the sea surface wind energy is transferred to the surface by frictional effects. The wind can be divided into a geostrophic (Ekman) and an ageostrophic (frictional) component. The ageostrophic wind component is the component that pulls the water in the same direction as the wind is blowing. Once the water mass is moving the Coriolis force becomes important, friction and Coriolis are in balance. The Coriolis force acts to the right (on the Northern Hemisphere) and deflects the water to the right of the wind direction. This response is caused by the geostrophic wind component.

The influence of the wind stress on the water column can be explained by the linearised equations of motion. The water column is assumed to be deep and bottom friction is ignored. The equations for a rotational fluid become (Van Wiechen, 2011; Csanady, 1982):

$$N\frac{\partial^2 u}{\partial z^2} = -fv + \frac{1}{\rho}\frac{\partial p}{\partial x} \tag{2.3}$$

$$N\frac{\partial^2 v}{\partial z^2} = fu + \frac{1}{\rho}\frac{\partial p}{\partial y} \tag{2.4}$$

Where u and v are the cross-shore and alongshore velocities, N is a constant eddy viscosity, ρ is the density of the water and p is the pressure in the sea, at any location. The Coriolis parameter is defined by f. The velocities can be assumed to consist of a pressure and wind induced velocity. Each part can be solved separately and added back together afterwards:

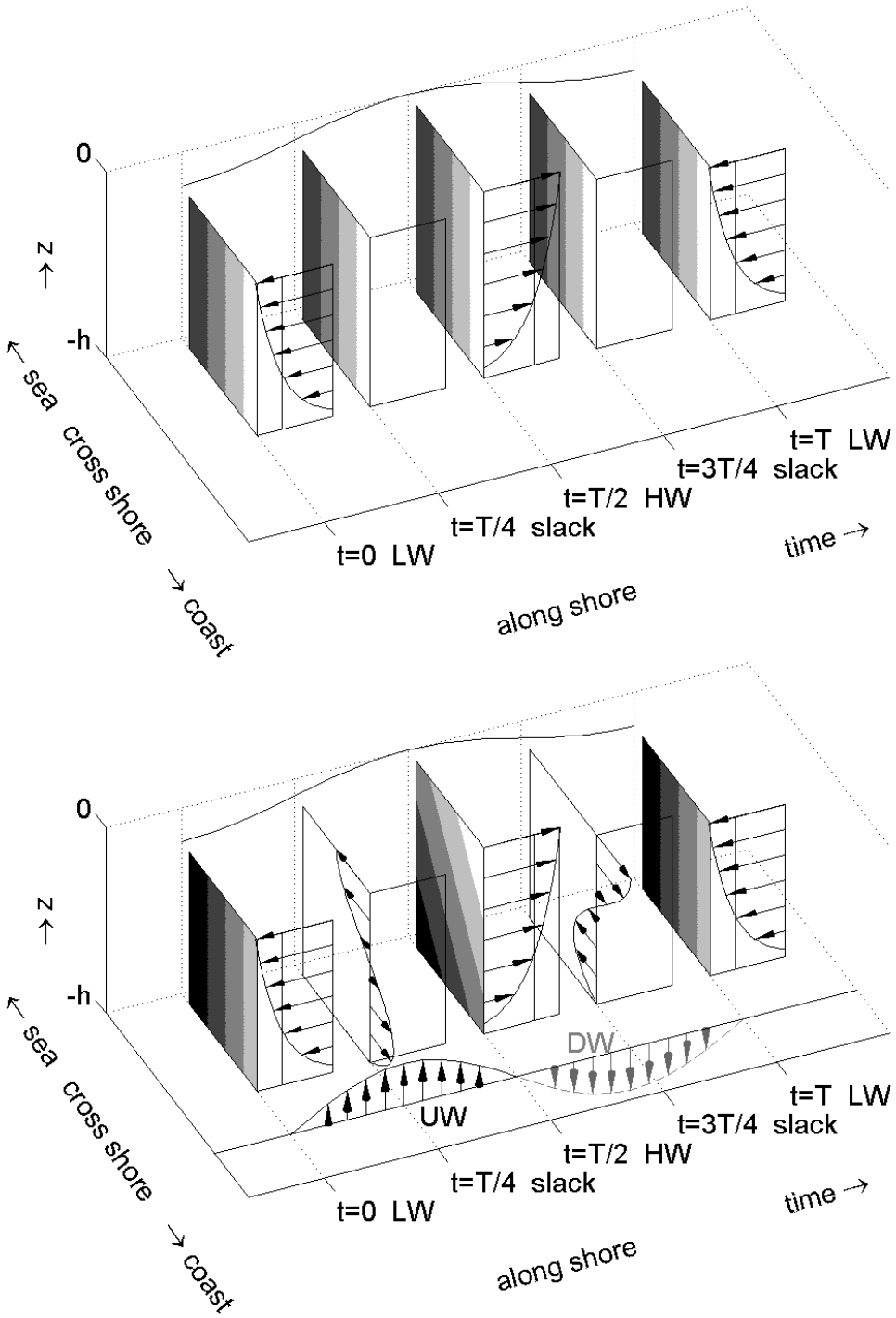

Figure 2.5: The upper panel shows the situation during well-mixed conditions. There is no interaction between the cross-shore density gradient and ebb and flood velocities. The lower panel shows tidal straining in the Rhine ROFI during stratified conditions, due to the occurrence of a cross-shore velocity shear. This velocity shear interacts with the cross-shore density gradient. Figure by De Boer (2009).

$$u = u_a g + u_E \quad \text{and} \quad v = v_a g + v_E \tag{2.5}$$

$$f u_a g = -\frac{1}{\rho}\frac{\partial p}{\partial x} \quad \text{and} \quad f v_a g = \frac{1}{\rho}\frac{\partial p}{\partial x} \tag{2.6}$$

$$f u_E = N\frac{\partial^2 v_E}{\partial z^2} \quad \text{and} \quad f v_E = -N\frac{\partial^2 u_E}{\partial z^2} \tag{2.7}$$

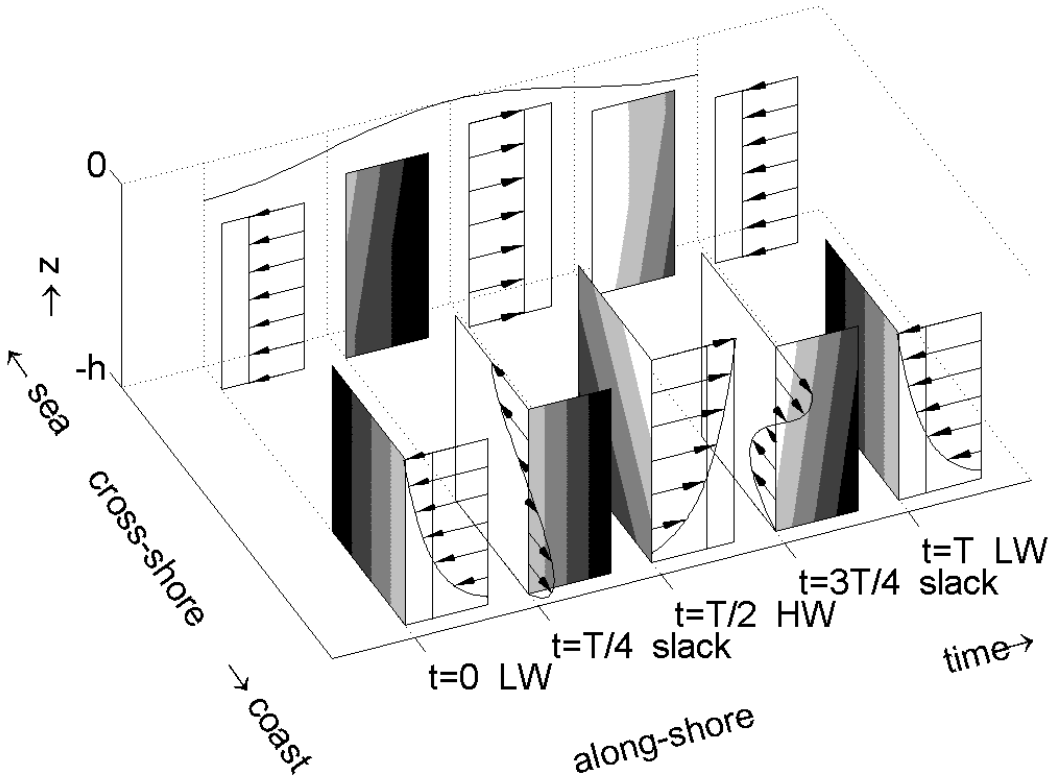

Figure 2.6: The combined effect of alongshore and cross-shore processes,as advection and straining, is shown for the downstream region of the Rhine ROFI, during one tidal cycle. The figure in the back shows alongshore advection. The figure in the front shows cross-shore and alongshore straining. The maximum stratification occurs during high water slack (3/4T). Figure by De Boer et al. (2008).

Following Ekman, assuming a constant vertical eddy viscosity, a homogeneous water column with a zero surface slope, the geostrophic part becomes:

$$-fu_E + N\frac{\partial^2 v_E}{\partial z^2} = 0 \tag{2.8}$$

$$fv_E + N\frac{\partial^2 u_E}{\partial z^2} = 0 \tag{2.9}$$

For a wind stress acting in the y-direction the solution for the geostrophic part can be shown by:

$$u_E = \pm V_0 cos\Big(\frac{\pi}{4} + \frac{\pi}{D_E}z\Big)\exp\Big(\frac{\pi}{D_E}z\Big) \tag{2.10}$$

$$v_E = V_0 sin\Big(\frac{\pi}{4} + \frac{\pi}{D_E}z\Big)\exp\Big(\frac{\pi}{D_E}z\Big) \tag{2.11}$$

where V_0 is defined as $V_0 = (\sqrt{2\pi\tau_{yn}})/(D_E\rho|f|)$ and D_E is the depth of frictional influence, also called the Ekman depth. These equations show that the surface current differs from the bottom current. The surface currents are defined as $u_E = \pm V_0 cos(45)$ and $v_E = V_0 sin(45)$. The surface current will be deflected 45 degrees to the right of the wind (in the Northern Hemisphere). The currents decay by $\exp(\pi D_E)/z)$ and deflects further towards the right, when going down in the water column. An Ekman spiral is formed, where the wind induced currents swing from 45 degrees at the surface towards the opposite direction of the wind at the bottom, with a magnitude of $0.004V_0$. Ekman his theory is valid for deep oceans. The Dutch coastal zone is shallow (< 20 m), where friction plays an important role. However, Chao (1988) showed that Ekman drift on the river plume is still valid for shallow areas.

2.5.2 Upwelling and downwelling

The presence of the Dutch coast causes another movement of the water as a result of the wind, defined as upwelling and downwelling. When wind blows along a coastline, the Coriolis force pushes the surface waters to the right. For a northerly wind (i.e. wind coming from the north) the surface waters will be pushed offshore. By continuity, the water that moved offshore needs to be replaced, which could only be by water from the bottom layers. This process is called upwelling. With southerly winds (i.e. wind coming from the south) the opposite happens. The surface waters are pushed towards the coast, which leads to an offshore movement of the bottom water. The onshore pushed surface water will flow downward. This is called downwelling. Onshore and offshore winds also cause downwelling and upwelling, however for these situations the frictional component is responsible. An onshore wind causes downwelling and an offshore wind upwelling.

2.5.3 Influence of the wind on the water column

Wind can work as a mixing or stratifying process in the Rhine ROFI. Souza and Simpson (1997) show that the wind, as a mixing process, is important regarding stratification. In their 1992 measurements vertical stratification is present during spring tides. Only a vertical mixed water column was observed when wind stirring was high. Smolders (2011) found evidence for the importance of wind stirring as well. He observed a vertical homogeneous water column during neap tides with strong winds, when the wind relaxed the water column started to stratify.

The wind direction has an important influence on the behaviour of the system. The influence is different for a stratified or mixed situation. Van Wiechen (2011) investigated the influence of the wind direction and magnitude during neap tide (i.e. during stratified conditions). Figure 2.7 shows his findings. The influence of the wind direction is as follows. Southerly alongshore winds push the water towards the north by the frictional component. The Ekman response is towards the right, pushing the water towards the coast (i.e. eastwards). As a response the water column will be vertically well-mixed. Northerly alongshore winds push the water initially towards the south. Coriolis deflects the water seawards (i.e. towards the west). The water column will remain stratified. The ageostrophic wind component (by friction) pushes the water towards the coast for a westerly wind (i.e. onshore). The Ekman response deflects the water southwards. As a result the water column is vertically well-mixed. For an easterly wind (i.e. offshore) the water is initially pushed offshore and deflected to the right by Ekman Dynamics. The water column remains stratified. Upwelling of bottom water occurs.

Chao (1988) introduced the term "direct wind-induced vertical mixing". It means that when the wind magnitude increases the wind not only advect the surface layer leading to stratification or mixing, but also mixes the water directly over the vertical. An offshore wind pushes the fresh water offshore, which leads to a thin layer of fresh water. A large wind velocity mixes this thin fresh layer over the vertical. Van Wiechen (2011) showed this phenomena as well. With an increased wind speed the southerly and onshore winds result in a well-mixed water column. High wind speeds for northerly and offshore winds result in a wide and thin fresh water plume. The high wind speed will lead to direct wind-induced vertical mixing figure 2.7.

2.6 Waves

Waves play an important role in stirring up sediments and causing current motions which transport the sediments. Their impact is especially near the bed. A part of this thesis is about the distribution of suspended particulate matter. Waves have a clear influence on this (ref), therefore waves are interesting with respect to sediments to investigate. Information about waves is given within this section. In the North Sea two types of waves are dominant. There are swell waves, generated in a distant storm, and locally generated wind waves. The locally wind generated waves dominate the wave climate in the North Sea. These waves are irregular and short-crested. The wave characteristics, like wave height, period, propagation, direction and duration depend on the characteristics of the wind field, the fetch and the water depth.

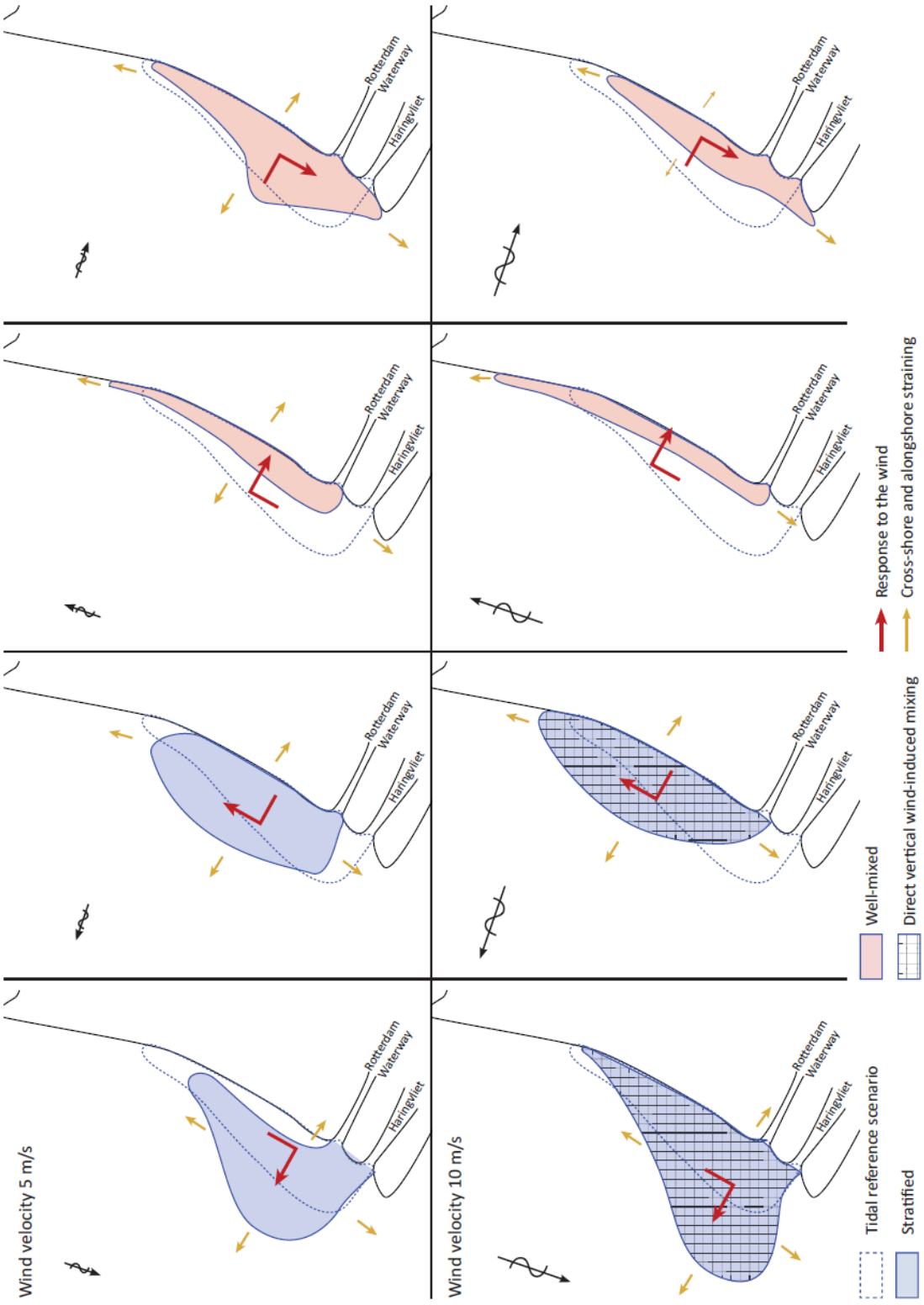

Figure 2.7: A sketch that summarizes the wind-driven motions in the Rhine ROFI during stratified conditions. The top panels present the 5 m/s wind scenarios, the bottom panels the 10 m/s scenarios. In horizontal direction the response of the Rhine ROFI to the different wind directions are discussed. Figure by Van Wiechen (2011).

Waves are a disturbance of the water surface. In deep water the orbits are circles, further away from the surface the diameter of the orbits decreases. In shallow water the orbits are ellipsoids becoming flatter near the bottom. Near the bottom the vertical velocities are reduced to zero, the magnitude of the horizontal displacement remains somewhat the same (Bosboom and Stive, 2012). At higher order the orbits are not closed, that means that there is a residual flow.

In shallow water (viz. coastal areas) ($\frac{h}{L} < 0.05$, where h is the water depth and L the wave length) the linear theory for waves does not hold anymore. Nonlinearities and friction are becoming important. This causes waves to deform, they become asymmetrical.

When the water depth becomes shallow ($\frac{h}{L} < 0.05$),waves are impacting the area near the bottom. A wave boundary layer develops near the bed. The orbital velocity is nonzero near the bed and causes an increase of turbulence, which enhances the bed shear stress. The bed shear stress due to waves can be defined as follows.

$$\tau_w = 0.5\rho f_w U_w^2 \tag{2.12}$$

Where ρ is the density, U_w is the near bed wave orbital velocity, which for linear theory (Soulsby, 1997) can be defined as

$$U_w = \frac{H\pi}{T \sinh kh} \tag{2.13}$$

In which H is the wave height, T is the wave period, h is the water depth and $k = \frac{2\pi}{L}$ is the wave number. Determination of the friction coefficient, f_w, for a rough bed and turbulent flow is complex. Generally this parameter will depend on the bed material and the bed forms. In appendix A.4 the way of calculating the wave bed shear stress and wave energy is presented.

Souza and Simpson (1997) investigated the effect of bottom stirring due to waves. This is an important factor in shallow regions like the Dutch coastal zone. They did not succeed to separate the direct influence of the waves from the influence of the wind, or swell waves from wind-generated waves. Their point model showed that the effect of waves, including the wave bed shear stress, does not lead to significant differences. In this case it seems that wave mixing does not have a significant influence on the overall mixing. In situations with large swell waves and low winds, it could have a larger influence on the mixing process.

Chapter 3

Methodology

3.1 Introduction

In this study observational data are used to obtain relations between the different mechanisms within the Rhine ROFI. A part of the data collected by the Port of Rotterdam Authority for the monitoring and evaluation program of the Maasvlakte 2 is used only. First the measurements are discussed, viz. the location of the measurements, the sensors used, the data processing and the conditions. To analyze the data different methods are used. Section 3.3 describes how the Potential Energy Anomaly can contribute to the understanding of the Rhine ROFI. Section 3.4 presents the tidal analysis used to obtain information about the tidal ellipses.

3.2 Measurements

The Port of Rotterdam Authority, PoR, carried out a field measurement campaign from 2007 till 2013. Each year six surveys were performed along the Dutch coast, covering an area from Petten in the North to Westkapelle in the South. A fishing ship, the BRA-7, was used to collect data during these surveys. After six years of in-situ measurements a large scale data set is obtained. Figure 3.1 shows all vertical profiles collected during the years 2007-2013. The measurements were taken at 100 predefined locations, during all seasons and in different order during each campaign. The coordinates of each measurement were about 500 - 1000 m from the predefined location. Apart from the "fixed" locations also transects were sailed. In order to help interpret this large scale dataset the background of the physical processes influencing the flow and the distribution of SPM along the Dutch coast need to be understood. An overview of all the data is made and analysed by making scatter plots (see Appendix B). However, the results of the scatter plots highlight the complex interplay of all the physical processes. Therefore, this study focuses on two simultaneously sampled parallel transects, which were sailed on the 13th of October 2011, together with NIOZ (Royal Netherlands Institute for Sea Research). Appendix C presents some pictures to get an impression of the measurement campaign of PoR.

3.2.1 Study area October 13, 2011: two parallel transects

Two parallel transects are analysed, both are presented in figure 3.2. Data for the northern transect, near Egmond aan Zee, was collected by PoR. NIOZ collected data with another vessel, RV Navicula, in the southern transect, near Wijk aan Zee. Each transect has four stations at a distance of 1, 2, 4 and 8 km from the coastline. The measurements started at station one, located 8 km offshore. The transect is sailed eight times, each time is called a track. Therefore each transect has 8 tracks, on different points of time. In total these measurements took thirteen hours. The measurements started around 5.00 a.m. and continued until 6:30 p.m on the 13th of October 2011.

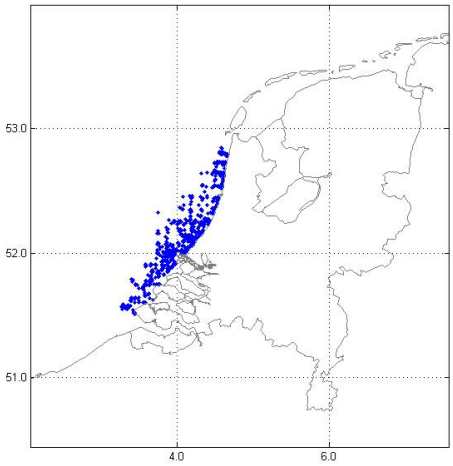

Figure 3.1: The sampling stations of the Port of Rotterdam Authority from 2009 till 2013

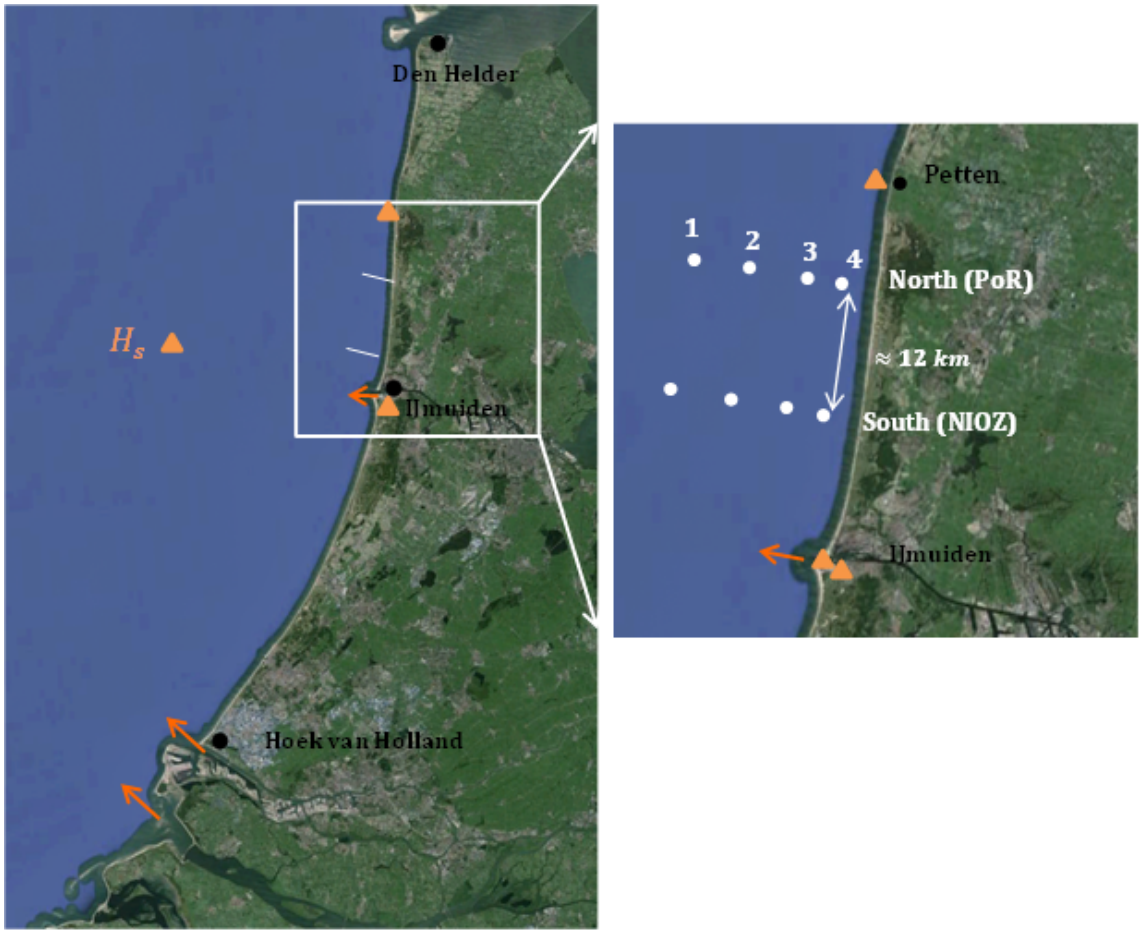

Figure 3.2: The measured transects at the 13th of October 2011. The northern transect is measured by PoR. NIOZ measured the southern transect. The four measuring stations are located at 1,2,4 and 8 km from the coast and are each measured eight times. The triangles are the measurement stations for the meteorological data. The station on sea measures the wave data, near IJmuiden the wind and tidal elevation are determined. The station near Petten measures the tidal elevation as well.

3.2.2 Instrumentation

PoR uses a so-called Siltprofiler, a platform which can be lowered into the water column and an ADCP (Acoustic Doppler Current Profiler) mounted alongside the BRA-7 at a depth of ca. 2.15 m. The Siltprofiler is a stainless steel frame of approximately 1.20 by 0.80 meter with a collection of twelve different measuring devices (figure 3.3(a)). The ADCP is a velocity meter and measures velocities in the vertical profile, from approximately two and a half meters below the surface down to the bottom. Table 3.1 gives an overview of all the measuring devices of PoR and NIOZ with a short description.

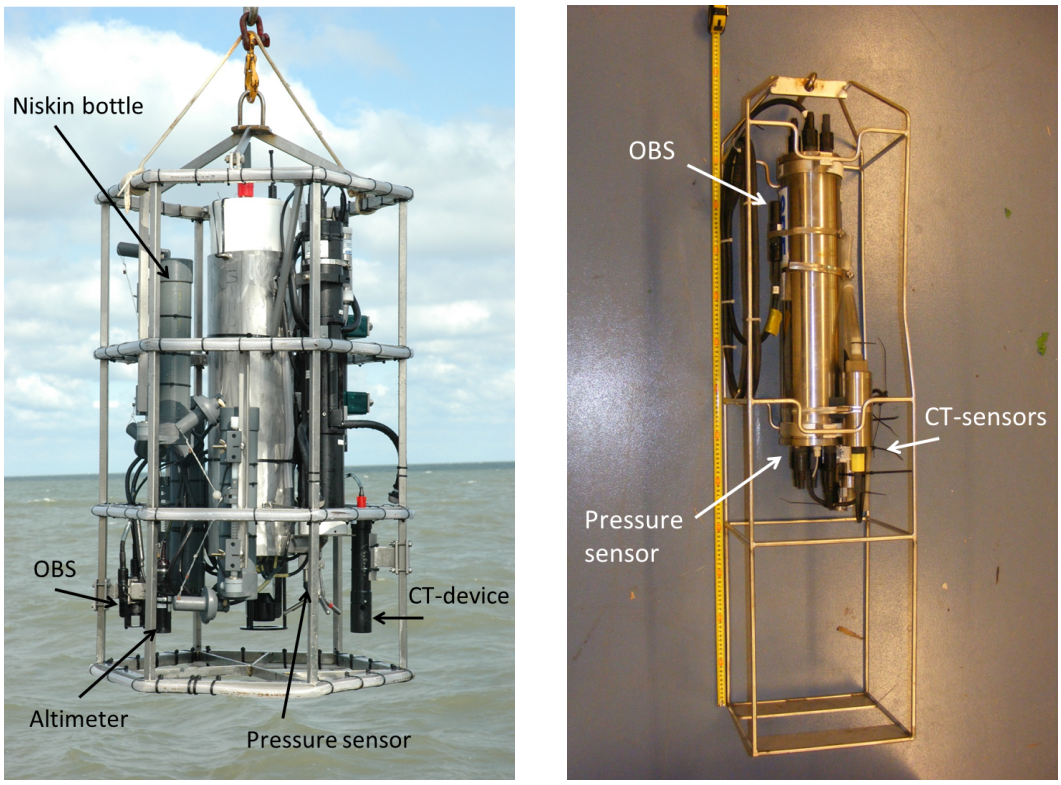

(a) (b)

Figure 3.3: The instruments used by PoR and NIOZ (a) The Siltprofiler of the Port of Rotterdam Authority with twelve different measurement devices (b) The Seabird SBE 911plus CTD of NIOZ with a temperature, conductivity and OBS sensor.

NIOZ recorded conductivity, temperature and pressure with a Seabird SBE 911plus CTD (Conductivity Temperature Depth sensors). An OBS (Optical Backscatter) sensor was attached to the CTD frame and measured optical backscatter. Figure 3.3(b) shows the CTD frame with the OBS sensor of NIOZ. The frame has a height of approximately 1.30 m and a width of 0.35 m. Current velocities (horizontal and vertical) were measured with a RDI Workhorse Rio Grande 1200 kHz ADCP, which is mounted at the starboard side of the ship at 1 m below the water level.

At each measuring station, both for PoR and NIOZ, the measuring frames are lowered into the water. Niskin bottles, one at the surface and one at the bottom, are used to take water samples. These water samples are used for calibration of the OBS sensor.

For this study only the CTD, OBS and ADCP sensors of PoR and NIOZ are used. The CTD sensors measure a vertical profile of conductivity and temperature. After processing a salinity profile is obtained. An OBS sensor records the optical backscatter, which can be converted into the concentration of SPM over the vertical and is sensitive to air bubbles. The ADCP measures

PoR	NIOZ	Description
CTD	CTD	Conductivity Temperature Depth sensor
OBS	OBS	Optical Backscatter sensor
ADCP	ADCP	Acoustic Doppler Current Profiler
Niskin bottle	Niskin bottle	For water samples
Altimeter		Determines the altitude above seabed
Pressure sensor		Determines depth below water surface
ADV		Current velocity meter
LISST		Determines grainsize SPM
ACS		Spectral absorption and attenuation meter
Fluorescence meter		Measures concentration chlorophyll

Table 3.1: The instruments of PoR and NIOZ. During the 13th of October 2011 the CTD, OBS and ADCP are used.

the water velocities. The Siltprofiler is first lowered a few meters below the water surface, then it is pulled up again till around one meter below the surface, to get rid of air bubbles. Then the profiler is lowered with a speed of 10 cm/s to the seabed (the downcast), and lifted up again (the upcast). This lowering procedure is shown in figure C.6. When the profiler touches the bottom sediment is stirred up from the seabed, which is clearly visible in the recordings. That part of the measurement is filtered out and will not be used. The time displayed by the instruments is in UTC (Coordinated Universal Time). The local time, in the Dutch coastal zone, is UTC plus one hour. During the summer (from end of March till end of October) the local time is UTC plus two hours.

3.2.3 Data processing

The CTD and the ADCP sensors create output files with raw data. The type of file differs between the instruments. Raw data is erratic and needs to be processed before it can be used. After processing netCDF files [1] are created. These are used for the analysis. A few important steps in the process of creating these files are described below.

The OBS measures backscatter of light emission in the water column. The OBS sensor of the Siltprofiler is calibrated in FTU (Formazin Turbidity Units), commonly used to express turbidity. The OBS-signal in Volts is transformed by the software of the instrument. The OBS sensor of NIOZ gives an output in Volts. For the analysis it is necessary to compute the concentration of SPM in mg/l from the output of the instruments. The calibration of the instruments is indicated below. Niskin bottles are used to take water samples, one below the sea surface and one above the sea bed at specific locations. Subsamples, with a certain volume, are taken, filtered with Whatmann GF/F glass fiber filters with 0.7 micrometer pore size, and dried. The concentration of SPM in mg/l is calculated from these samples. The backscatter measured with the OBS is compared with the samples. A regression of the lab-values on the OBS values is carried out. The resulting regression equation is applied to all measured data. The regression equation differs per instrument and may depend on season and location. The calibration formula's based on the samples of the 13th of October 2011 are:

$$\begin{aligned} SPM_{PoR} &= 0,9007 * OBS_{PoR} + 2,7689 \\ SPM_{Nioz} &= 25,3547 * OBS_{Nioz} + 1,4981 \end{aligned} \tag{3.1}$$

Figure 3.4 shows the calibration graph of the PoR and the NIOZ calibration.

Using the altimeter and pressure data the distance above the bed is calculated, by applying a linear regression. The data is filtered, i.e. missing data and peaks are removed. In case of missing altimeter data (e.g. NIOZ) the height above the bottom is determined based on measured pressure

[1] Network Common Data Form (NetCDF) is according to the Unidata website: "a set of software libraries and self-describing, machine-independent data formats that support the creation, access, and sharing of array-oriented scientific data" (http://www.unidata.ucar.edu/).

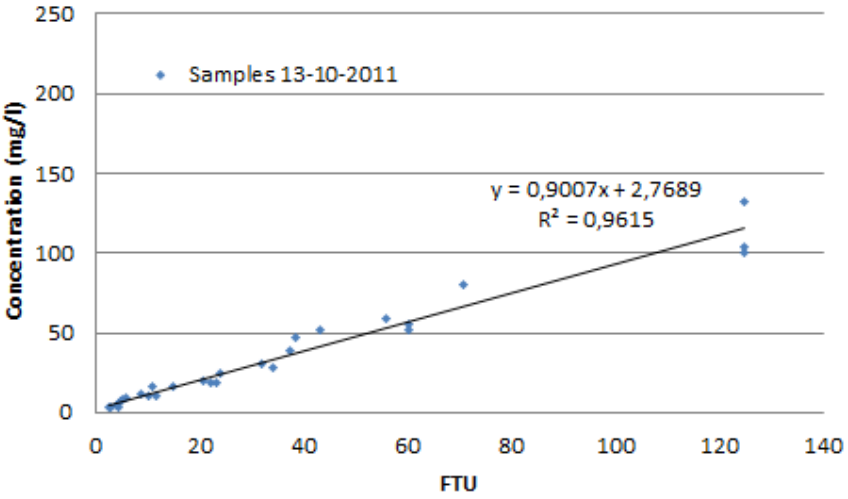

(a)

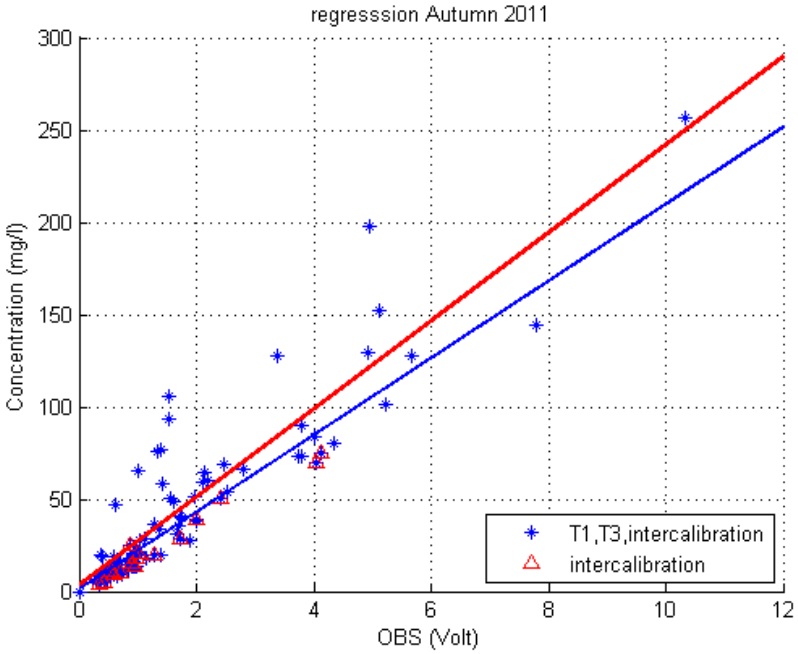

(b)

Figure 3.4: Calibration graphs for (a) PoR and (b) NIOZ at the 13th of October 2011 for the determination of SPM

only.

The data are processed step wise by the processing routine for the CTD (and OBS) sensor used by the Port of Rotterdam, which is also used to process the NIOZ-data. The data are stored at different levels of processing:

- Level 0, is the unprocessed original data per sensor. The measured quantities and the sensor settings.
- For level 1,spikes are removed, conductivity is converted into salinity, the up and downcast are filtered out and stored in a variable (as a mask) and the altitude is determined.

- For level 2, the backscatter data is transformed into concentration SPM (mg/l), data is processed and two types of netCDF files are produced for the downcast as well as for the upcast. Peaks are removed first and the first type of netCDF files are made. A second type of netCDF files is created by averaging the data within bins of 5 cm.

The ADCP data obtained is smoothed already by the software and stored in bins of 50 cm and in netCDF-files:

- Level 0 netCDF files are made based on the raw velocity data, absolute velocities and directions.
- For the level 1 files the direction and velocities are converted into north and east velocities and the up and downcast are captured in a variable.
- At level 2, the average and standard deviation of the velocities in all ensembles during the downcast and during the upcast burst are stored in the original 50 cm bins. The values are transformed to altitude above bottom instead of depth with respect to water surface.

The processed netCDF level 2 files are used for this study.

The netcdf level 2 files contain the down- and upcast. The average of both is taken for this study. This decision is made based on the comparison between down- and upcast of the different profiles. For the analysis missing values are replaced by linear interpolation with depth. However, the data shows also missing values at the top and the bottom of the profiles, which differ per transect. The data can now be used to make cross-sectional plots. Between the different measuring stations the data is linearly interpolated. Figures 4.2 through 4.15 show these plots. The dotted lines are the measurement stations.

The NIOZ data is processed into netCDF files with the same processing method as the Siltprofiler data. This gives some problems. PoR uses an altimeter to determine the height above the bottom. NIOZ does not use an altimeter. Determination of the height above the bottom for NIOZ is derived as follows. The pressure when the CTD touches the sea bottom is estimated from the pressure against time graph. At that moment the CTD is ca. 50 cm above the bed and the OBS is 1 m above the bed. Using these values the pressures are converted to height above seabed.

3.2.4 Intercalibration

On Friday the 14th of October 2011 both transects were sailed again, but now with two ships at the same transect, next to each other. Calibration measurements were performed to compare the values of the sensors used. The instruments of PoR and NIOZ were lowered at the same moment with a distance between the ships as small as possible. The obtained data is used to compare the sensors used by PoR and NIOZ (CTD, OBS and ADCP sensors). Differences between devices are observed. A correction for the deviation of the devices is required. This section describes the steps taken for the intercalibration.

The sensors of PoR and NIOZ (conductivity, temperature and OBS sensor) are calibrated individually by technicians of the company or in the factory. As explained in subsection 3.2.3 an OBS sensor is calibrated during a measurement campaign with use of water samples. Both parties have their own laboratory method to determine the concentration of the samples. To check the SPM laboratory values water samples were exchanged. For the comparison each of the samples at the 13th of October 2011 was divided over two bottles of which one was exchanged and the other is kept for analysis by the one who did the profile measurement. Figure 3.5 shows the relation between the determined laboratory concentrations. The laboratory values of both methods are in agreement. A deviation of 10 % between the laboratory method of PoR and NIOZ is observed, but this may be due to the sample with the highest concentration only (leaving this one out, gives even a better relation). It can be concluded that the deviation is small enough to use the laboratory

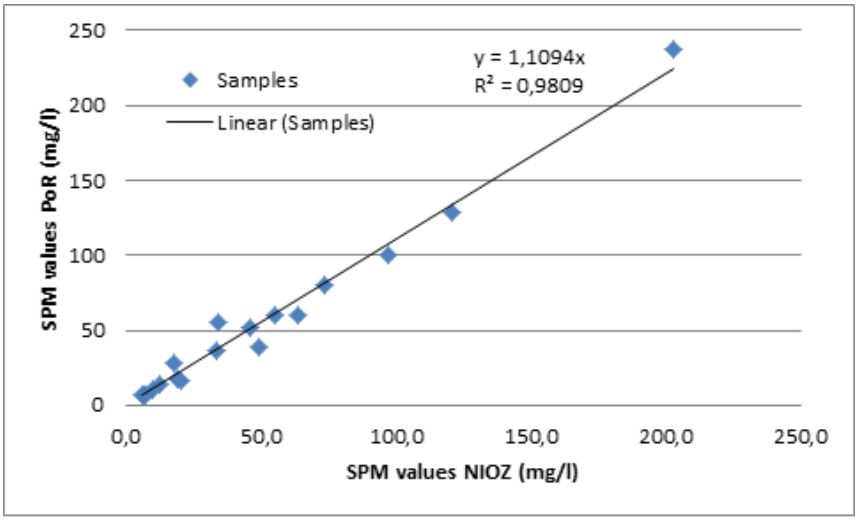

Figure 3.5: The SPM values determined by PoR and NIOZ to compare their laboratory methods. On the vertical axis the determined values by PoR are presented, on the horizontal axis the values by NIOZ. The values are fitted linear and give a deviation of about 10 %.

values for the calibration of both OBS sensors.

The next step of the intercalibration is the comparison of the resulting data of the sensors (after calibration). Figures 3.6 and 3.7 show the values of temperature, salinity and SPM of PoR and NIOZ for the southern and northern transect respectively. The temperature and salinity data of PoR shows more variation. NIOZ presents a smoother signal. NIOZ has a pumping system near the CTD sensor, this could explain the difference in spreading of the data between NIOZ and PoR. Figures 3.6 and 3.7 show that the salinity values, computed from the conductivity and temperature sensors of PoR and NIOZ are in agreement. The temperature values differ ca. 0.5 degree C, this difference is observed at both transects. The NIOZ temperature sensor is calibrated on the 23th of June 2011 and checked with surface CTD values. Therefore temperature values of NIOZ are assumed to be correct. The PoR temperatures are corrected with 0.5 degree C.

The SPM values show large differences between PoR and NIOZ, especially at the southern transect. For both transects, NIOZ measured much lower values of SPM at the onshore stations. Offshore the difference is less. The low values measured by NIOZ are in contradiction to high values found in the water samples collected that day. To get more insight in the deviation between both sensors values of PoR and NIOZ are plotted against each other. Figure 3.9 shows the values of NIOZ against the values of PoR for the Southern transect. The relation for the Northern transect is presented in figure 3.8. At both transects, the offshore stations have a better fit than the onshore stations. The relations seem close to linear. Onshore the relation between PoR and NIOZ show a variety in slope, no distinct relation is visible. This holds for the Southern as well as the Northern transect. A proper calibration formula between the two OBS sensors which holds for all the stations could not be defined. For now the SPM values for the 13th of October 2011 are therefore only analyzed qualitatively.

The intercalibration between the OBS sensors of PoR and NIOZ is extra challenging because of the problems with the correct depth determination for the NIOZ data (as explained in subsection 3.2.3). On top of this, the shape of the profiles are different and do not fit correctly on top of each other. An interesting question is what happened during the measurements? A possible cause could be SPM clouds, but it is doubtful if the different slopes in the profiles can be caused by SPM clouds. Another option could be a change in the tuning of the OBS sensor of NIOZ.

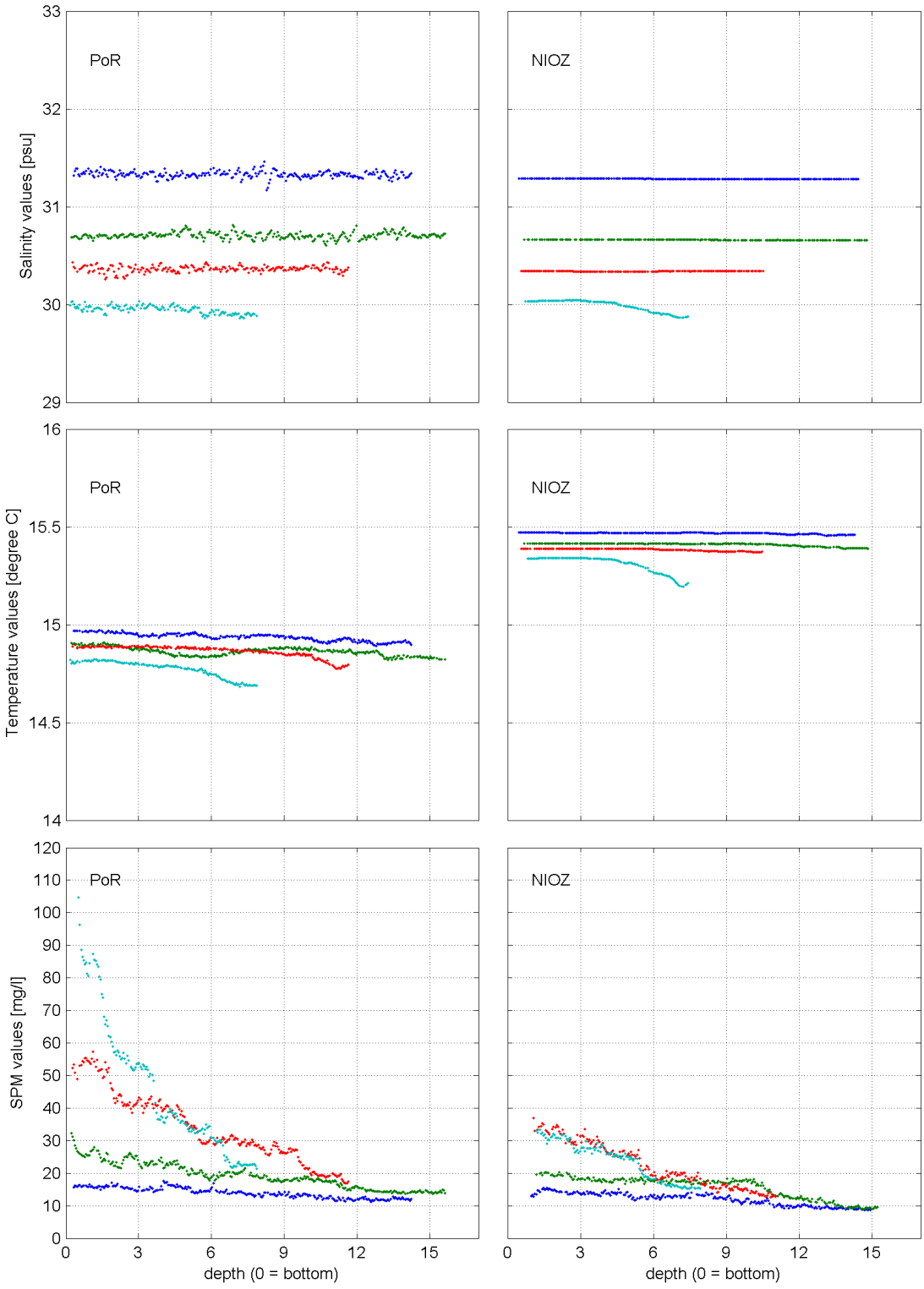

Figure 3.6: Salinity, temperature and SPM values measured by the sensors of NIOZ and PoR are presented at the Southern transect. The horizontal axis gives the depth, where z = 0 is the bottom. On the left side the values of PoR are shown, on the right the values of NIOZ.

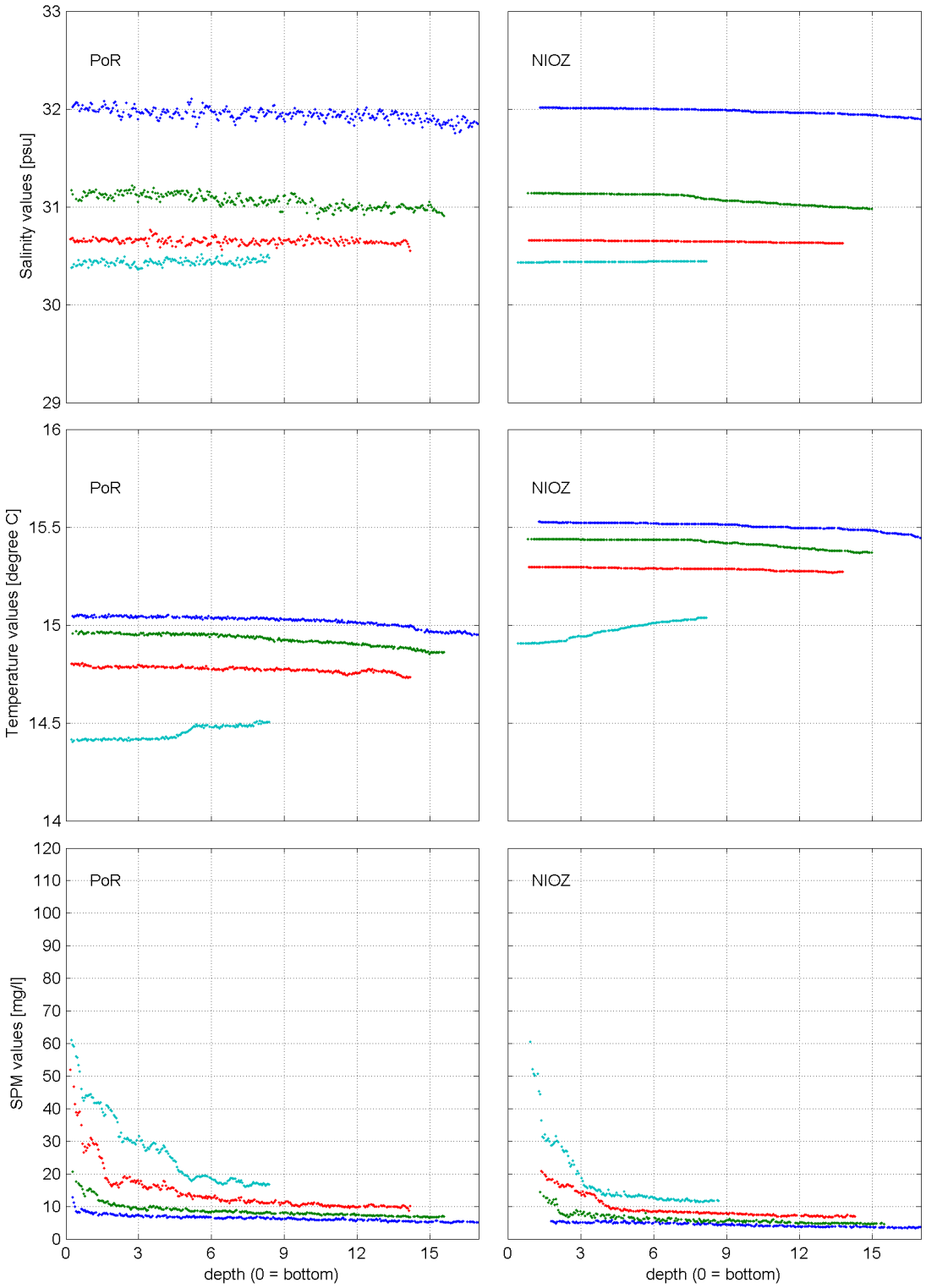

Figure 3.7: Salinity, temperature and SPM values measured by the sensors of NIOZ and PoR are presented at the Northern transect. The horizontal axis gives the depth, where z = 0 is the bottom. On the left side the values of PoR are shown, on the right the values of NIOZ.

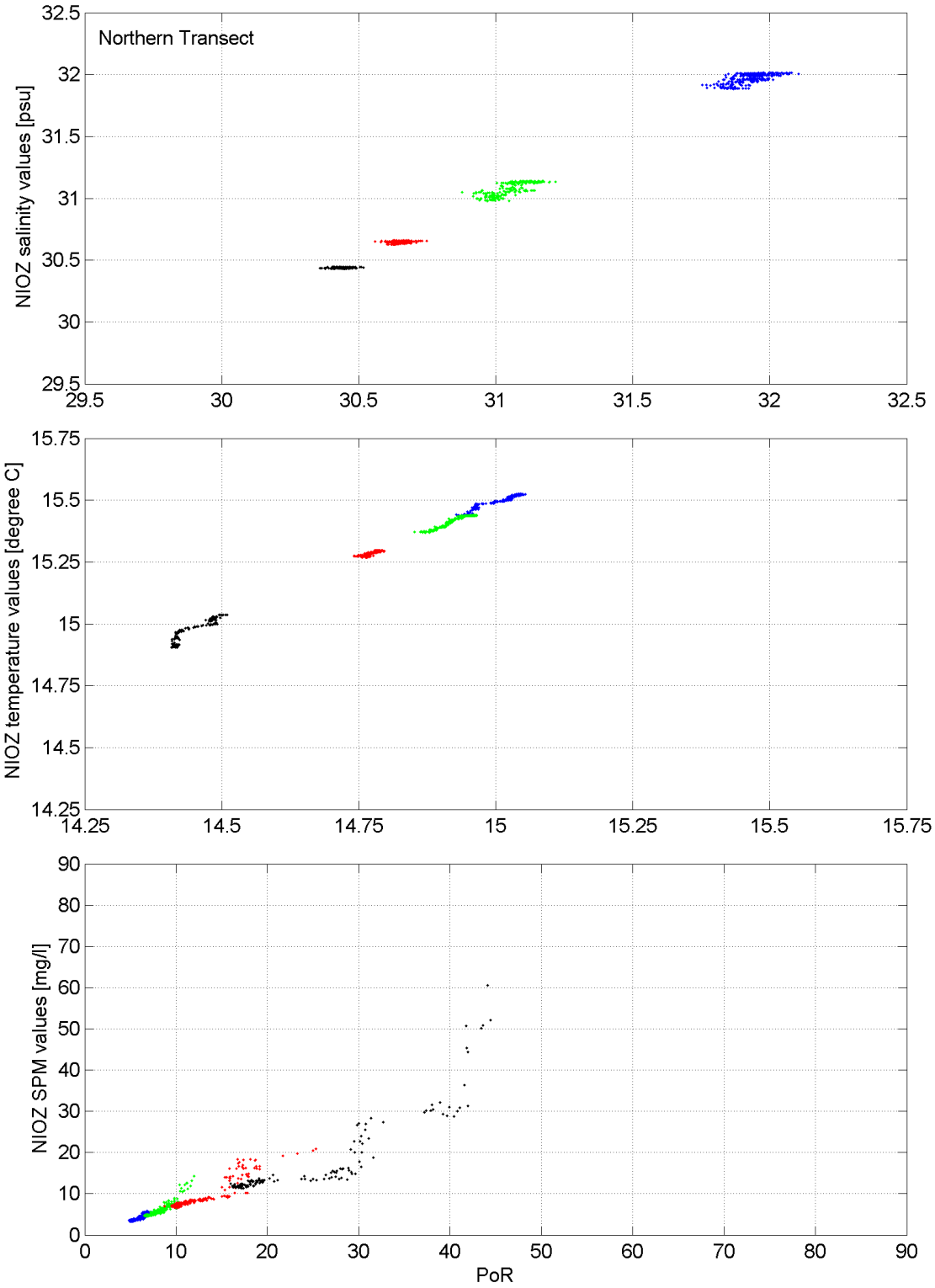

Figure 3.8: Relation between SPM values of PoR and NIOZfor the Northern transect. Black is 1 km offshore, red 2 km, green 4 km and blue 8 km.

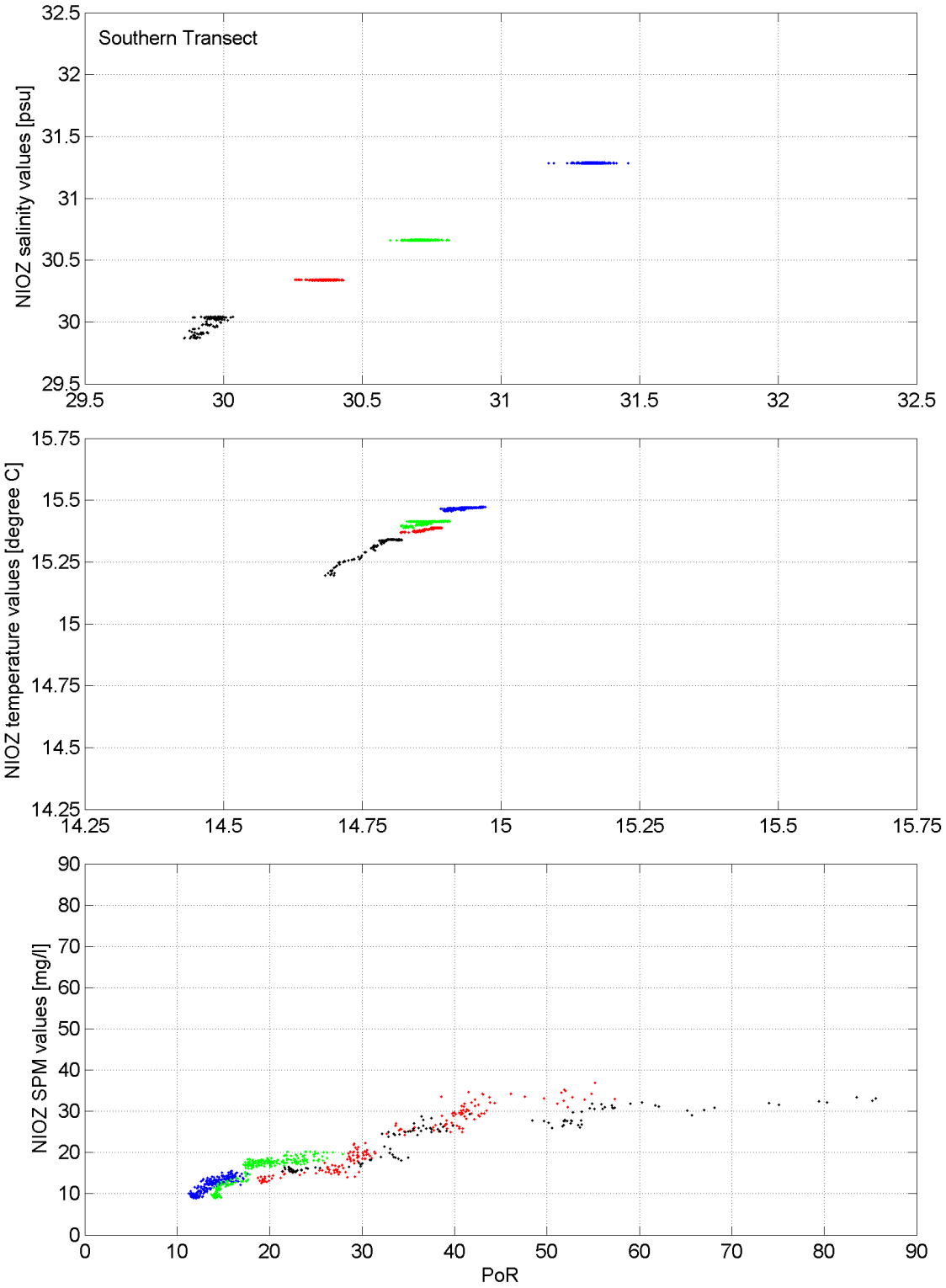

Figure 3.9: Relation between SPM values of PoR and NIOZ for the Southern transect. Black is 1 km offshore, red 2 km, green 4 km and blue 8 km.

3.2.5 Conditions

For the analysis of the time series on the 13th of October 2011 the weather conditions are important. Wind, waves, tide and river discharge are important factors for the Dutch coastal region. The river discharge is a stratifying component, it works as a buoyancy force in the North Sea, while the energy of wind, waves and the tide are tending to de-stratify the water column. The wind data is obtained from the KNMI database (www.knmi.nl) and the data of the waves, tide and discharges are obtained from the database of Rijkswaterstaat (www.waterbase.nl).

The measurement sequence started just after high water and ended after the next high water. An entire semi-diurnal tidal cycle is captured during the measurement campaign. The tidal levels of the 13th of October 2011 are shown in figure 3.11. The measuring stations at IJmuiden and Petten Zuid give an impression of the tidal height at the locations of the two transects. Section 2.4.1 discusses the deformation of the tide along the Dutch coast as a result of bottom friction. This phenomenon is clearly visible in figure 3.11 between IJmuiden and Petten. Based on this figure it can be concluded that the tidal height of the two transects is slightly different. Figure 3.10 shows the tidal levels during the month of October. This gives information about the phase in the spring-neap tidal cycle. At the 13th of October 2011 the semi-diurnal tidal ranges are around 1.25 and 1.50 meters. On the 14th of October 2011 the maximum tidal ranges are found of about 1.75 m. Spring tide seems to be at the 14th of October 2011. Thus, the measurements took place one day before spring tide.

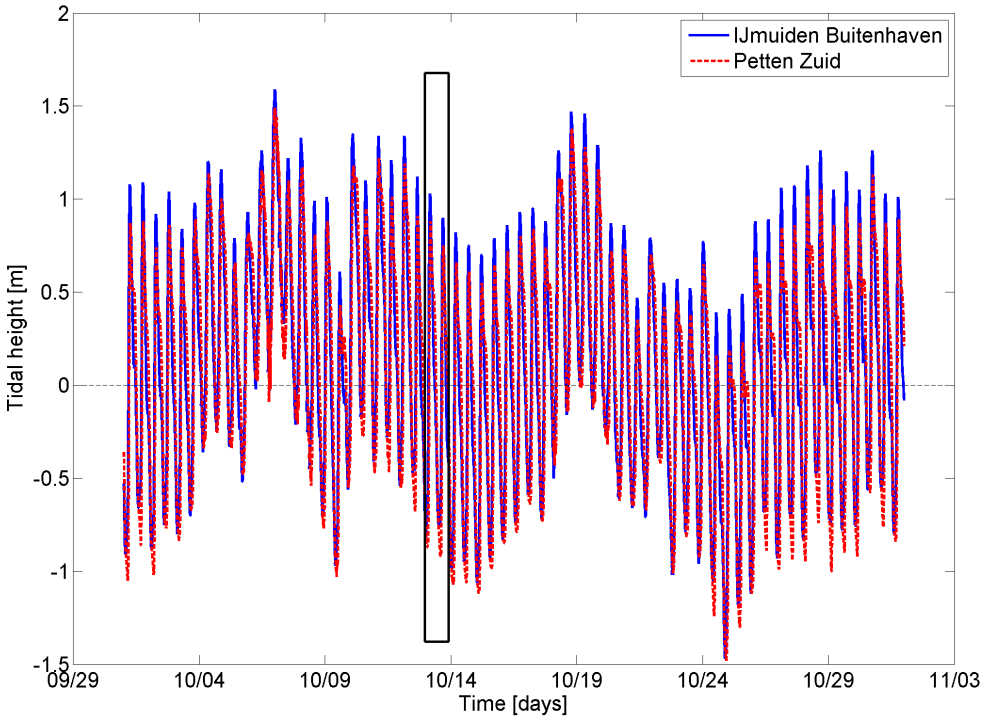

Figure 3.10: The tidal elevation in the month October 2011. The red line is the tide measured at Petten Zuid and the blue line at IJmuiden (www.waterbase.nl)

During Thursday the 13th of October the wind velocity was between 3.75 and 4.5 m/s. The wind direction varied between 45 and 115 degrees, viz. from a northeastern and easterly direction (see figure 3.14). The days before were windy, with wind velocity peaking around 12 m/s. Strong winds significantly influence the fresh water plume (Van Wiechen, 2011; Pietrzak and De Boer, in prep.). Their work states that Ekman Dynamics have more influence on the movement of the plume than

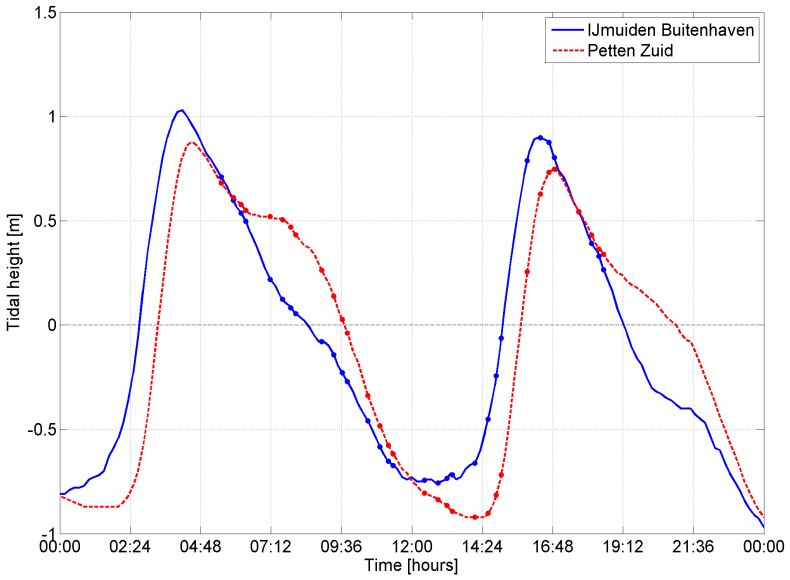

Figure 3.11: The tidal elevation at the 13th of October 2011. In blue the tide at IJmuidenhaven. In red the tide at Petten Zuid. The symbols show the times of the measurements. The tidal height at time of measurements is between the red and blue symbol. The tidal information is obtained from (www.waterbase.nl)

the frictional component (this holds during stratified conditions). The days before the measurements, the wind direction was west and south-west. Based on Van Wiechen (2011) and Pietrzak and De Boer (in prep.) the plume is expected to be blown towards the coast and become thin and well-mixed over the vertical. At the 12th, the day before the measurements, the wind was east with low wind velocity. Easterly winds push the plume offshore and northwards. Since the velocities were low (< 5.0 m/s) and one day before spring tide, the contribution is small but some movement is expected. Figure 3.12 indicates the possible direction of the plume as a response of the wind on the days before the measurement campaign. Figure 3.13 gives an indication of the state of the water column at the start of the measurements based on the weather circumstances the days before.

The waves, were coming from the north, significant wave height was ca. 1.0 meter, and the wave period varied between 5.5 and 6.5 seconds. The days before, due to the heavy weather, significant wave heights higher than 2.5 meter occurred. The wave height and period are shown in figure 3.15.

Fresh river water is discharged into the North Sea at several locations along the Dutch coast. The Rhine and Meuse are discharging into the North Sea via the New waterway and the Haringvliet in the south-west of the Netherlands, causing a freshwater plume in front of the coast. The Haringvliet is closed off by a barrier and discharges water intermittently in the North Sea. The mean discharge for both rivers is around 1600 m^3/s and 700 m^3/s respectively. The total discharge depends on the season and fluctuates during the year. In figure 3.16 the discharge for the New Waterway,the Haringvliet and the total discharge are displayed for the month of October 2011. The discharges are calculated with a model. The daily average discharge is displayed at noon. The discharge at the 12th of October is 1500 m^3/s and on the 13th it is 1750 m^3/s. During low water the North Sea Channel at IJmuiden sluices amounts of freshwater at irregular intervals into the North Sea (figure 3.16). The discharge was 126 m^3/s on the 12th of October and 121 m^3/s on the 13th of October.

The residual tidal current is about 3 cm/s at the Belgium coast and 12 cm/s near Texel (de Kok, 2004). According to these velocities it takes bout 15 to 20 days for the river water to reach the transects, depending on the actual residual velocity and the conditions during the days. The discharge from the North Sea Channel at IJmuiden needs about 1.5 day to reach the Southern transect.

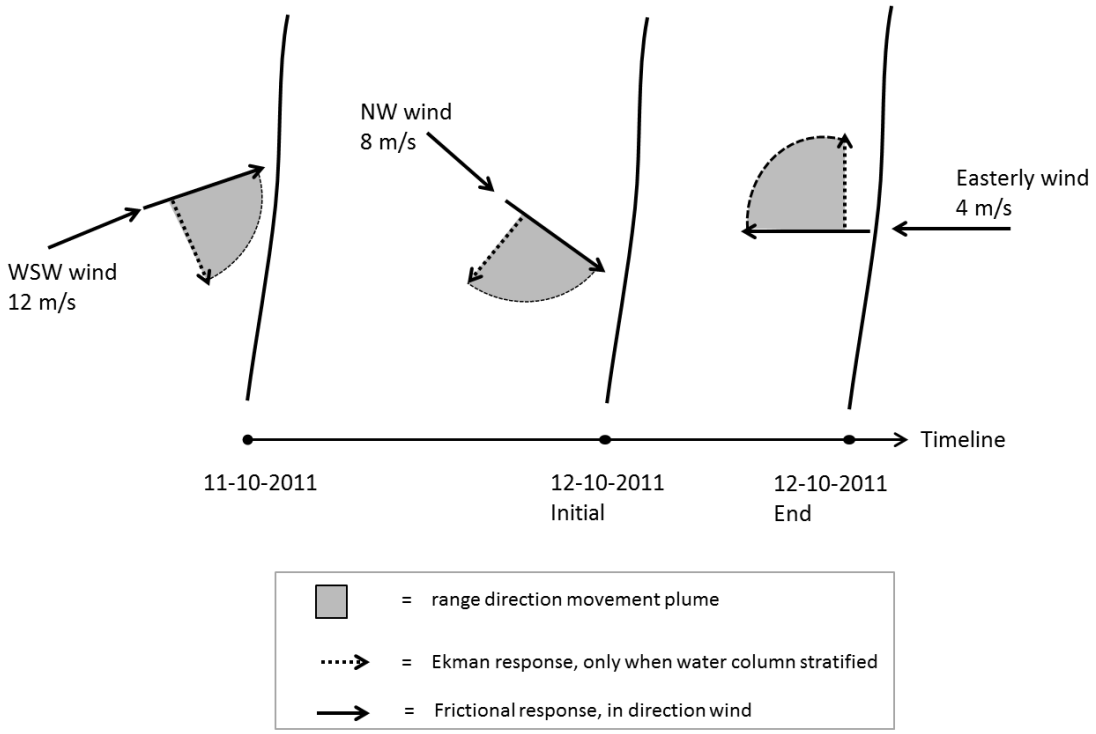

Figure 3.12: A cartoon of the expected influence of the wind on the movement of the plume the days before the measurement campaigns. The plume is pushed anyway in the direction of the wind. The black arrow represents the direction of the frictional component of the wind, the dotted arrow is the maximum direction of the Ekman response. The grey area indicates the range of the possible direction for the plume to move, depending on the reaction of the Ekman response.

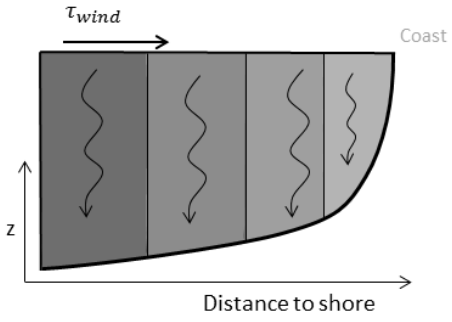

Figure 3.13: A sketch of state of the water column at the start of the measurements is presented. As a result of the high wind speeds, large stirring energy is present to mix the water column over the vertical. This results in a well-mixed water column, with less saline water in a small band close to the coast.

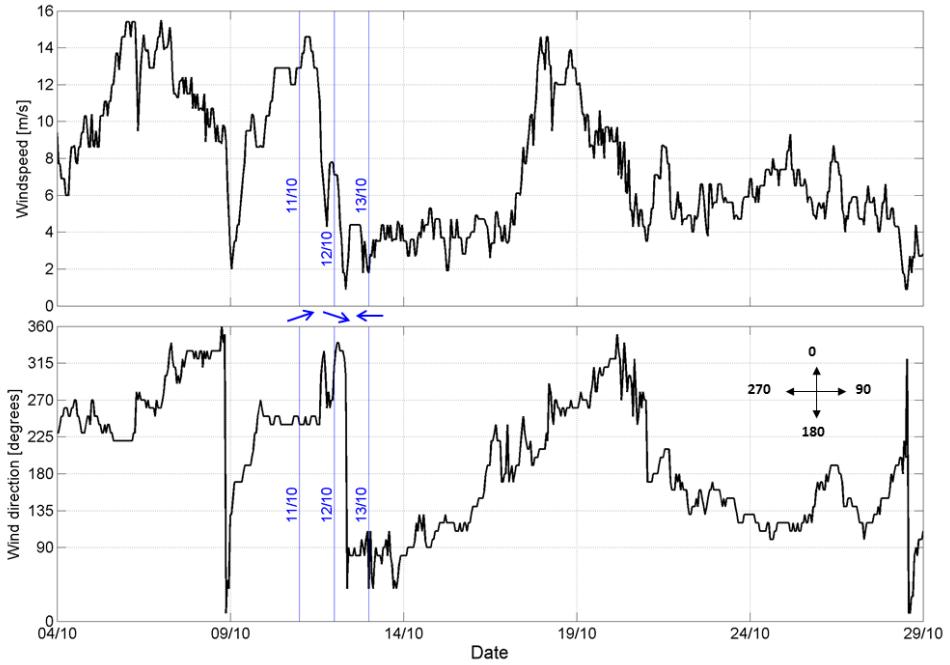

Figure 3.14: The upper panel shows the wind speed. The lower panels shows the wind direction. Both data is collected from a measuring station near IJmuiden during the month October in 2011. The 11th, 12th and the 13th of October are indicated in the figure (www.knmi.nl)

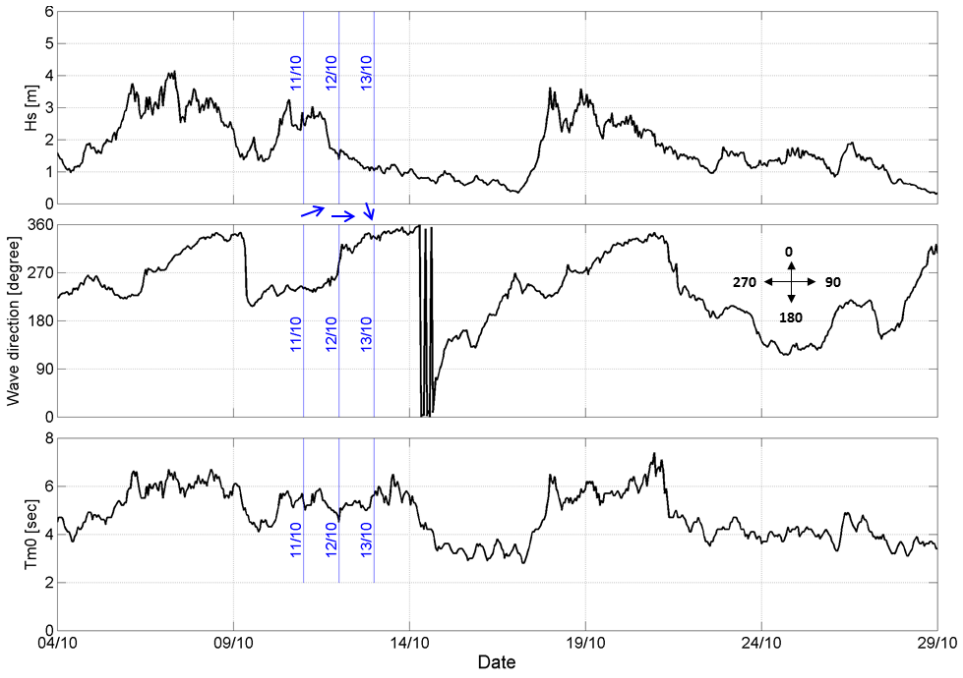

Figure 3.15: The upper panel shows the significant wave height, Hs. The middle panel shows the direction were the waves come from and the lower panel shows the wave period, Tm0. The data is collected from a measuring station near IJmuiden during October 2011. The 11th, 12th and the 13th of October are indicated in the figure (www.waterbase.nl)

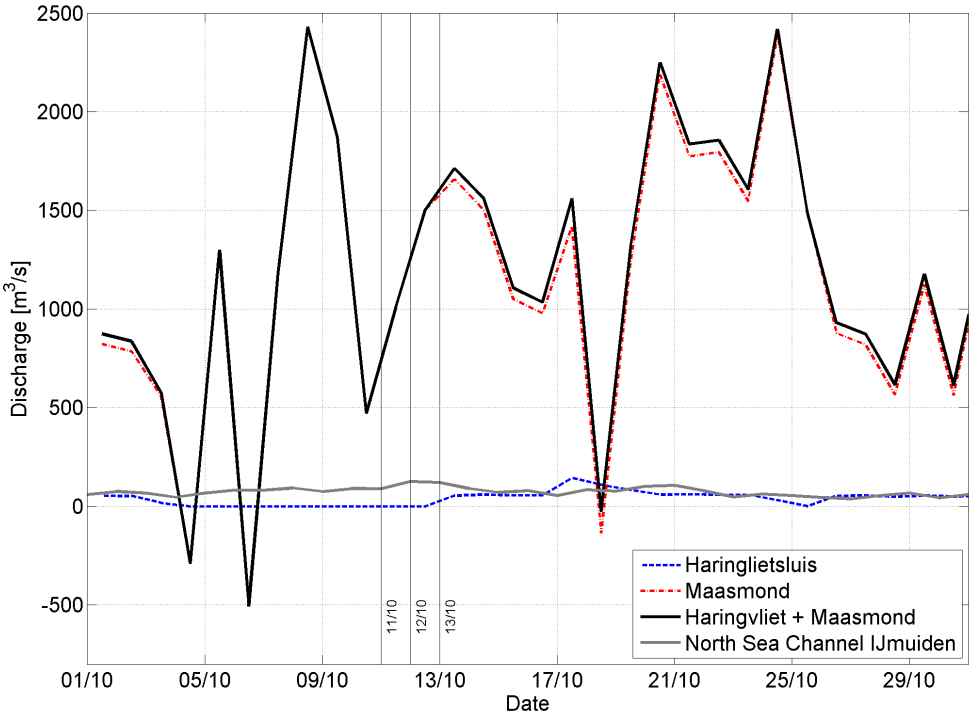

Figure 3.16: Discharges in 2011 during the month October. The discharge at the Haringvliet, Maasmond, the total of both and the discharge at the North Sea Channel at IJmuiden are shown. The discharges are measured at 12.00 each day. The total discharge of the Haringvliet and Maasmond on the 12th at 12.00 is 1500 m^3/s. On the 13th it is 1750 m^3/s. The North Sea Channel discharges 126 m^3/s on the the 12th of October and 121 m^3/s on the 13th of October (www.waterbase.nl).

3.3 Potential Energy Anomaly Analysis

The potential energy anomaly can be used for the analysis of data with respect to the onset and breakdown of stratification. Background on this parameter can be found in section 2.3, where the potential energy anomaly, φ [J/m^3], is defined as

$$\varphi = \frac{1}{H}\int_{-h}^{\eta}(\bar{\rho}-\rho)gzdz \tag{3.2}$$

The time rate of change of φ [W/m^3] is described as

$$\frac{\partial\varphi}{\partial t} = \frac{g}{H}\int_{-h}^{\eta}\frac{\partial(\bar{\rho}-\rho)}{\partial t}zdz \tag{3.3}$$

which is the potential energy anomaly equation. Where $H = h + \eta$ is the total water depth [m], h the distance between the bed and the mean water level [m], η is the free surface [m], g is the gravitational acceleration (9,81 m^2/s), z is the depth interval [m], ρ is the water density [kg/m^3] and $\bar{\rho}$ the depth averaged density. These two parameters (φ and $\frac{\partial\varphi}{\partial\varphi}$) are calculated for both transects using the measured temperature, salinity and pressure data. The φ gives the depth averaged amount of energy required for complete mixing of the water column, indicating if the water column is stratified ($\varphi > 0$) or mixed ($\varphi = 0$). The change of φ in time can be determined for each station, at each transect. It is the difference in φ and time between the different tracks. Therefore seven

values for $\frac{\partial\varphi}{\partial\varphi}$ per station are obtained. Figure 3.17 shows how $\frac{\partial\varphi}{\partial\varphi}$ is obtained from the measurements. The change of the density profile is caused by advection, straining and vertical mixing. The three-dimensional Potential Energy Anomaly equation derived by De Boer et al. (2008), is used to investigate the importance of these processes. The reduction of the equation is explained in the next subsection.

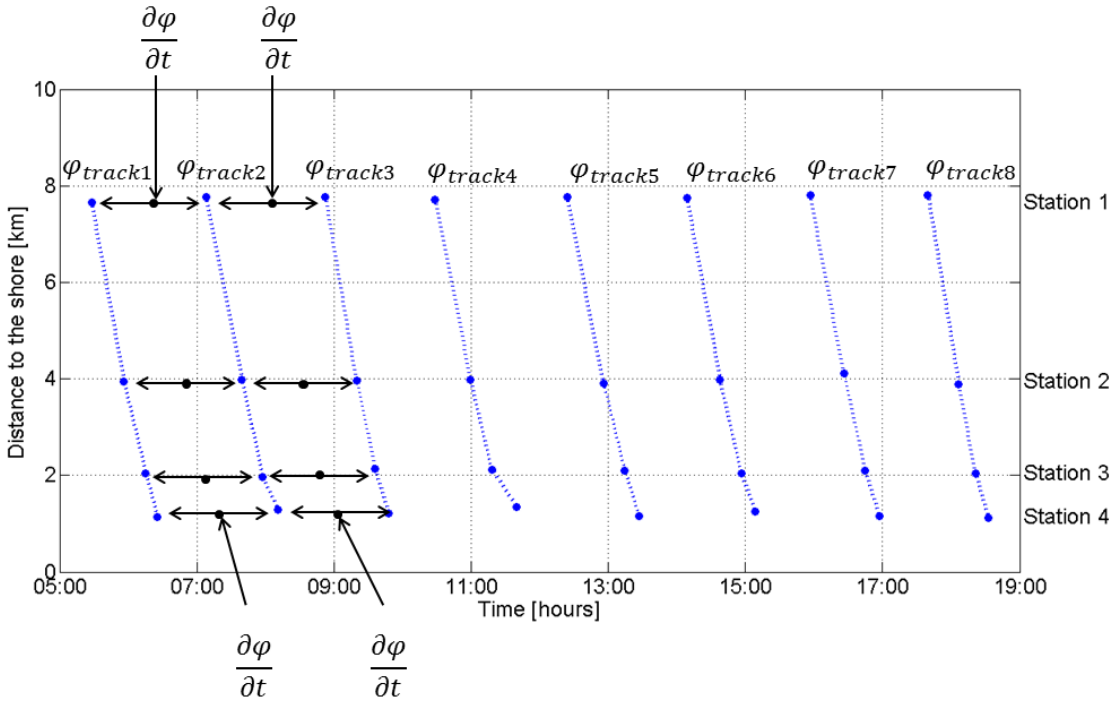

Figure 3.17: A schematic view of the determination of $\frac{\partial\varphi}{\partial\varphi}$ is shown. The eight tracks result in seven terms for $\frac{\partial\varphi}{\partial\varphi}$ for each measuring station.

3.3.1 Reduced form of the three-dimensional PEA Equation

The full three-dimensional equation is defined as

$$\begin{aligned}\frac{\partial\varphi}{\partial t} = \frac{g}{H}\int_{-h}^{\eta}\Bigg(&\underbrace{\tilde{u}\frac{\partial\bar{\rho}}{\partial x}}_{S_x}\underbrace{+\bar{u}\frac{\partial\tilde{\rho}}{\partial x}}_{A_x}\underbrace{+\tilde{u}\frac{\partial\tilde{\rho}}{\partial x}}_{N_x}\overbrace{-\frac{1}{H}\frac{\partial\overline{\tilde{u}\tilde{\rho}}H}{\partial x}}^{C_x}\overbrace{+w\frac{\partial\rho}{\partial z}}^{W_z}+\ldots\\ &\underbrace{\tilde{v}\frac{\partial\bar{\rho}}{\partial y}}_{S_y}\underbrace{+\bar{v}\frac{\partial\tilde{\rho}}{\partial y}}_{A_y}\underbrace{+\tilde{v}\frac{\partial\tilde{\rho}}{\partial y}}_{N_y}\underbrace{-\frac{1}{H}\frac{\partial\overline{\tilde{u}\tilde{\rho}}H}{\partial y}}_{C_y}\underbrace{+\frac{\partial\langle\rho' w'\rangle}{\partial z}}_{M_z}\Bigg)zdz+\ldots\\ \int_{-h}^{\eta}\Bigg(&\underbrace{\frac{\partial\langle\rho' u'\rangle}{\partial x}}_{D_x}+\underbrace{\frac{\partial\langle\rho' u'\rangle}{\partial x}}_{D_y}-\frac{1}{H}\Bigg(\underbrace{\langle\rho' w'\rangle|_s}_{D_s}\underbrace{-\langle\rho' w'\rangle|_b}_{D_b}\Bigg)\Bigg)zdz-\underbrace{\frac{\varphi}{H}\frac{\partial\varphi}{\partial t}}_{B_H}-\underbrace{\left(\frac{g}{H}\right)\left(\rho(\eta)\eta\frac{\partial\eta}{\partial t}\right)}_{B_\eta}\end{aligned} \tag{3.4}$$

Where $\tilde{\rho}=\rho-\bar{\rho}$,$\tilde{u}=u-\bar{u}$ and $\tilde{v}=v-\bar{v}$ are the deviations from the depth mean values. u is the cross-shore velocity and v the velocity alongshore. An observational study has some limitations when compared with numerical modeling. Data is obtained at a certain location and time. Assumptions have to be made and the full three-dimensional equation will be simplified. The data set used in this research contains along- and cross-shore information. As a result the terms $\partial\bar{\rho}/\partial x$,

$\partial\tilde{\rho}/\partial x$, $\partial\bar{\rho}/\partial y$ and $\partial\tilde{\rho}/\partial y$ are known. Together with along- and cross-shore velocities, terms as S_x, S_y, A_x and A_y are calculated. Terms N_x,N_y,C_x and C_y are neglected because of complexity. Furthermore these terms are in the order of 10^{-5} - 10^{-10}, which is small compared to S_x, S_y, A_x and A_y. Especially the advection and straining terms are of interest. Moreover De Boer et al. (2008) demonstrated that the first four terms, advection and straining, give an acceptable estimate for the total change of φ in time.

Turbulence is not measured directly. Sirks (2012) showed that turbulence can be derived from a moving ADV (Acoustic Doppler Velocimeter). NIOZ did not use an ADV, thus the turbulent fluxes are unknown in their transect. For future research, it is recommended to derive turbulence from ADCP measurements as well. Consequently, bed and surface density fluxes are set to zero, the horizontal depth averaged dispersion terms (D_x and D_y) are discarded. The vertical mixing term, M_z is calculated analytically based on the mixing energy due to wind, waves and tide, following Simpson et al. (1990). Likewise, the up- and downwelling term (W_z) and the barotropic terms (B_H and B_η) are neglected for sake of simplicity.

As a result, the terms S_x, S_y, A_x, A_y and M_z remain. The simplified equation with the remaining advection, straining and estimated mixing terms becomes

$$\frac{\partial\varphi_t}{\partial t} \approx \frac{g}{H}\int_{-h}^{\eta}(\underbrace{\tilde{u}\frac{\partial\bar{\rho}}{\partial x}}_{S_x} + \underbrace{\bar{u}\frac{\partial\tilde{\rho}}{\partial x}}_{A_x} + \underbrace{\tilde{v}\frac{\partial\bar{\rho}}{\partial y}}_{S_y} + \underbrace{\bar{v}\frac{\partial\tilde{\rho}}{\partial y}}_{A_y})z\,dz + M_z \tag{3.5}$$

Where $\tilde{\rho} = \rho - \bar{\rho}$,$\tilde{u} = u - \bar{u}$ and $\tilde{v} = v - \bar{v}$ are the deviations from the depth mean values. u is the cross-shore velocity and v the velocity alongshore.

3.3.2 Determination of the separate terms

The resulting formula is applied to the study area. A spatial grid is defined based on the two transects. Figure 3.18 shows the grid. Each station represents a grid point. Four extra terms between the two transects, on the same distance from the coastline, are inserted. The grid consist of n by m grid points, where n are the points in cross-shore direction and m the points in along-shore direction. The points (n,1) and (n,3) contain the measured density and velocity data. The determination of the different terms from equation 3.5 on the grid are discussed below.

Alongshore terms

The alongshore terms,S_y and A_y, are calculated with the use of the two transects, in y-direction. These terms are located between the two transects, at m = 2. The partial derivative of ρ in y direction is calculated as follows:

$$\frac{\partial\rho}{\partial y} \approx \frac{\Delta\rho_{n,m}}{\Delta y_{n,m}} = \frac{\rho_{n,m+1} - \rho_{n,m-1}}{y_{n,m+1} - y_{n,m-1}} \qquad \text{for m = 2} \tag{3.6}$$

The alongshore velocity is calculated between the Northern and Southern transect as well. This is done by averaging the velocities measured in both transects:

$$v_{n,m} = \frac{v_{n,m+1} + v_{n,m-1}}{2} \qquad \text{for m = 2} \tag{3.7}$$

Using of equations 3.6 and 3.7 S_y and A_y are displayed on the grid points (n,2), between the two transects.

Cross-shore terms

The determination of the partial derivative in x direction is more complicated than in y direction. For each point on the two transects (m = 1,3) the partial derivative in x direction is determined. Four stations with data are available in x direction, which results in three derivatives, located between the grid points. For the analysis the $u\frac{\partial\rho}{\partial x}$ need to be determined at the same places as

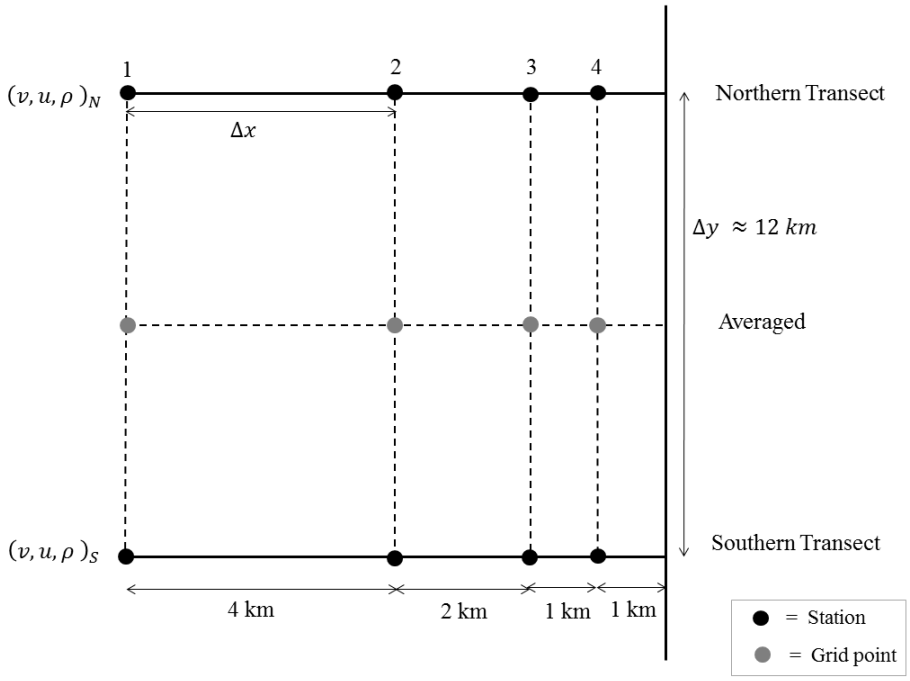

Figure 3.18: A schematic view of the two transects is shown. Both at the Northern and Southern transects density (ρ) and velocity data (v,u) is available at four points. The change of density in alongshore and cross-shore direction is reflected between the two transects. The black points represent the stations. The grey points are grid points, the average between the Northern and Southern transect.

$v\frac{\partial \rho}{\partial y}$. Equations 3.8 and 3.9 show how a derivative is derived at the four grid points. Equation 3.8 calculates the derivative on the middle two points, n = 2,3. For example the determination of $\frac{\partial \rho}{\partial x}$ for point 2 is based on the density difference between point 1 and 3. The same principle holds for point 3, which is based on the difference between point 2 and 4. Equation 3.9 determines the derivatives on the two corner points, n = 1,4. The calculation of $\frac{\partial \rho}{\partial x}$ for point 1 for example is based on the density difference between point 1 and 2. Unfortunately, the method leads to an error, which is discussed later in this section. When all the derivatives are determined at m = 1,3, the derivatives at m = 2 can be calculated with equation 3.10.

$$\frac{\partial \rho}{\partial x} \approx \frac{\Delta \rho_{n,m}}{\Delta x_{n,m}} = \frac{\rho_{n+1,m} - \rho_{n-1,m}}{x_{n+1,m} - x_{n-1,m}} \qquad \text{for n = 2,3 and m = 1,3} \tag{3.8}$$

$$\frac{\partial \rho}{\partial x} \approx \frac{\Delta \rho_{n,m}}{\Delta x_{n,m}} = \frac{\rho_{n+1,m} - \rho_{n,m}}{x_{n+1,m} - x_{n,m}} \qquad \text{for n = 1,4 and m = 1,3} \tag{3.9}$$

$$\frac{\partial \rho}{\partial x} \approx \frac{\Delta \rho_{n,m}}{\Delta x_{n,m}} = \left(\frac{\Delta \rho_{n,m+1}}{\Delta x_{n,m+1}} + \frac{\Delta \rho_{n,m-1}}{\Delta x_{n,m-1}}\right) \qquad \text{for n = 1:4 and m = 2} \tag{3.10}$$

The cross-shore velocity is calculated for each grid point (n,m). Therefore for m = 2 the velocity can be determined as

$$u_{n,m} = \frac{u_{n,m+1} + u_{n,m-1}}{2} \qquad \text{for m = 2} \tag{3.11}$$

S_x and A_x are determined on each grid point (n,m). Both equations (equation 3.10 and 3.11) form the cross-shore straining and advection terms on m = 2. These terms are used in the simplified PEA equation (3.5).

Mixing terms

Vertical mixing, M_z, is determined based on analytic formulations defined by Simpson et al. (1990). The mixing components which are taken into account in this analysis are wind, waves and tide.

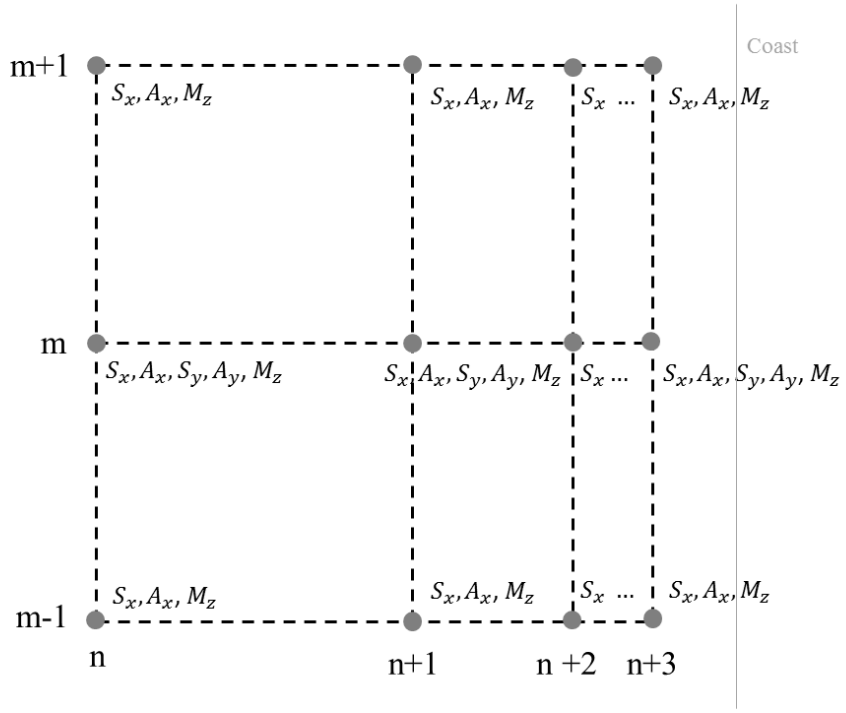

Figure 3.19: The grid based on the study area. The grey points indicate the grid points.

Therefore, three vertical mixing terms are derived. Each of these terms is discussed below.

The tidal mixing energy can be defined as

$$\frac{\partial \varphi_{tide}}{\partial t} = -\epsilon k \rho_{n,m} \left(\frac{|\overline{u}^3_{n,m}|}{h_{n,m}}\right) \tag{3.12}$$

Where ϵ is a coefficient of efficiency for mixing, k is an effective drag coefficient for bottom stresses, ρ is the water density, h is the water depth and $\overline{u}$ is the depth mean tidal current.

The wind exerts a horizontal load on the water surface, which introduces kinetic energy in the surface layer, enhancing mixing over the vertical. The mixing due to the wind can be approximated with

$$\frac{\partial \varphi_{wind}}{\partial t} = -\delta k_s \rho_a \left(\frac{\overline{w}^3}{h_{n,m}}\right) \tag{3.13}$$

Where δ is a coefficient of efficiency for mixing, k_s is an effective drag coefficient for surface stresses, ρ_a is the air density (kg/m^3), h is the water depth and w is the wind velocity in m/s.

In shallow water, like the Rhine ROFI, stirring caused by waves significantly contributes to mixing. This term is more difficult to quantify, therefore Simpson et al. (1991) did not consider this term within their model. Due to the lack of an analytical definition Smolders (2011) derived a formula for the mixing energy of waves which is defined as

$$\frac{\partial \varphi_{waves}}{\partial t} = -\tau_w \epsilon \frac{U_w}{h_{n,m}} = -0.5 \rho_{n,m} f_w \epsilon \frac{U_w^3}{h_{n,m}} \tag{3.14}$$

Where τ_w is the bed shear stress, U_w the orbital velocity near the bed and ϵ a coefficient of efficiency for mixing, based on the tidal current. The derivation and reasoning of equation 3.14 can be found in appendix A.

The constants for the mixing equations are based on Simpson et al. (1991), specified as:

$$\begin{array}{ll} \delta = 0.039 & \epsilon = 0.0065 \\ k_s = 6.4 \times 10^{-5} & k = 0.0025 \end{array} \tag{3.15}$$

The mixing efficiency ϵ is based on Smolders (2011). The Rhine ROFI is shallower compared to the United Kingdom Shelf. In shallow areas mixing by tide and waves will be more dominant. Therefore the mixing efficiency is taken 0.0065 instead of 0.0038 (Simpson et al., 1991). The value is based on the condition $\delta \approx 6\epsilon$ (Simpson and Bowers, 1981).

Introduced Error

The determination of the different terms for the simplified PEA equation (3.5) introduces bias and errors, which can be divided into four different parts. Each error will be discussed. First bias is obtained by neglecting many terms from equation 3.4. Only the advection and straining terms remained. Therefore the bias is denoted as ε_{ASIPS}. The second error is because of the analytic approach for the mixing terms instead of M_z from equation 3.4. This error is defined as ε_{M_z}.

The third error is introduced for the change of time within the calculated cross-shore density difference, defined as ε_{time}. The determination of $u_{n,m}(\Delta\rho_{n,m}/\Delta x_{n,m})$ uses densities and velocities measured at different times, resulting into a local change over time. This error is explained by using the total derivative for the density:

$$\frac{D\rho}{Dt} = \frac{\partial\rho}{\partial t} + u\frac{\partial\rho}{\partial x} + v\frac{\partial\rho}{\partial y} + w\frac{\partial\rho}{\partial z} \tag{3.16}$$

In which $\frac{\partial\rho}{\partial t}$ is the change of density in time. The term $w\frac{\partial\rho}{\partial z}$, defined as advection in vertical direction, is not used in the analysis, therefore it is neglected here as well. The determination of $v\frac{\partial\rho}{\partial y}$ does not produce a change over time. Density and velocity at the different transects are measured at the same time. As mentioned before, the cross-shore derivative induces a local change over time, $\frac{\partial\rho}{\partial t} \neq 0$. Consequently, equation 3.16 results in

$$(\frac{D\rho}{Dt} - \underbrace{\frac{\partial\rho}{\partial t}}_{\neq 0}) = u\frac{\partial\rho}{\partial x}. \tag{3.17}$$

The change of time between the measurements is neglected here, causing bias.

For the determination of the cross-shore density terms, $\frac{\Delta\rho_{n,m}}{\Delta x_{n,m}}$, an assumption is made, introducing bias, ε_{grid}. The cross-shore terms are calculated with the equations 3.8 and 3.9. The calculated derivative for the corner points is displayed between point n and n+1 (figure 3.20(a)). This value is moved to point n. The determination of the derivative for the center points introduces bias as well, but much smaller. Equation 3.9 shows the calculation and figure 3.20(b) presents the movement of the terms.

The total error and bias is defined as

$$\varepsilon \approx \varepsilon_{ASIPS} + \varepsilon_{M_z} + \varepsilon_{time} + \varepsilon_{grid} \tag{3.18}$$

3.3.3 Simplified PEA Equation

In this section the three-dimensional Potential Energy Anomaly equation is reduced to a simplified form. The total simplified three-dimensional Potential Energy Anomaly equation, including

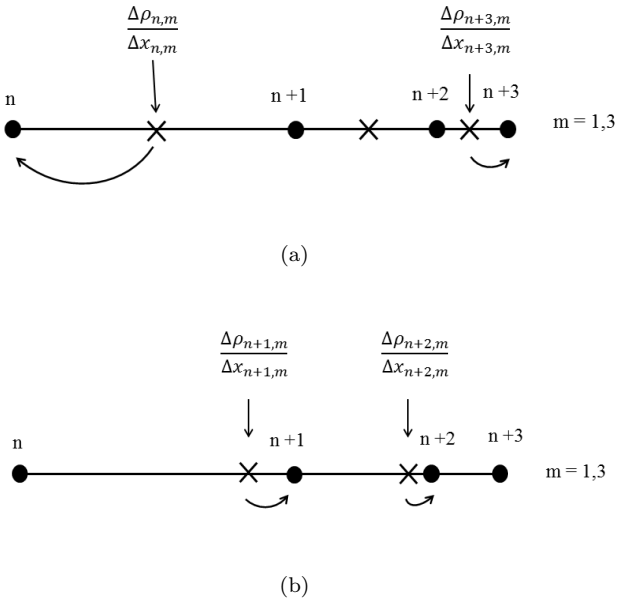

Figure 3.20: Schematisation of the determination of the cross-shore density differences. Bias is introduced because of staggering. The terms are moved, the direction is indicated by the arrow. Figure (a) shows the determination of the terms on the two corner points. Figure (b) shows the calculation of the terms on two center points.

straining, advection and stirring terms is

$$\frac{\partial\varphi_t}{\partial t} \approx \underbrace{\frac{g}{H}\int_{-h}^{\eta}(\tilde{u}_n, m\frac{\Delta\bar{\rho}_{n,m}}{\Delta x}_{n,m} + \bar{u}_{n,m}\frac{\Delta\tilde{\rho}_{n,m}}{\Delta x_{n,m}} + \tilde{v}_{n,m}\frac{\Delta\bar{\rho}_{n,m}}{\Delta y_{n,m}} + \bar{v}_{n,m}\frac{\Delta\tilde{\rho}_{n,m}}{\Delta y_{n,m}})zdz}_{ASIPS}$$
$$\underbrace{-\epsilon k\rho_{n,m}(\frac{|\widehat{u}^3_{n,m}|}{h_{n,m}}) - \delta k_s\rho_a(\frac{\overline{w}^3}{h_{n,m}}) - 0.5\rho_{n,m}f_w\epsilon\frac{U^3_w}{h_{n,m}}}_{M_z} + \underbrace{\varepsilon}_{error} \tag{3.19}$$

For n = 1:4 and m = 2. This formula is the basis of the Potential Energy Anomaly Analysis within this study. The formula can be simplified by renaming the different parts. The straining and advection terms are denoted with ASIPS and the vertical mixing components with M_z. The introduced error is defined as ε. With this simplification the equation becomes:

$$\frac{\partial\varphi_t}{\partial t} \approx ASIPS + M_z + \varepsilon \tag{3.20}$$

This simplified formula will be compared with the change of φ in time based on equation 4.1. This is done to check whether the introduced error is acceptable and to check if equation 3.20 can be applied for calculating the different cross- and alongshore processes (see section 4.5).

3.4 Tidal Analysis

Velocities are measured and split into along- and cross-shore velocity components. The measured velocity signal includes among others the tidal current, a time averaged velocity, influence of the wind stress and velocity residuals. To investigate the vertical tidal current structure an harmonic analysis is performed on the velocity data. The measurements lasted only 13 hours, therefore a tidal analysis is possible, but only one tidal cycle can be filtered. The tidal analysis for each transect is based on the entire set of velocity data. This is not entirely correct, because the measurements were implemented at different stations. Otherwise not enough data was present to

obtain a represented signal. Harmonic analysis is commonly used to predict the tide at a specific location. Fourier analysis is performed to filter harmonic tidal components from erratic data. A harmonic component is a sinusoidal signal with a certain frequency and amplitude. Each tidal constituent can be described as a harmonic component. In front of the Dutch coast 92 components are present which represents the tide. M_2 and S_2 are the largest tidal components and a good representation for the Dutch tide. This study makes use of the M_2 component, with a radial frequency of $\omega = 1.41 \times 10^{-4}$ rad/s. Both, M_2 and S_2, are not possible because of the short time period in combination with a small difference in frequency between both. The tidal components can be filtered with use of the measured velocity signal and the radial frequency of the tidal constituent, resulting in amplitudes, A_n, and phases, φ_n, for each component defined with n. The velocity signal can be defined as the sum of all harmonics as (figure 3.21):

$$u(t) = a_0 + \sum_{n=1}^{N} a_n cos(\omega_n t - \varphi_n) \tag{3.21}$$

where, $u(t)$ is the measured velocity, N is the number of harmonic components,a_0 represents the mean value, a_n is the amplitude of harmonic component number n, ω_n the frequency of harmonic component n, t the time and φ_n the phase of the signal of harmonic component n.

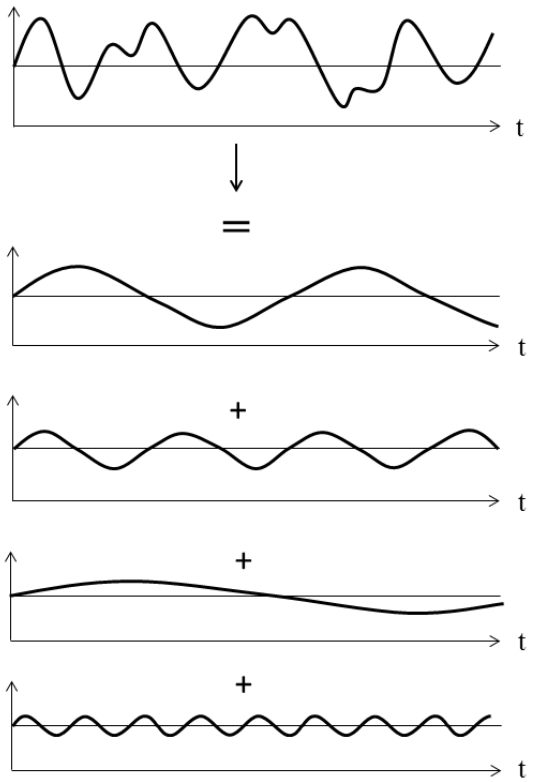

Figure 3.21: A measured signal, e.g. velocity or water elevation, can be defined as the sum of different harmonic components. These components can be filtered from the total signal with an harmonic analysis

For this study, first the M_2 tide is filtered. The measured velocity signal is then defined by:

$$u = u_{M_2} + R \tag{3.22}$$

where u is the measured velocity, u_{M_2} is the velocity of the M_2 tide and R is the velocity residual (not the alongshore residual velocity which is present along the Dutch coast).

The presence of cross-shore tidal currents induces tidal straining. The velocity vectors of the tidal current turn as ellipses. With use of the filtered M_2 velocity the tidal ellipse properties

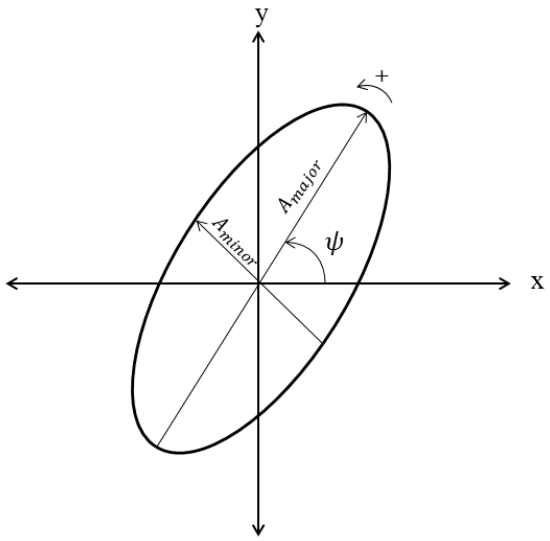

Figure 3.22: An ellipse with its properties, the vector turns positive in cyclonic (i.e. anti-clockwise) direction. The Inclination, major axis and minor axis are presented in the figure.

(e.g. parameters which indicate if the velocity vector rotates as a ellipse) can be defined. The M_2 velocity, u_{M_2}, can also be defined in the following way:

$$u_{M_2}(t) = \sum_{n=1}^{N} [a_n cos(\omega_n t) + b_n sin(\omega_n t)] \tag{3.23}$$

$$v_{M_2}(t) = \sum_{n=1}^{N} [c_n cos(\omega_n t) + d_n sin(\omega_n t)] \tag{3.24}$$

$$\tag{3.25}$$

where a through d are coefficients, which are used to derive the ellipse properties:

$$A_{major} = \frac{1}{2}|(a+d) + i(c-b)| + \frac{1}{2}|(a-d) + i(c+b)| \tag{3.26}$$

$$A_{minor} = \frac{1}{2}|(a+d) + i(c-b)| - \frac{1}{2}|(a-d) + i(c+b)| \tag{3.27}$$

$$\psi = \frac{1}{2}\arg\big(\frac{1}{2}[(a+d) + i(c-b)]\big) + \frac{1}{2}\arg\big(\frac{1}{2}[(a-d) + i(c+b)]\big) \tag{3.28}$$

$$\varphi = \frac{1}{2}\arg\big(\frac{1}{2}[(a+d) + i(c-b)]\big) - \frac{1}{2}\arg\big(\frac{1}{2}[(a-d) + i(c+b)]\big) \tag{3.29}$$

where A_{major} is the major axis of the ellipse, A_{minor} is the minor axis, ψ is the inclination of the maximum current with the horizontal axis and φ is the phase (figure 3.22).

The ellipticity is defined as the ratio of the minor and major axis,

$$E = \frac{A_{minor}}{A_{major}} \tag{3.30}$$

The ellipticity defines whether the velocity vector turns clockwise, anti-clockwise or turns over from ebb to flood velocities only (does not rotate). According to Souza and Simpson (1996) the ellipticity is zero for a degenerated ellipse, -1 for a circular ellipse rotating cyclonic and 1 for a circular ellipse rotating anti-cyclonic.

Chapter 4

Results

4.1 Introduction

The aim is to investigate the influence of the Rhine river 80 km downstream from the river mouth (Hoek van Holland). The focus is concentrated on the onset and breakdown of stratification, the presence of cross-shore tidal currents and the dominant cross- and alongshore processes regarding stratification. An unique in-situ dataset, obtained by PoR and NIOZ at the 13th of October 2011, is used, which provides information in four dimensions. The background of this dataset can be found in Chapter 3. The daily conditions are of importance for the behaviour of the ROFI. Table 4.1 gives an overview of the wind, wave and tidal conditions during the measurement campaign, which are described in detail in subsection 3.2.5. The campaign took place just before spring tide. First the measured velocities are presented in section 4.2. The along- and cross-shore velocities are linked to the onset and breakdown of stratification. With use of the velocities the salinity distribution is observed in section 4.3. Section 4.4 shows the influence of the temperature on the state of the water column. The contribution of the cross- and alongshore processes is investigated with use of the Potential Energy Anomaly. The results of this analysis is presented in section 4.5. In the end when more insight is gained into the processes causing stratification and mixing analysis of the distribution of SPM is of interest. Section 4.6 gives the results of the SPM distribution.

Transect	Measured by	Location	Tide	Wind force [m/s]	Wind dir.	Wave height [m]
Northern	PoR	Egmond aan Zee	1 before ST	3.5 - 4.5	Easterly	± 1.0
Southern	NIOZ	Wijk aan Zee	1 before ST	3.5 - 4.5	Easterly	± 1.0

Table 4.1: The conditions during the measurement campaign at the 13th of October 2011. It was one day before Spring Tide (ST).

4.2 Velocity distribution

4.2.1 Measured Velocities

Considering a non-frictional Kelvin wave, the tidal velocity is in phase with the tidal amplitude. At slack water the velocity changes direction. From high water slack till low water slack the water flows southwards. The velocity is directed northwards from low water slack till high water slack. Figure 4.1 shows the alongshore velocity in three-dimensions, namely time, depth and distance from the shore. The depth mean alongshore velocity is presented in the first panel of the figures 4.2 and 4.3, even as the alongshore velocity (fourth panel). These figures show distinct ebb and flood velocities, alternating between heading northwards and heading southwards.

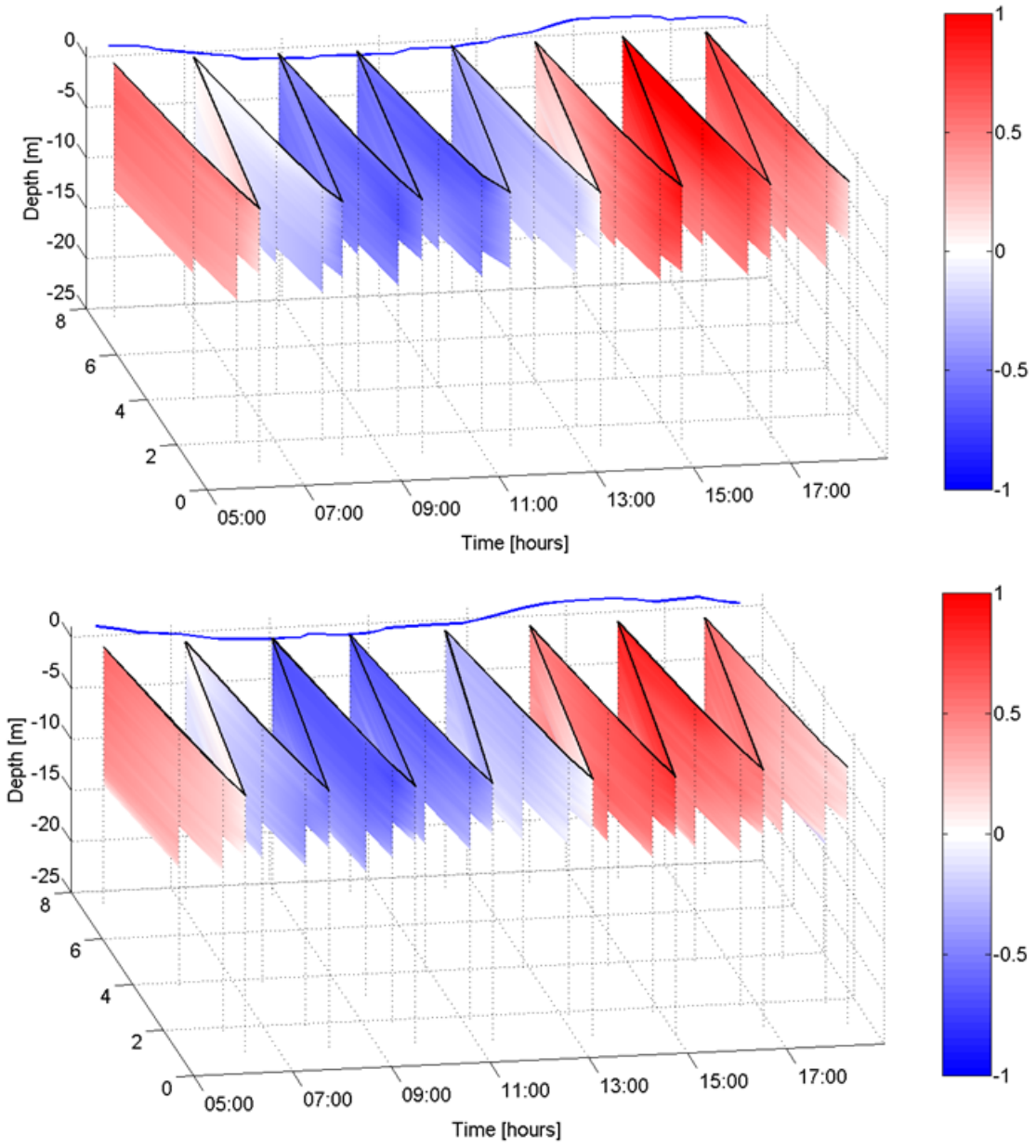

Figure 4.1: The alongshore velocity profile during the measurements in three-dimensions is shown. The upper panel shows the profile of the northern transect measured by PoR. The lower panel presents the southern transect measured by NIOZ. The velocity scale ranges from -1.0 till 1.0 m/s. The vertical axis represents the depth and the horizontal axis the time and the distance to the shore.

The velocity leads the tidal elevation (figure 4.2 and 4.3 first panel) by three hours during low water and one hour by high water. This can be concluded when the depth mean alongshore velocity is compared with the tidal elevation data for the 13th of October 2011. Around spring tide a leading tidal velocity is expected (e.g. De Boer et al. (2006), Van der Hout et al. (subm.)). The time between the two slack waters is about six and a half hours for the Northern transect and slightly longer for the Southern. For a symmetrical tide it is about six hours. Therefore, the alongshore velocity is considered here symmetrical. The tidal amplitude deforms moving towards the North. Viz. the period between high and low water becomes longer, and the period between low and high water shorter. This is the result of the experience of bed friction in the shallow coastal zone, causing a larger phase lag between the tidal amplitude and velocity. At the Northern transect the velocity switches between flood and ebb velocities about twenty minutes after the Southern

transect. For the reversal from ebb to flood this delay is not observed (it is not observed in the measured velocities, but it is in the fitted M2 signal). The delay is also visible for the maximum ebb and flood velocities.

Cross-shore velocities are observed (figure 4.4 and fifth panel of figures 4.2 and 4.3). These velocities are smaller than 50 % of the alongshore velocity. Opposite bottom and surface currents are observed, but not clearly recognizable during the entire campaign. Especially during track 5 and 6, at both transects, offshore surface currents and onshore bottom currents are observed. Following the tidal straining theory for the Rhine ROFI (Simpson and Souza, 1995), at high water slack the cross-shore surface velocity is directed onshore and at the bottom offshore. During low water slack the opposite is happening, the surface currents are directed offshore and the bottom currents onshore. This is the case during neap tide. During spring, the case for these measurements, hardly any cross-shore velocities are expected. The measured velocities show small cross-shore velocities. During low water slack offshore surface currents and onshore bottom currents are observed. At high water slack the directions are not in line with the above theory.

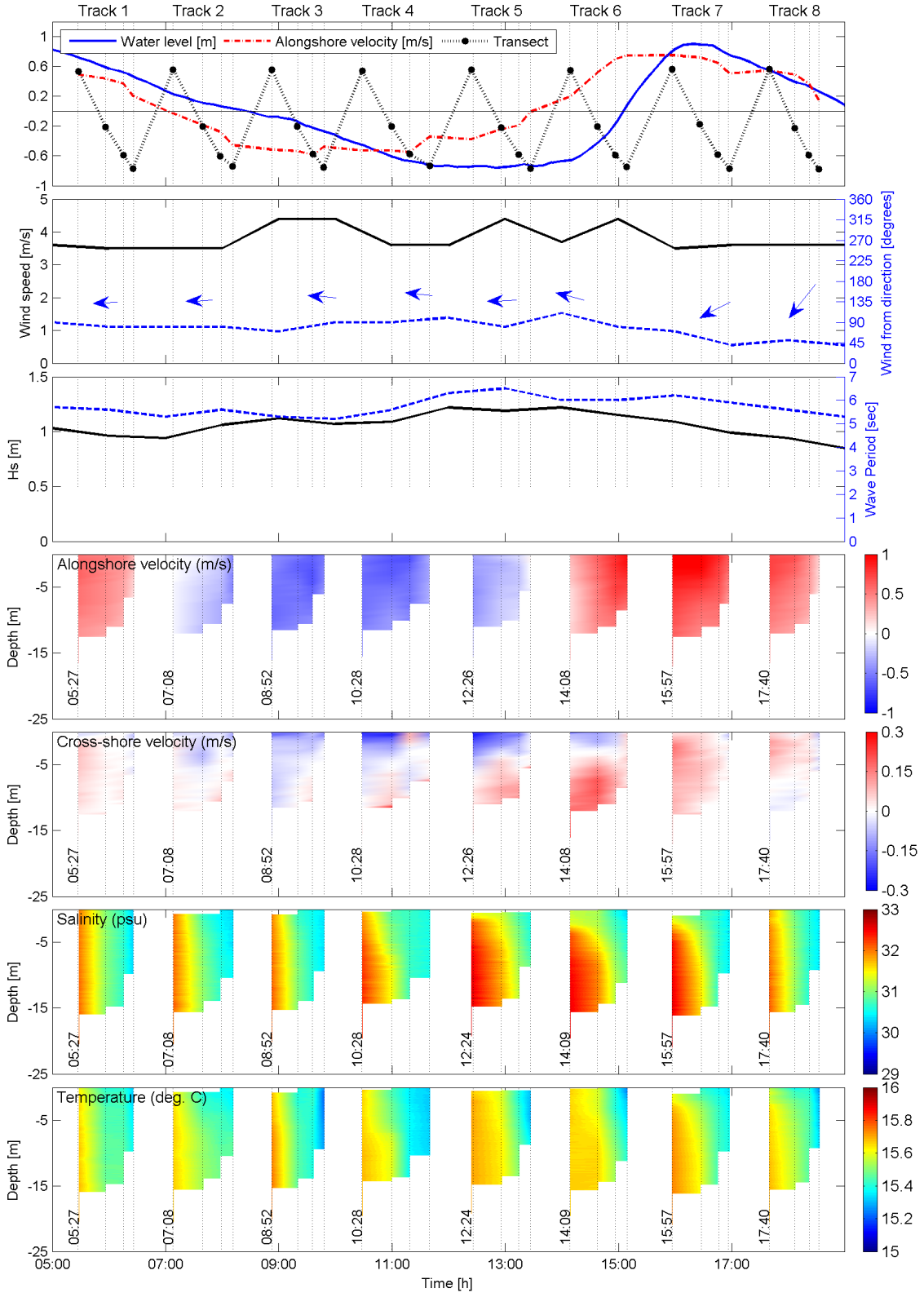

Figure 4.2: Data from the Northern transect on the 13th of October 2011. The dotted lines represent the measurement stations during the campaign. The panels show from top to bottom the following information: (1)the tidal height and the sailed transect in time. The blue line is the tide near IJmuiden Buitenhaven in m. The red dotted line is the measured depth mean alongshore velocity in m/s, where positive is northward. (2)Wind speed and direction. (3) Significant wave height, Hs. (4) Alongshore velocity in m/s, where positive is northward. (5) Cross-shore velocity in m/s, where positive is eastward. (6) Salinity in psu and (7) temperature in degree C.

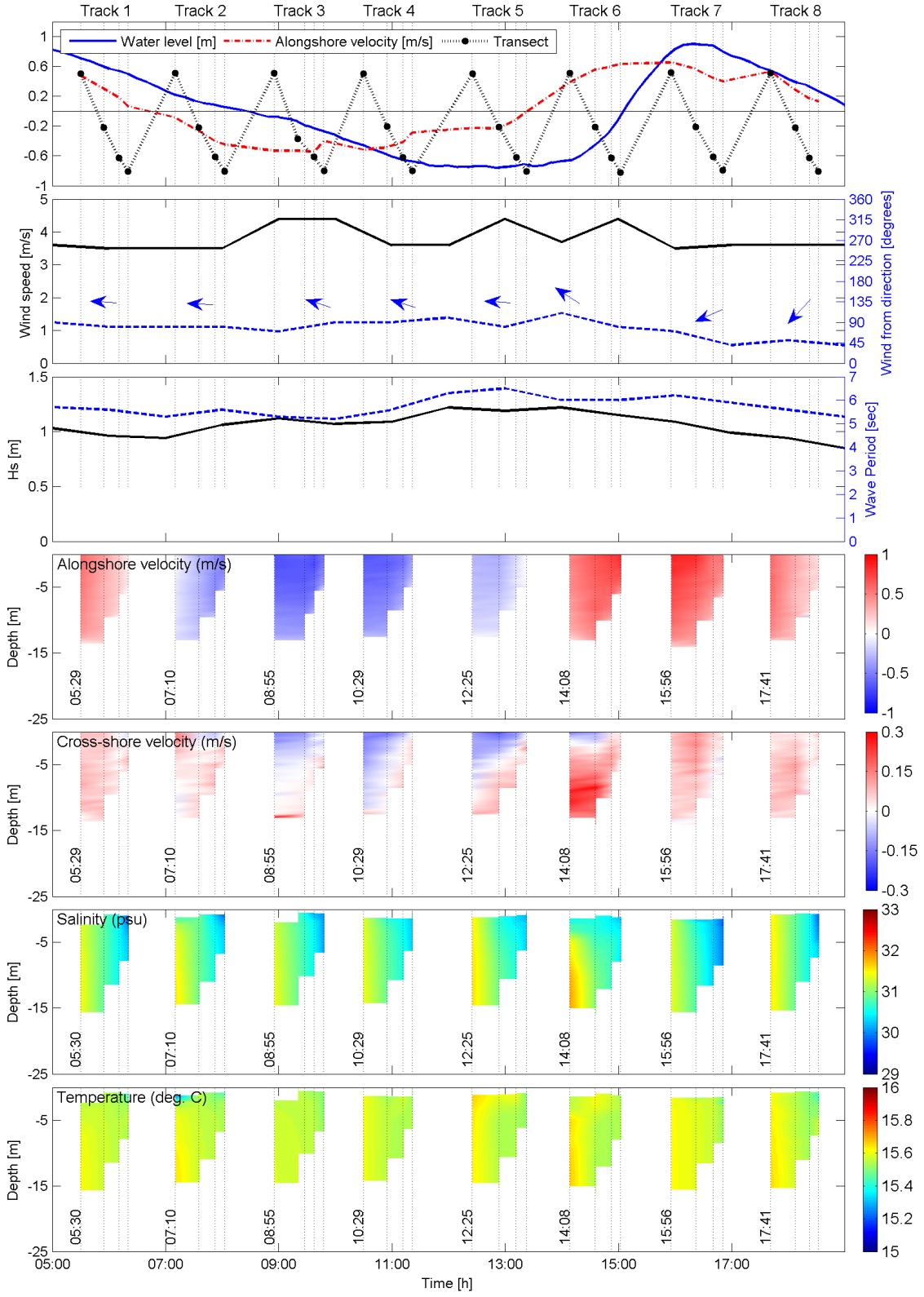

Figure 4.3: Data from the Southern transect on the 13th of October 2011. The dotted lines represent the measurement stations during the campaign. The panels show from top to bottom the following information: (1)the tidal height and the sailed transect in time. The blue line is the tide near IJmuiden Buitenhaven in m. The red dotted line is the measured depth mean alongshore velocity in m/s, where positive is northward. (2)Wind speed and direction. (3) Significant wave height, Hs. (4) Alongshore velocity in m/s, where positive is northward. (5) Cross-shore velocity in m/s, where positive is eastward. (6) Salinity in psu and (7) temperature in degree C.

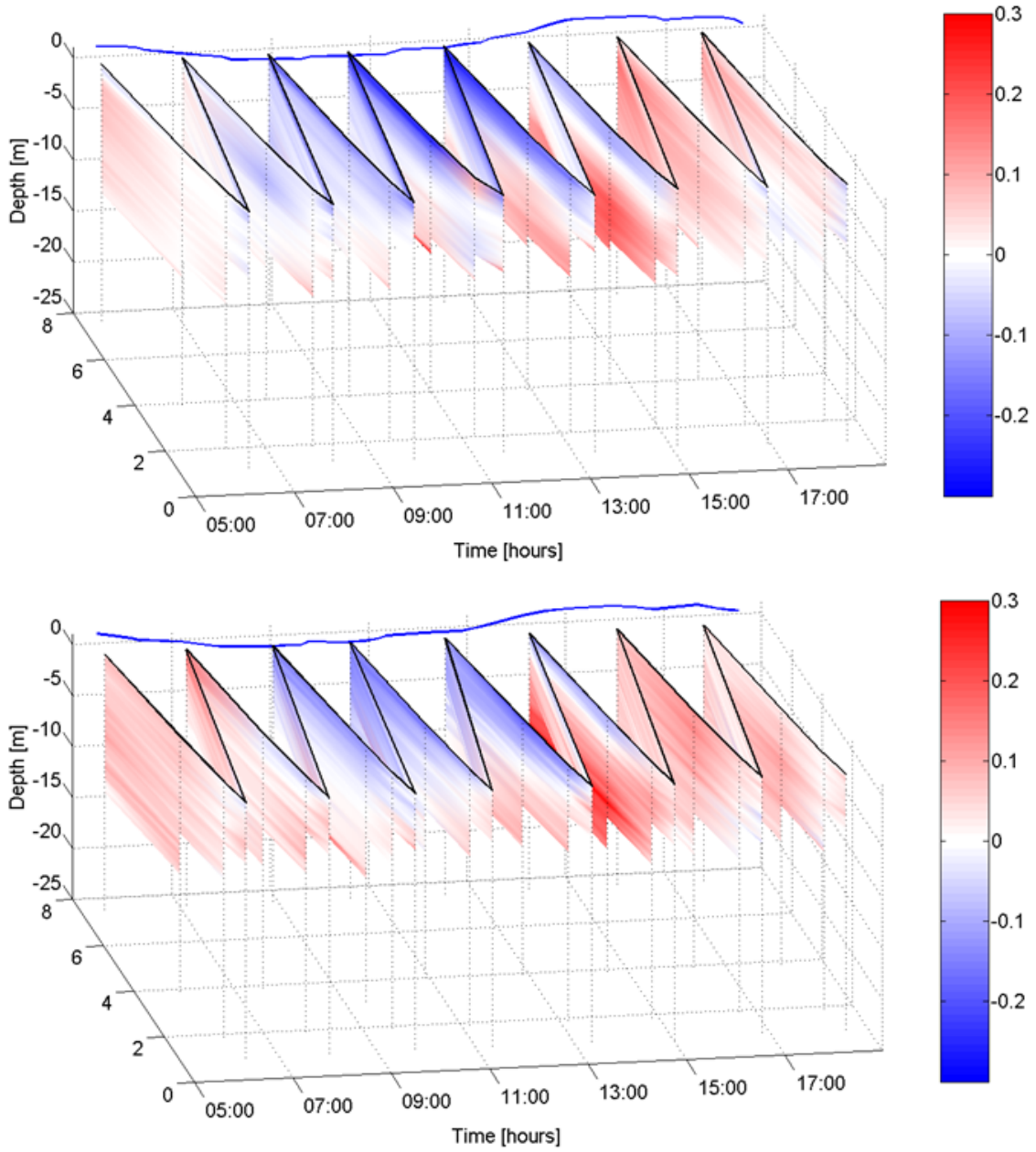

Figure 4.4: The cross-shore velocity profile during the measurements in three-dimensions is shown. The upper panel shows the profile of the northern transect measured by PoR. The lower panel presents the southern transect measured by NIOZ. The velocity scale ranges from -0.3 till 0.3 m/s. The vertical axis represents the depth and the horizontal axis the time and the distance to the shore.

Figure 4.5 shows that the velocity vector turns at the Northern and Southern transect. The turning is in line with the mentioned tidal straining theory. The surface velocity vector turns anti-cyclonic and the bottom velocity vector cyclonic. At high water slack the turning of the velocities is not very distinct, as during low water slack. The velocity vector seems to turn over from flood directly to ebb. For a better understanding the velocity signal can be separated into a tidal component and a residual term (subsection 4.2.2).

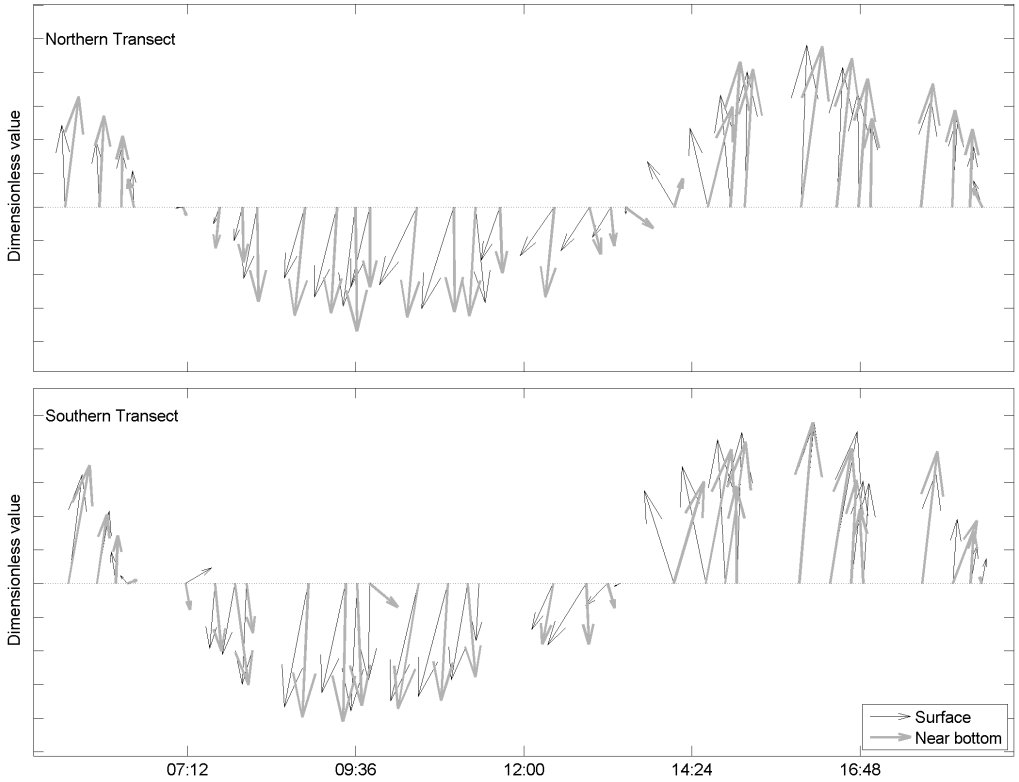

Figure 4.5: Direction of velocities at Northern transect (upper panel) and Southern transect. Black is velocity at bottom, grey in middle and light grey near surface. Positive is northwards, negative is southwards.

4.2.2 Tidal Current

The measured velocity signal contains for example the tidal current, a time averaged velocity, influence of the wind stress and velocity residuals. To investigate the velocity signal, the sign is separated into a tidal component and a residual term. The tidal current for the M_2 component is filtered out using tidal analysis, representing the semi-diurnal tidal component. For such a short period no distinction can be made between M_2 and S_2, as explained in section 3.4. At each depth the fitted M_2 tide has been compared with the measured velocity (figure 4.6 and 4.7). Overall, the results show that the fitted M_2 tide is in agreement with the measurements and can be used to investigate the tidal currents. Figures 4.8 and 4.9 show the separated velocity components.

Figures 4.6 and 4.7 show a distinct phase difference increasing over depth for the cross-shore M_2 velocities. This means that the tidal velocity at the bottom leads the surface velocity. This is inline with the theory that the water pressure at the bottom is higher than at the surface, resulting in a higher force which pushes the water away.

4.2.3 Ellipse properties

Figures 4.10 and 4.11 show the ellipse properties of the M2 tide for the Northern and the Southern transect. These properties give insight into the vertical structure of the tidal current and shows if the tidal velocity vector turns as an ellipse. The semi major axis showed a decrease in speed over depth with magnitudes of 0.7 - 0.8 m/s at the surface. The Northern transect has a smaller difference between surface and bottom velocities, meaning that higher alongshore bottom velocities are found for the Northern transect. The semi minor-axis shows very small values, around -0.05 m/s at the surface and 0.05 m/s near the bottom. The small values are expected, because of spring

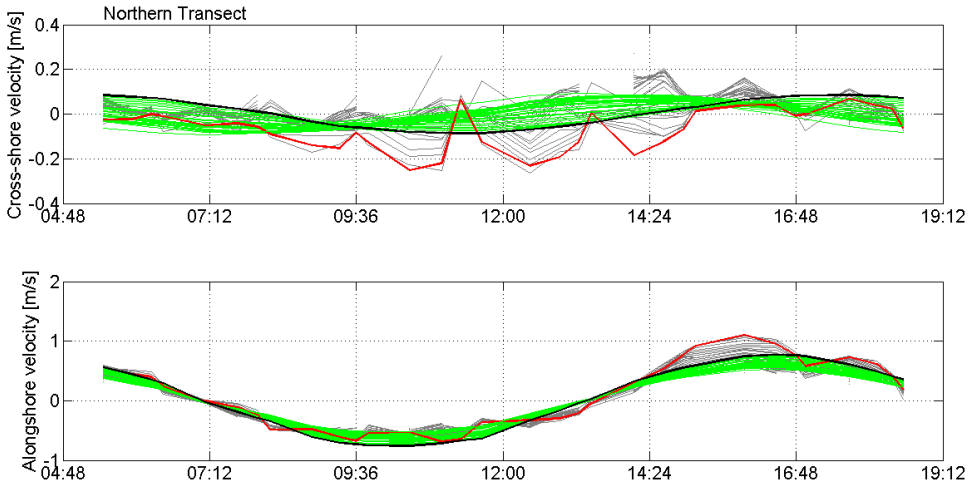

Figure 4.6: Northern transect. The upper panel shows the cross-shore velocities. The lower panel the alongshore velocities. The grey lines are the measured velocities over depth. The red line indicates the measured surface velocity. The green lines represent the fitted M_2 velocities, where the black line indicates the M_2 velocity at the surface.

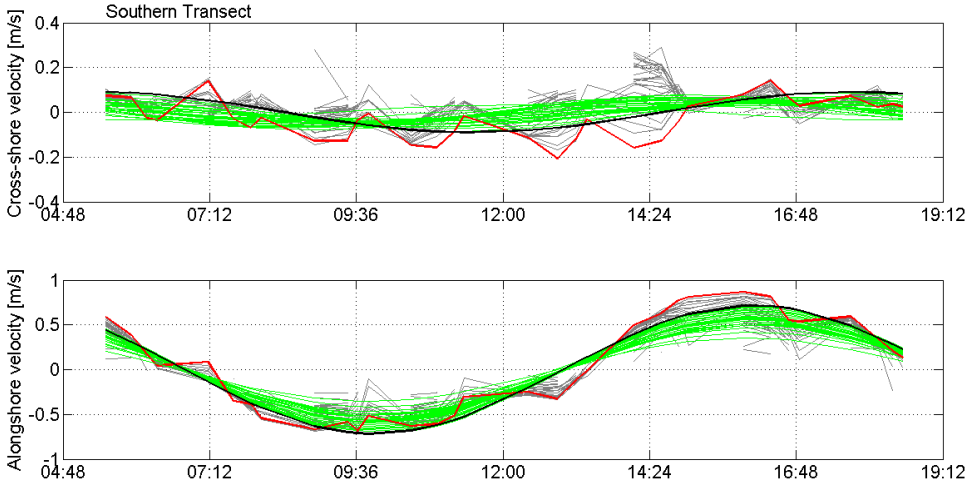

Figure 4.7: Southern transect. The upper panel shows the cross-shore velocities. The lower panel the alongshore velocities. The grey lines are the measured velocities over depth. The red line indicates the measured surface velocity. The green lines represent the fitted M_2 velocities, where the black line indicates the M_2 velocity at the surface.

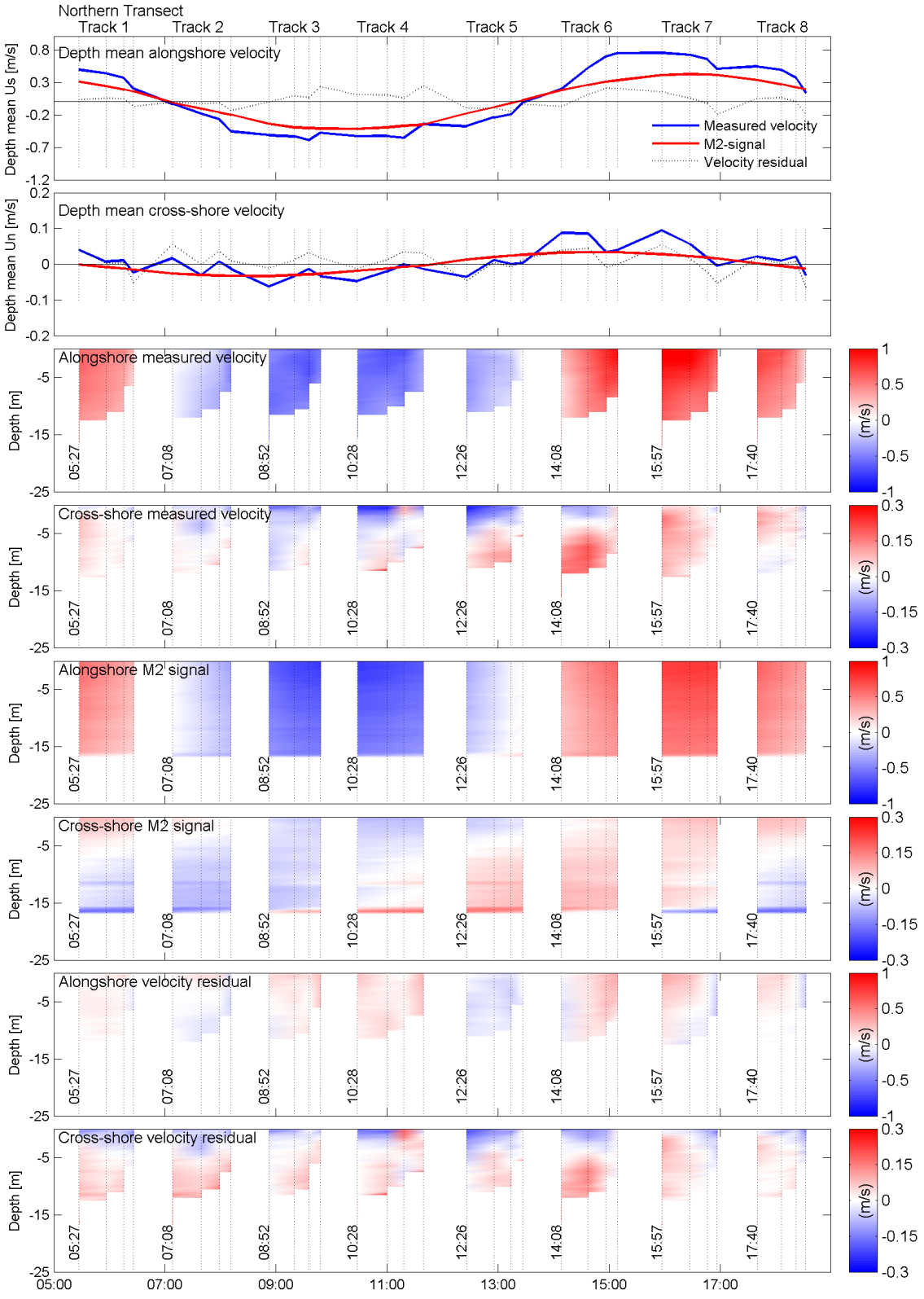

Figure 4.8: Velocity signal on the 13th of October 2011 at the Northern transect. The dotted lines represent the measurement stations during the campaign. Positive velocities are north- and eastwards. The panels show from top to bottom the following information: (1)The depth mean alongshore velocity in m/s, where the measured velocity in blue, the M_2 velocity in red and the difference between the the measured and the M_2 is the black dotted line.(2) The depth mean cross-shore velocities in m/s. The lines have the same meaning as in panel 1. (3) The measured alongshore velocity in m/s(4) The measured cross-shore velocity in m/s (5) Alongshore M_2 velocity in m/s (6) Cross-shore M_2 velocity in m/s (7) The velocity residual in alongshore direction (m/s) (8) The velocity residual in cross-shore direction

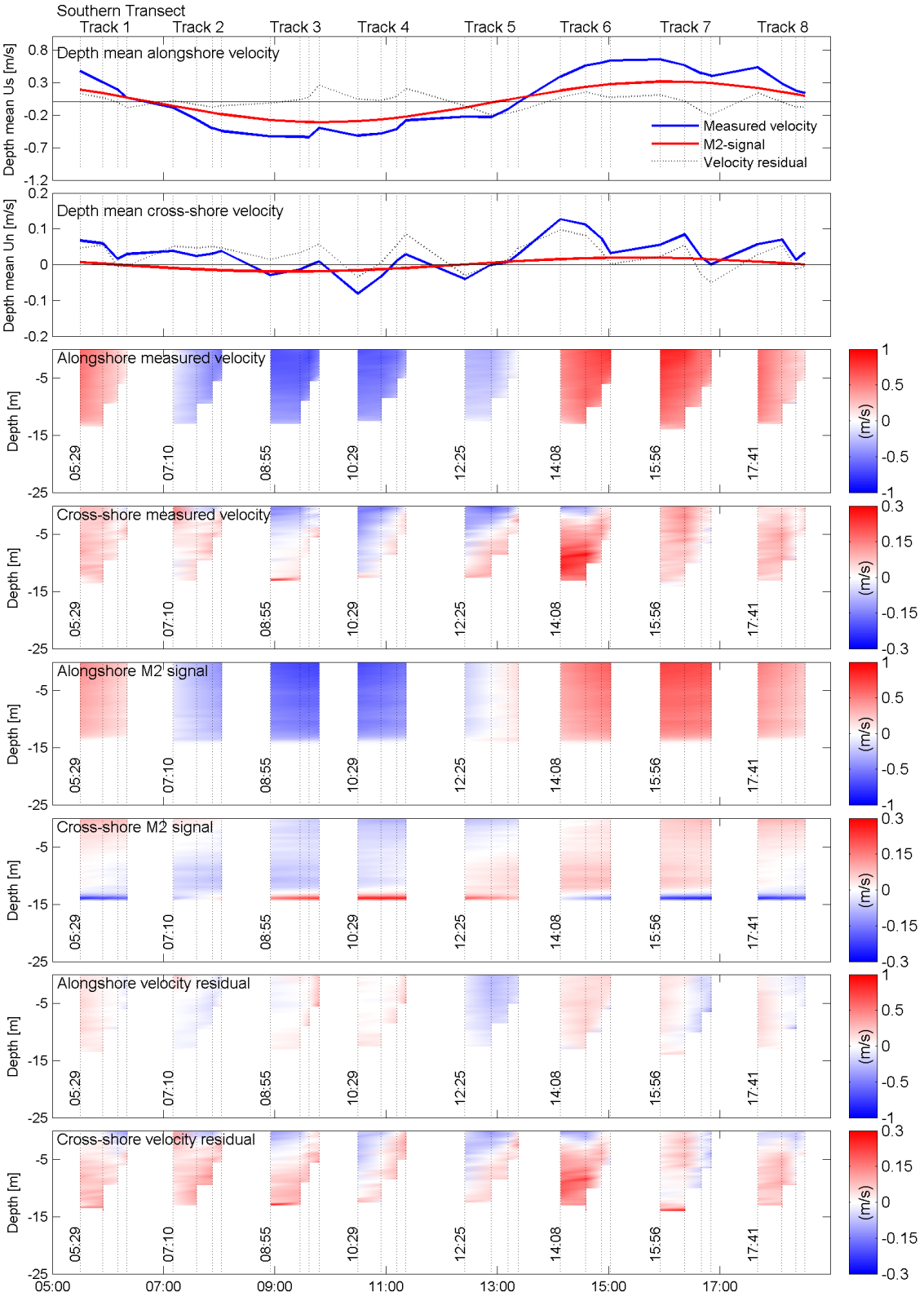

Figure 4.9: Velocity signal on the 13th of October 2011 at the Southern transect. The dotted lines represent the measurement stations during the campaign. Positive velocities are north- and eastwards. The panels show from top to bottom the following information: (1)The depth mean alongshore velocity in m/s, where the measured velocity in blue, the M_2 velocity in red and the difference between the the measured and the M_2 is the black dotted line.(2) The depth mean cross-shore velocities in m/s. The lines have the same meaning as in panel 1. (3) The measured alongshore velocity in m/s(4) The measured cross-shore velocity in m/s (5) Alongshore M_2 velocity in m/s (6) Cross-shore M_2 velocity in m/s (7) The velocity residual in alongshore direction (m/s) (8) The velocity residual in cross-shore direction

tide. Still, the minor axis is 10 % of the major axis. The positive and negative values of the minor axis mean that the surface and bottom layer are directed in opposite direction at the same time. The minor axis and the ellipticity show that the upper layer of the water column has a thickness of 4 meters for the Northern transect and 5 meters for the Southern transect. The depths differs per transect. The upper layer is about 38 % of the water column for the Southern transect. At the Northern transect it is about 25 %.

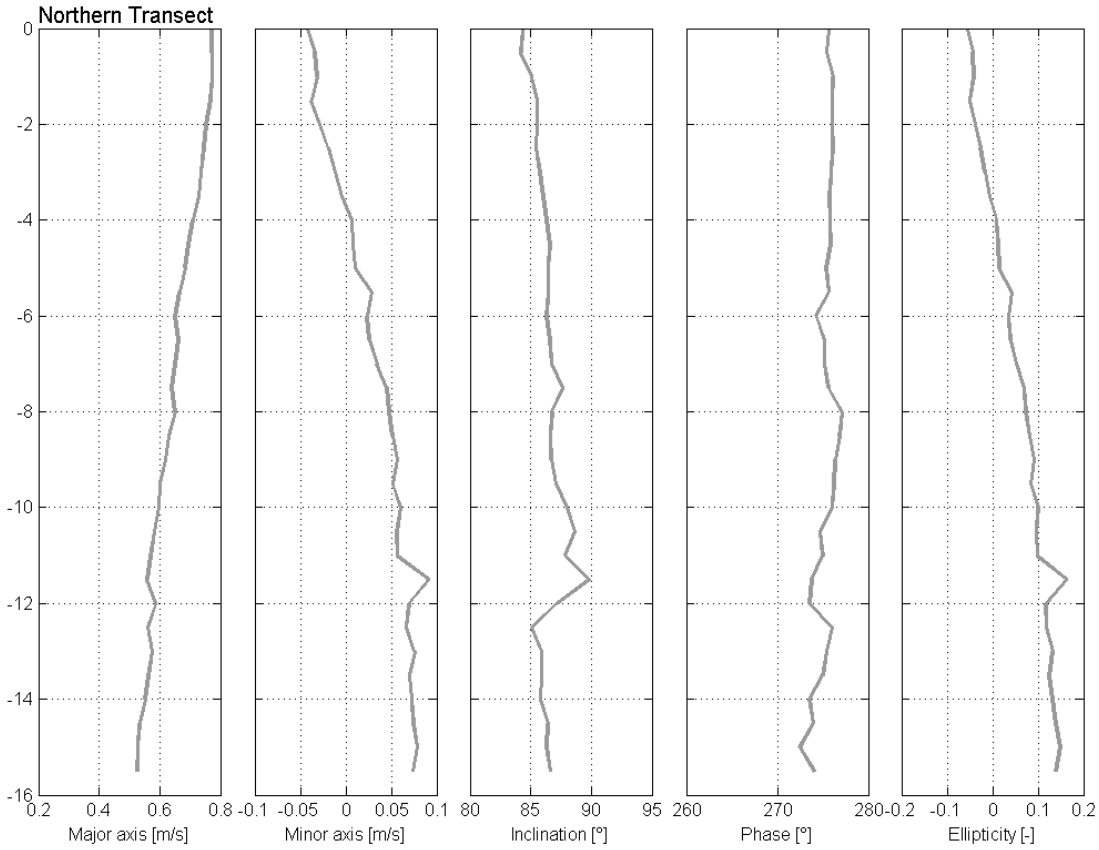

Figure 4.10: The ellipse properties for the Northern transect. From left to right: (1) the major axis in m/s, (2) the minor axis in m/s, (3) the inclination in degrees, (4) the phase in degrees and (5) the ellipticity (dimensionless)

Both transects show an ellipticity larger than zero (figures 4.10 and 4.11, right panel). This means that ellipses are formed. Mostly during spring tide the ellipticity is almost zero, with a small velocity vector turning cyclonic near the bed and a degenerated ellipse shape at the surface (figure 3.22) (De Boer et al., 2006). The Southern transect shows an ellipticity of -0.1 near the bottom to 0.1 near the surface, the same values near bed and surface. The Northern transect shows a larger ellipticity near the bottom than at the surface, the bottom ellipticity is about 0.15 and -0.05 at the surface. These values can be displayed in the form of the tidal ellipses (figure 4.12). The surface velocity vector turns anti-cyclonic (blue) and the bottom layer turns cyclonic (red). This observation is in line with figure 4.5 and with the tidal straining theory. Ellipticity is linked to stratification. When ellipses are present it means that the water column is stratified, resulting in cross-shore tidal velocities, which induce tidal straining.

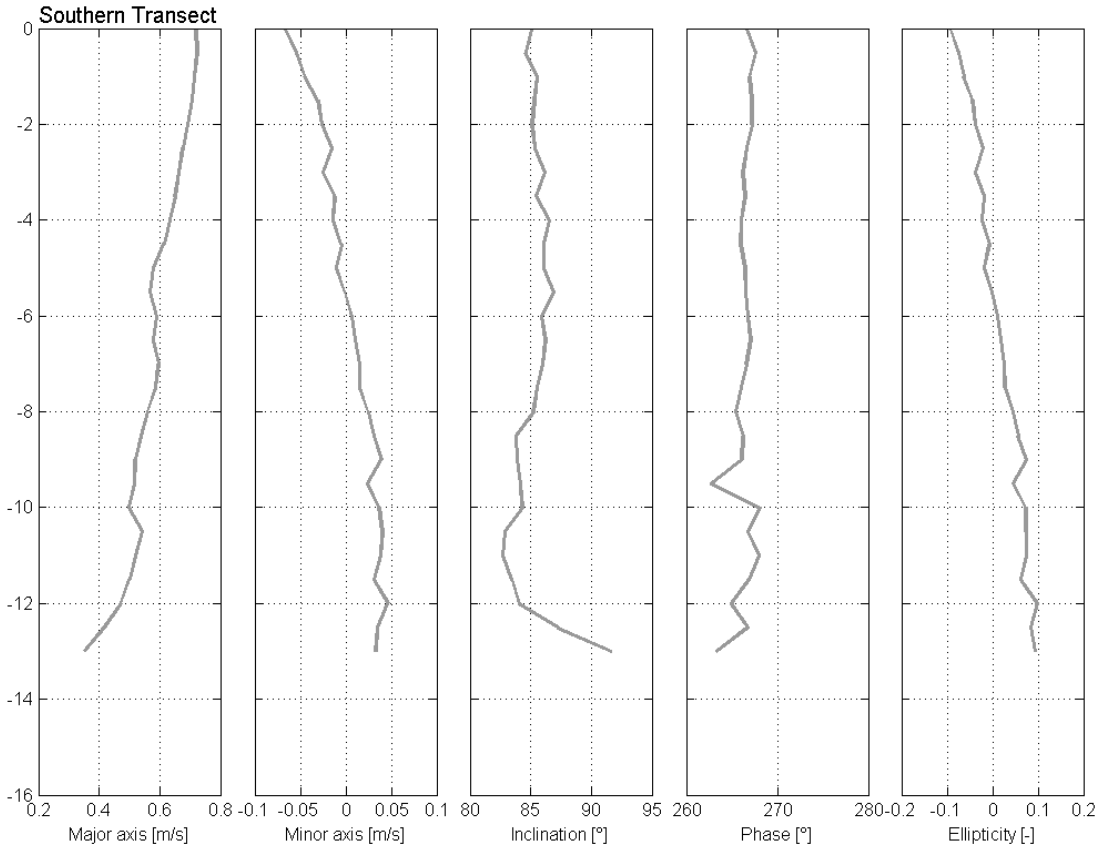

Figure 4.11: The ellipse properties for the Southern transect. From left to right: (1) the major axis in m/s, (2) the minor axis in m/s, (3) the inclination in degrees, (4) the phase in degrees and (5) the ellipticity (dimensionless)

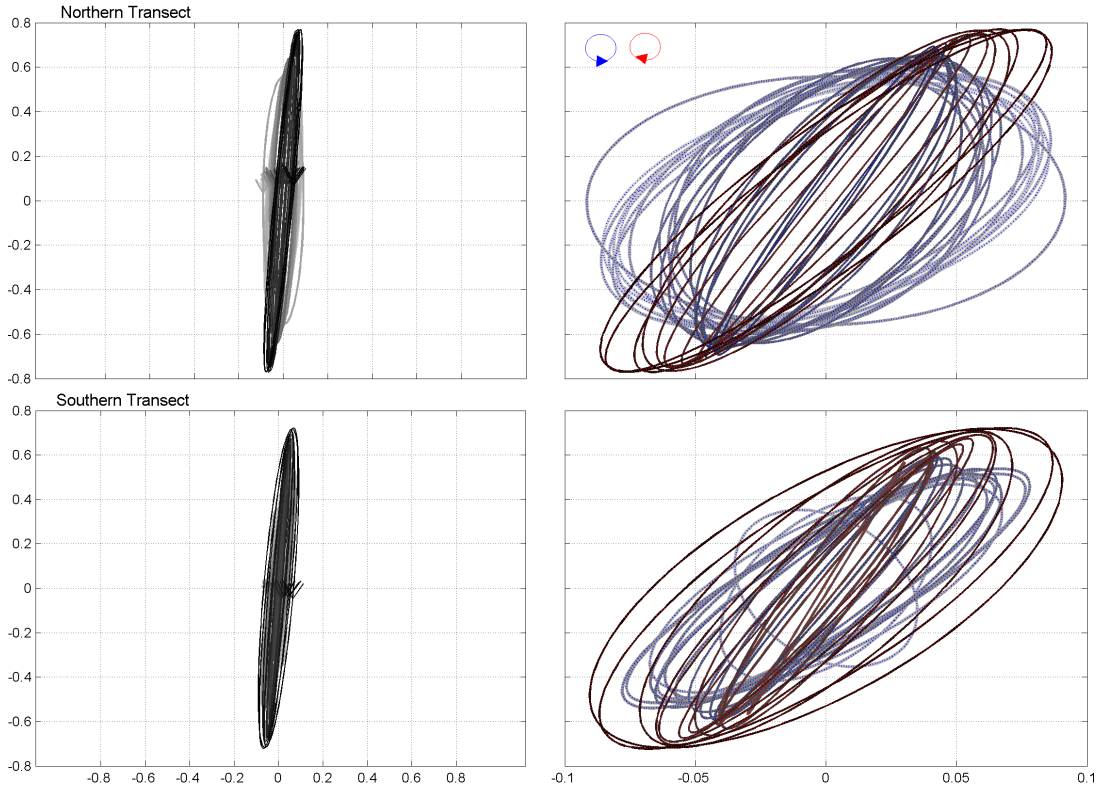

Figure 4.12: The upper 2 panels show the ellipse for the Northern transect. On the left the ellipse is displayed on equal axes. On the left the axes are not equal. The thin black line represents the surface and the thick light grey line the bottom layer. In the figure on the right red means that the velocity vector turns anti-cyclonic and blue cyclonic.

4.2.4 Velocity residuals

Figures 4.6 and 4.7 show a positive alongshore velocity residual for both transects. Hence, other currents are present in alongshore direction. This residual can be ascribed to for example the wind stress, other tidal constituents and the residual velocity (defined as the difference between flood and ebb velocities). The wind was directed offshore. An offshore wind results in a frictional component in offshore direction and ,when the water column is (weak) stratified, a force towards the north regarding Ekman Dynamics. Therefore, a part of the northward velocity residual can be ascribed to the pushed water northwards by the wind.

The net along- and cross-shore residual velocity is determined with use of the data shown in figures 4.8 and 4.9. For one tidal period (here 12 hours and 25 minutes) the residual values are accumulated and divided by the total number of values. For the alongshore velocity the mean residual values (presented in the upper panel of figures 4.8 and 4.9) are used, resulting in a mean alongshore residual velocity of 0.030 m/s for the Northern transect and 0.012 m/s for the Southern transect. The residual velocity is northwards directed at both transects. For the cross-shore velocity the residual bottom and surface currents are determined, resulting in a residual offshore directed velocity at the surface and onshore at the bottom, for both the Northern and Southern transect. The values are presented in table 4.2. The residual velocities are interesting for the transport of SPM for example.

Residual velocity	Northern Transect [m/s]	Southern Transect [m/s]
Mean alongshore	0.0301	0.012
Cross-shore surface	-0.075	-0.037
Cross-shore bottom	0.061	0.055

Table 4.2: The residual velocities, in along- and cross-shore direction, calculated from the measured velocities and the fitted M_2 tide. Positive velocity is northwards or onshore in m/s.

4.3 Salinity Distribution

Figure 4.13 shows the three-dimensional salinity profile for the Southern and Northern transect along the Dutch coast. The salinity distribution is shown over time and depth. Figures 4.2,4.3,4.14 and 4.15 show the salinity, temperature and density profile in time for both transects, which give a clear picture of what actually happens during the measurements. The interest lies at the existence and behaviour of the freshwater plume and the onset and breakdown of stratification. This is investigated with the use of the salinity distribution. The measurements are implemented at October, therefore salinity is dominating the density profile and stratification, as explained by section 4.4.

4.3.1 Freshwater plume

The freshwater plume can be distinguished with use of salinity. Fresh river water from the Rotterdam New Waterway is in the order of 25 PSU, whereas seawater is defined around 35 PSU (IOC et al., 2010). As explained in Chapter 2, the Rhine river has a pulsed discharge, lenses of fresh water are released into the North Sea (influenced by the tide) and transported northwards. These freshwater lenses are slowly mixed till they reach the study area. Therefore, more northwards from the river mouth (Hoek van Holland) higher salinity values are expected. Figure 4.13 shows a minimum salinity of 29.5 for the Southern transect and 30 PSU for the Northern transect, which indicates the influences of fresh riverine water (based on e.g. De Ruijter et al. (1997) and Giessen et al. (1990)). Maximum salinity is 32.7 PSU for the Northern transect and 31.8 PSU for the Southern transect. The fresher water is found close to the coast. This could be a result of the heavy west-southwestern wind the days before. The hypothesized location of the plume at the start of the measurements is presented in figure 3.13.

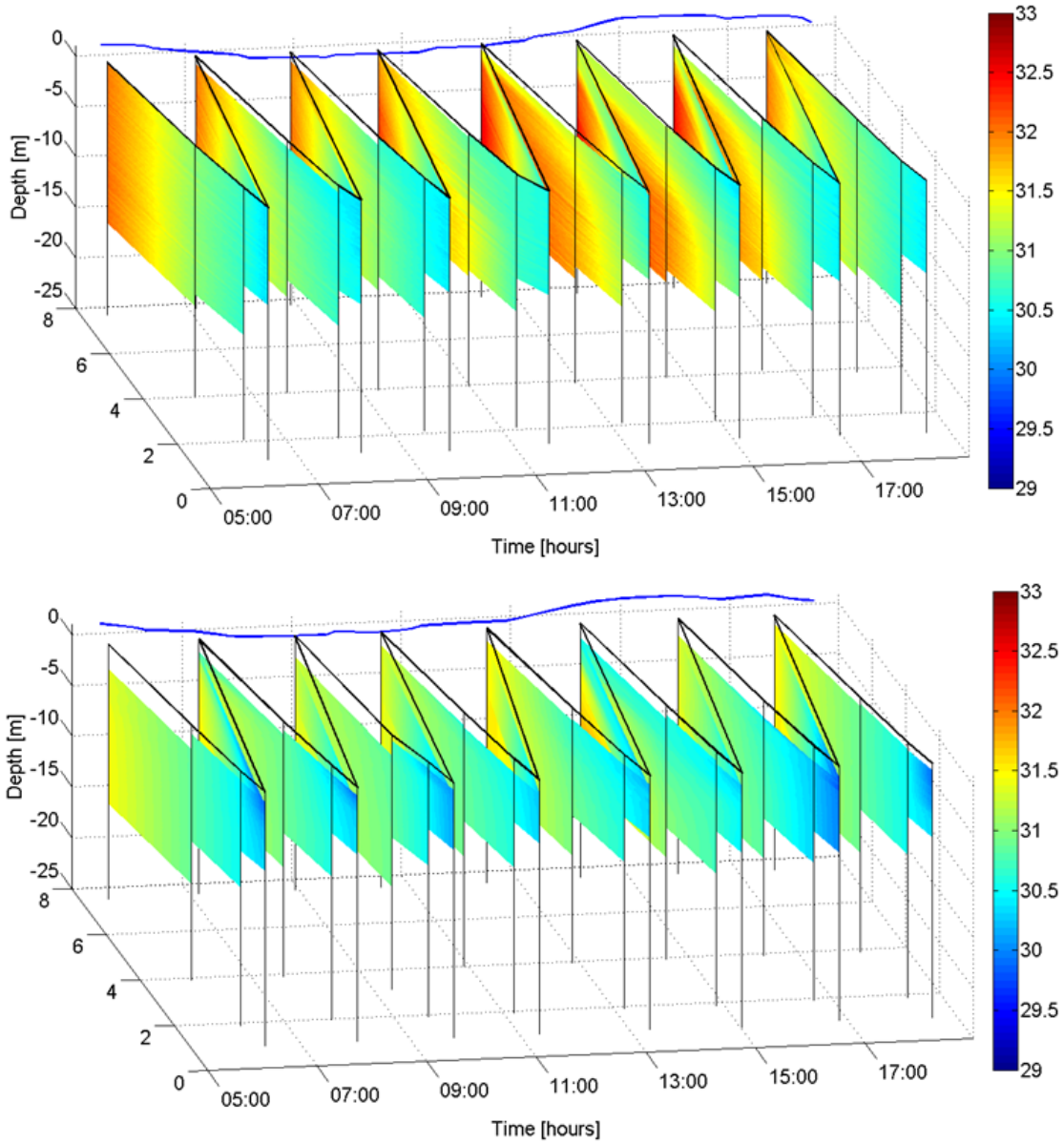

Figure 4.13: The salinity profile during the measurements in three-dimensions is shown. The upper panel shows the profile of the northern transect measured by PoR. The lower panel presents the southern transect measured by NIOZ. The salinity scale ranges from 29 till 33 PSU (practical salinity units). The vertical axis represents the depth and the horizontal axis the time and the distance to the shore.

4.3.2 Horizontal stratification

Figure 4.13, even as the figures 4.2 and 4.3, show differences in salinity between the different stations. Both transects show fresher water onshore and more saline water offshore, resulting in a cross-shore salinity gradient. The horizontal differences are small, in the order of 1.5 a 2 PSU between station 1 and 4. The cross-shore difference at the Northern transect is slightly higher (in the order of 0.5 PSU) than for the Southern, resulting in a cross-shore salinity gradient in the order of $2.5 \cdot 10^{-4}$ for the northern transect and $2.0 \cdot 10^{-4}$ for the southern transect.

Figure 4.13 indicates differences in salinity between the Northern and Southern transect. The four northern stations show more saline water than the stations at the Southern transect. This means that an alongshore horizontal salinity gradient is present. The maximum salinity observed is about 31.8 PSU at the Southern transect. For the Northern transect this is around the 32.7

PSU. Horizontal salinity differences in alongshore direction are on average 0.5 PSU and sometimes around 1.0 PSU. The maximum alongshore differences are found at the station 8 km offshore. As a result an average alongshore salinity gradient in the order of $5.5{\cdot}10^{-5}$ PSU/m^{-1} is found 8 km offshore and about $2.5{\cdot}10^{-5}$ PSU/m^{-1} at 1 km offshore.

The alongshore density gradient between the Northern and Southern transect can be explained by the distance from the river mouth (Hoek van Holland). The plume water mixes while it travels downstream, the further away from the river mouth the salinity increases and the plume becomes narrower. Suijlen and Duin (2002) described the yearly mean horizontal salinity gradient in front of the Dutch coast (figure D.3), which shows that the salinity increases and the gradient decreases in northward direction. When the plume is narrower northwards denser water is observed more onshore. Furthermore, the North Sea Channel at IJmuiden, discharged around 120 m^3/s into the North Sea on the day and the day(s) before of the measurement campaign. The plume and the water from the North Sea Channel need to flow around the breakwaters at the Port of IJmuiden.

4.3.3 Onset and breakdown of vertical stratification

Figure 4.13 and the salinity figures (figures 4.2 and 4.3, panel 6) show the development of stratification. At the start of the measurements the water column is well-mixed, only horizontal stratification is observed. During the day fresher water is observed on top of more saline water, the water column is stratified over the vertical. The onset and breakdown of the vertical stratification is clearly shown with the relative salinity difference. The relative salinity difference is defined as (salinity$_{bottom}$ - salinity(z)) and is shown in figure 4.14 and figure 4.15 (panel 3).

Differences between the Northern and Southern transect are observed regarding the onset and breakdown of stratification. Both transects show a well-mixed water column at the start of the measurements. During slack water the Southern transect shows (very) weak stratification at station 1 (8 km offshore). During maximum ebb velocities the water column is well-mixed again. The Northern transect becomes stratified directly after maximum ebb velocities and reaches its maximum around maximum flood velocities. This happened during the sixth track. The Southern transect shows maximum stratification at track 6 as well. Both transects reach a maximum difference of 1.3 PSU over the vertical, which is observed at station 1 (most offshore). A vertical salinity difference of 1.3 or less PSU means weak stratification. The onset and breakdown of stratification, as well as the differences between the two transects are clearly shown by the Potential Energy Anomaly (φ) (Figure 4.17). The figures D.1 and D.2 in Appendix D show clearly the differences between the Northern and Southern transect.

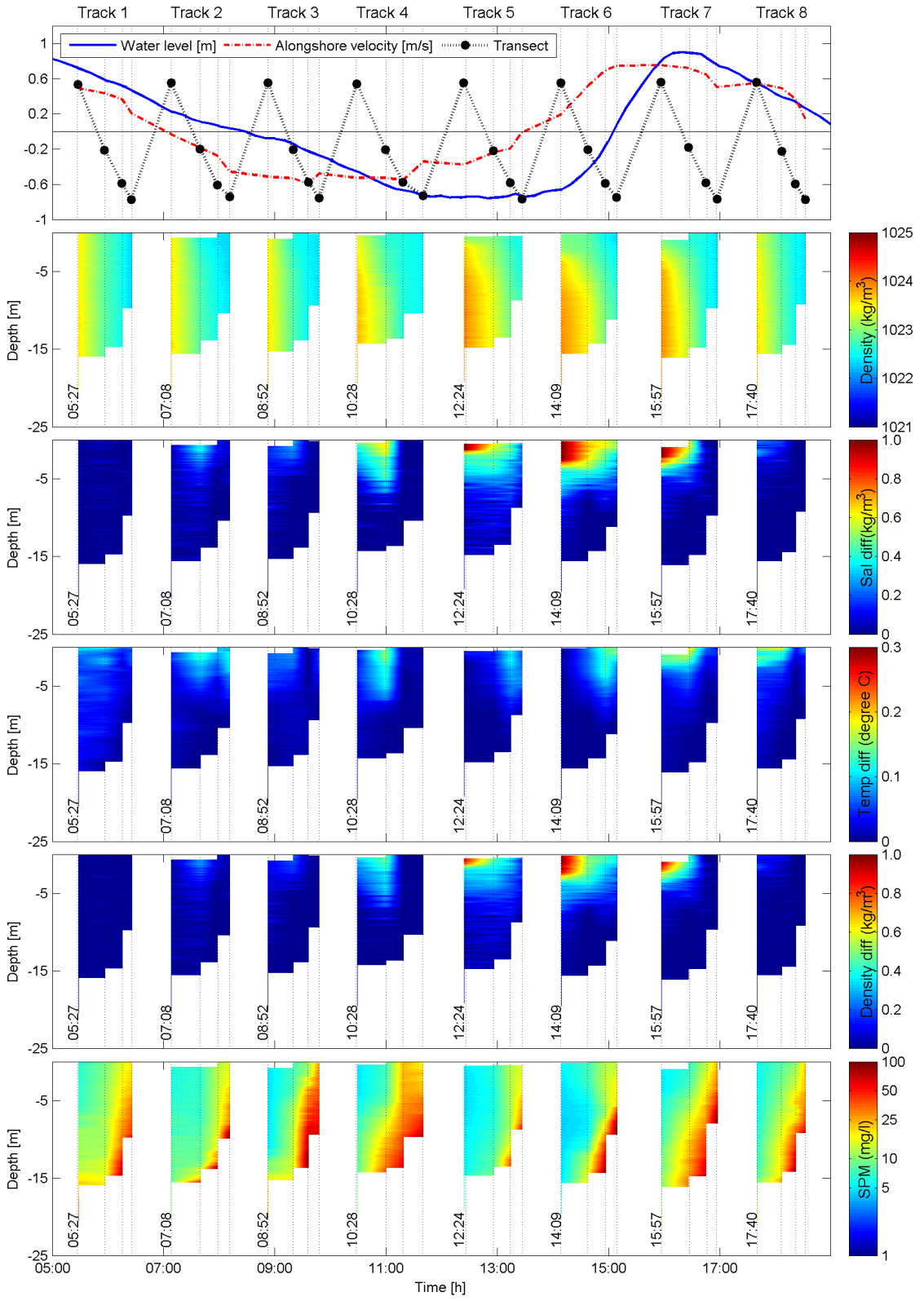

Figure 4.14: Data from the Northern transect on the 13th of October 2011. The dotted lines represent the measurement stations during the campaign. The panels show from top to bottom the following information: (1)the tidal height and the sailed transect in time. The blue line is the tide near IJmuiden Buitenhaven in m. The red dotted line is the measured depth mean alongshore velocity in m/s, where positive is northward. (2) Density in kg/m^3, (3) salinity difference (salinity$_{bottom}$-salinity(z)), (4) temperature difference, (5) density difference and (6) suspended particulate matter (SPM) in mg/l (7) the bottom and surface SPM concentrations per station, in mg/l.

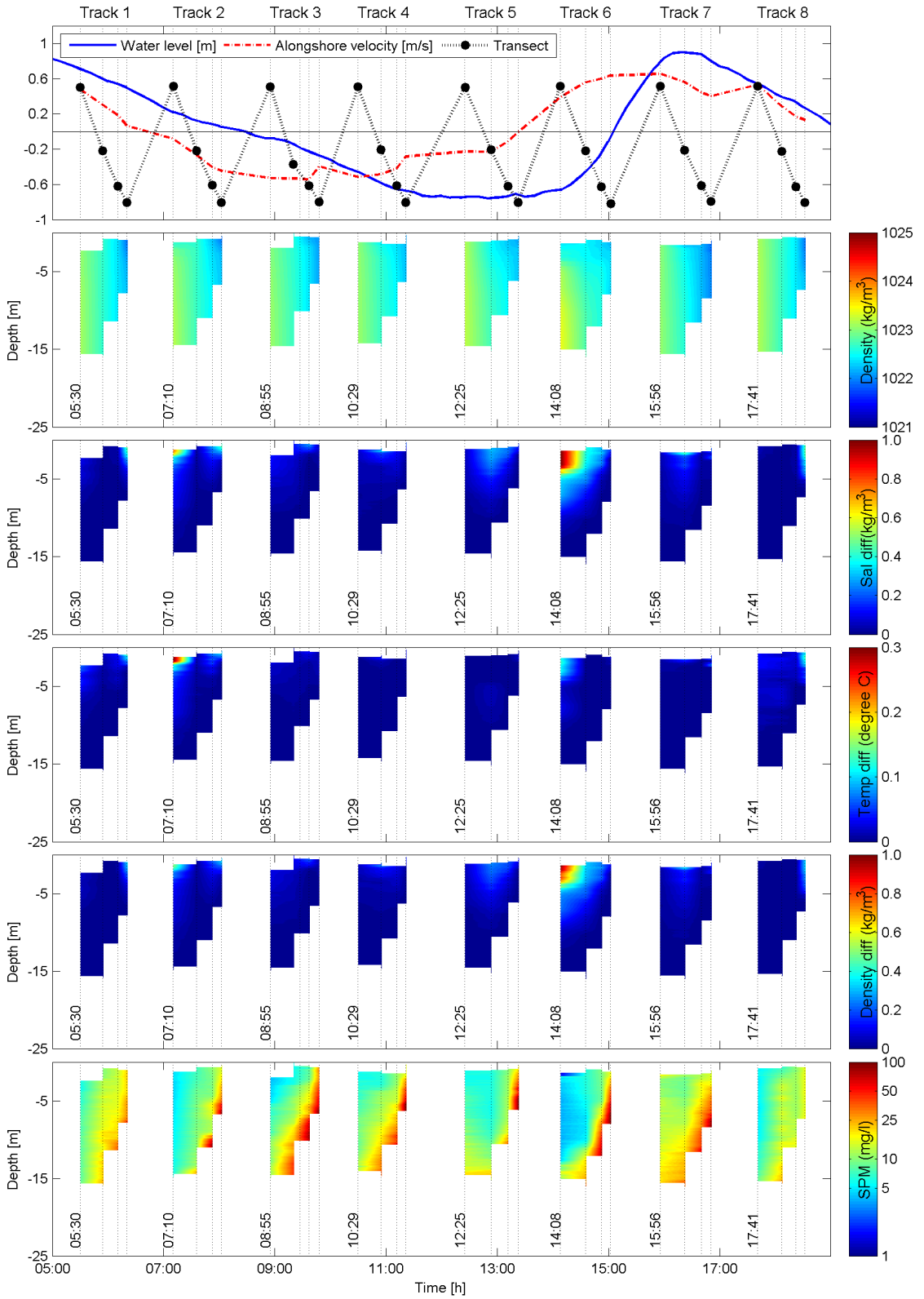

Figure 4.15: Data from the Northern transect on the 13th of October 2011. The dotted lines represent the measurement stations during the campaign. The panels show from top to bottom the following information: (1)the tidal height and the sailed transect in time. The blue line is the tide near IJmuiden Buitenhaven in m. The red dotted line is the measured depth mean alongshore velocity in m/s, where positive is northward. (2) Density in kg/m^3, (3) salinity difference (salinity$_{bottom}$-salinity(z)), (4) temperature difference, (5) density difference and (6) suspended particulate matter (SPM) in mg/l (7) the bottom and surface SPM concentrations per station, in mg/l.

4.4 Temperature

The temperature sensor of the CTD device measured the temperature of the water. The temperature distribution, in assessment with salinity, gives information about the density of the water, the location of the plume, the state of water column and solar heating. Figures 4.2, 4.3 and 4.16 show the temperature distribution over time and depth.

The temperature distribution (figure 4.16) shows warmer seawater offshore and colder water onshore. This distribution is expected during the month of October. Pietrzak et al. (2011) shows with SST images that the ROFI cools down around September. During the autumn and winter months the Rhine ROFI is colder than seawater. The onshore water temperature is slightly lower than offshore. Vertical stratification and mixing is observed in the temperature plots.

Differences in the temperature distribution between the northern and southern transect are observed. The differences are noticeable but small, because the temperature lies between 15 and 16 degrees C. The northern transect shows a horizontal temperature difference of 0.70 degree C. At the southern transect this is 0.25 degree C. The distributions show the same pattern as the salinity distribution. The denser water is higher in temperature and further offshore. The freshwater with a lower temperature is observed closer to the coast.

Section 2.2 describes that stratification can be amplified by solar radiation and by exchange of heat between water surface and the atmosphere. The magnitude of this contribution to stratification depends on the season. The air temperature on the 13th of October was 6 degrees C at 04:48, it increased to 14 degree C during the day. The maximum global radiation that day was 180 J/cm^3. A temperature of 14 degree C is lower than the temperature of the water and heating up of the surface water in October is not expected beforehand. Conversely, cooling down is more expected. The relative temperature (difference between bottom and surface temperature) is used to investigate the cooling down of the surface (figures 4.14 and 4.15, panel 4). Figure 4.16 does not show distinct cooling of the surface, it is hard to distinguish from the movement of the plume.

For the study area, the maximum relative temperature differences, horizontal and vertical, are less than 0.3 degree C. These relative differences are much smaller compared with the salinity contribution (panels 2,3 and 4, figures 4.14 and 4.15).The observation is confirmed by Giessen et al. (1990). For the time of the year, autumn, it is expected that haline stratification controls the plume. During summer the thermal differences can contribute up to 30 percentage of the vertical density gradient (De Kok et al., 2001). For this research, it is concluded that the water temperature has a limited effect on buoyancy, therefore the salinity distribution determines largely the density profile at both transects. However, for the potential energy anomaly analysis both, salinity and temperature, values are taken into account.

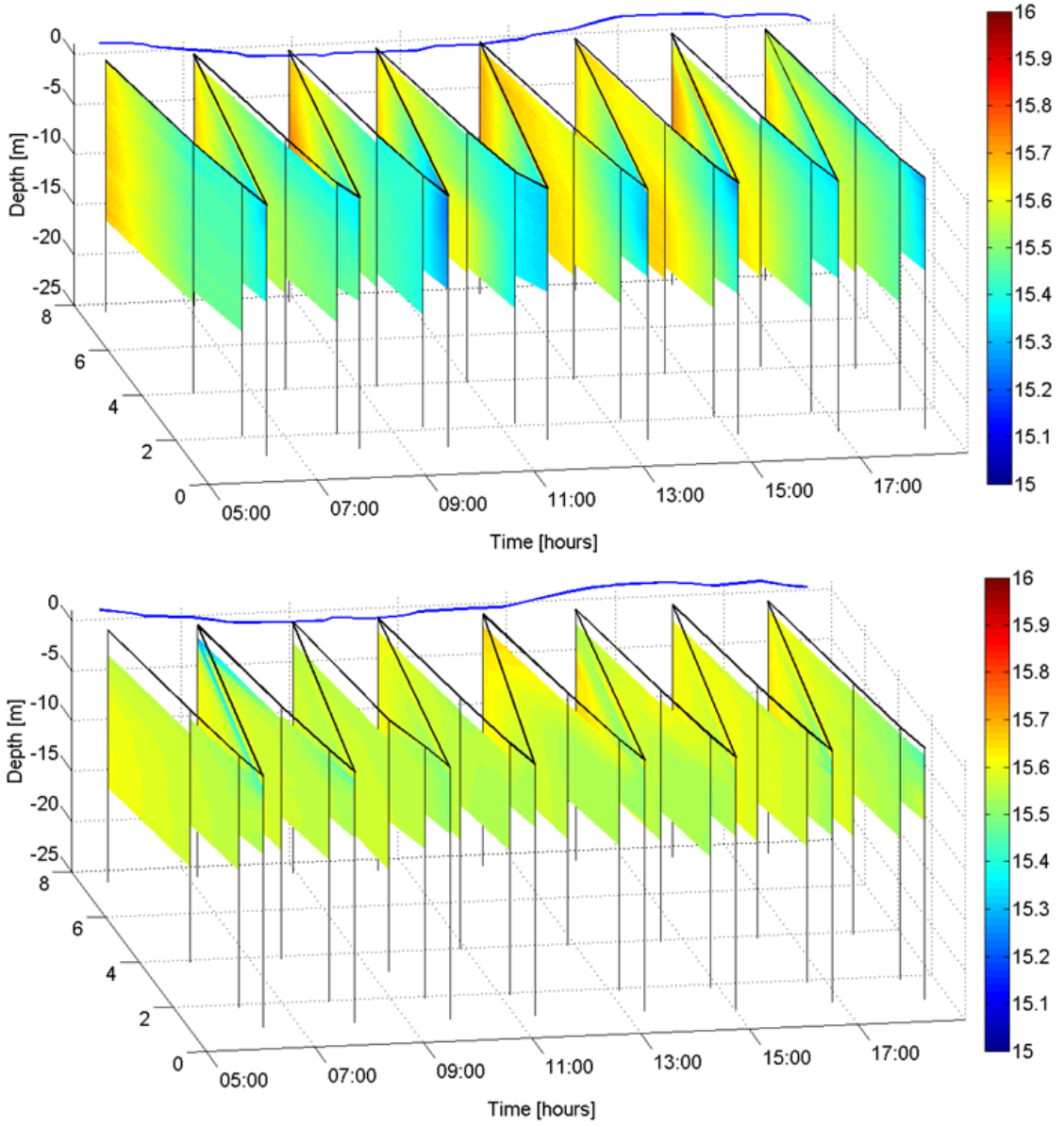

Figure 4.16: The figure shows the temperature (in degree C) distribution at the southern and northern transect during the 13th of October 2011. The upper panel presents the temperature profile at the northern transect measured by PoR. The lower panel shows the profile at the southern transect, measured by NIOZ. The temperature ranges from 15 to 16 degrees C.

4.5 Potential Energy Anomaly Analysis

The potential energy anomaly indicates the amount of energy required to mix the entire water column. The higher φ the more energy is needed to mix the entire water column. When φ is larger than zero, there is vertical stratification. It follows that the larger φ the stronger the vertical stratification. Section 3.3 describes how φ is used. First the Potential Energy Anomaly (φ) is calculated for both transects. The results are discussed in subsection 4.5.1. The next step is the analysis of φ changing over time. Within this analysis the different factors affecting the onset and breakdown of stratification are discussed, based on the simplified three-dimensional PEA equation (eq. 3.19). The analysis unravels the stirring and stratifying processes.

4.5.1 Potential Energy Anomaly

Figure 4.17 shows φ in J/m^3 for both transects. Equation 3.2 is used to determine the amount of energy required for complete mixing of the water column. φ is plotted for each measuring point individually and per transect. This gives a proper indication for what really happens in front of the coast and at each location. The figure shows increase and decrease of potential energy during the measurements, which indicates the onset and breakdown of stratification. Both transects show differences per measuring station. The offshore location shows the largest φ. Near shore φ is smaller. Differences between the northern and southern transect were already observed in the salinity profiles. Figure 4.17 shows distinct differences between the northern and southern transect for φ as well. The Northern transect has higher values for φ and shows higher potential energy for almost the entire measurement period. The Southern transect shows a larger φ at the second measurement and again at the fifth. The highest φ is during track six, meaning maximum stratification. This happens during maximum flood velocities which is inline with the tidal straining theory (see figure 4.17).

4.5.2 Change of PEA in time

The change of φ over time is used to investigate the contribution to stratification of different processes. In this section two formula's are used, both are repeated here:
(1) The change of φ in time:

$$\varphi_t \equiv \frac{\partial \varphi}{\partial t} = \frac{g}{H}\int_{-h}^{\eta} \frac{\partial(\bar{\rho}-\rho)}{\partial t} z dz \tag{4.1}$$

(2) The simplified three-dimensional PEA equation:

$$\frac{\partial \varphi}{\partial t} \approx \frac{g}{H}\int_{-h}^{\eta} (\underbrace{\tilde{u}\frac{\partial \bar{\rho}}{\partial x}}_{S_x} + \underbrace{\bar{u}\frac{\partial \tilde{\rho}}{\partial x}}_{A_x} + \underbrace{\tilde{v}\frac{\partial \bar{\rho}}{\partial y}}_{S_y} + \underbrace{\bar{v}\frac{\partial \tilde{\rho}}{\partial y}}_{A_y}) z dz \underbrace{-\epsilon k \rho (\frac{|\widehat{u}^3|}{h})}_{M_{tide}} \underbrace{-\delta k_s \rho_a (\frac{\overline{w}^3}{h})}_{M_{wind}} \underbrace{-0.5\rho_{n,m} f_w \epsilon \frac{U_w^3}{h}}_{M_{waves}} + \underbrace{\varepsilon}_{error} \tag{4.2}$$

The change of φ is calculated based on equation 4.1 and presented in figure 4.18 (the black line). When $\frac{\partial \varphi}{\partial t}$ is positive, the water column is stratifying. As a result φ increases. A negative value for $\frac{\partial \varphi}{\partial t}$ indicates a breakdown of stratification, the water column will mix (φ decreases). A stable water column is present, i.e. the water column is vertically well-mixed or is stable stratified, when $\frac{\partial \varphi}{\partial t}$ is zero. Figure 4.18 shows the simplified three-dimensional equation (equation 4.2) and the time rate of change of φ based on equation 4.1. Deviation between the two equations is observed. The assumptions have an influence on the accuracy of the equation. The different positions in time (see figure 3.17) makes comparison more complicated. In general the trend between the two equations is similar. At station 4 (1 km offshore) the simplified equation follows the same trend as the time rate of change of φ, but it underestimates equation 4.1. The quick increase and decrease of $\frac{\partial \varphi}{\partial t}$ from 12.00 till 15.00 hours is not followed by the simplified equation.

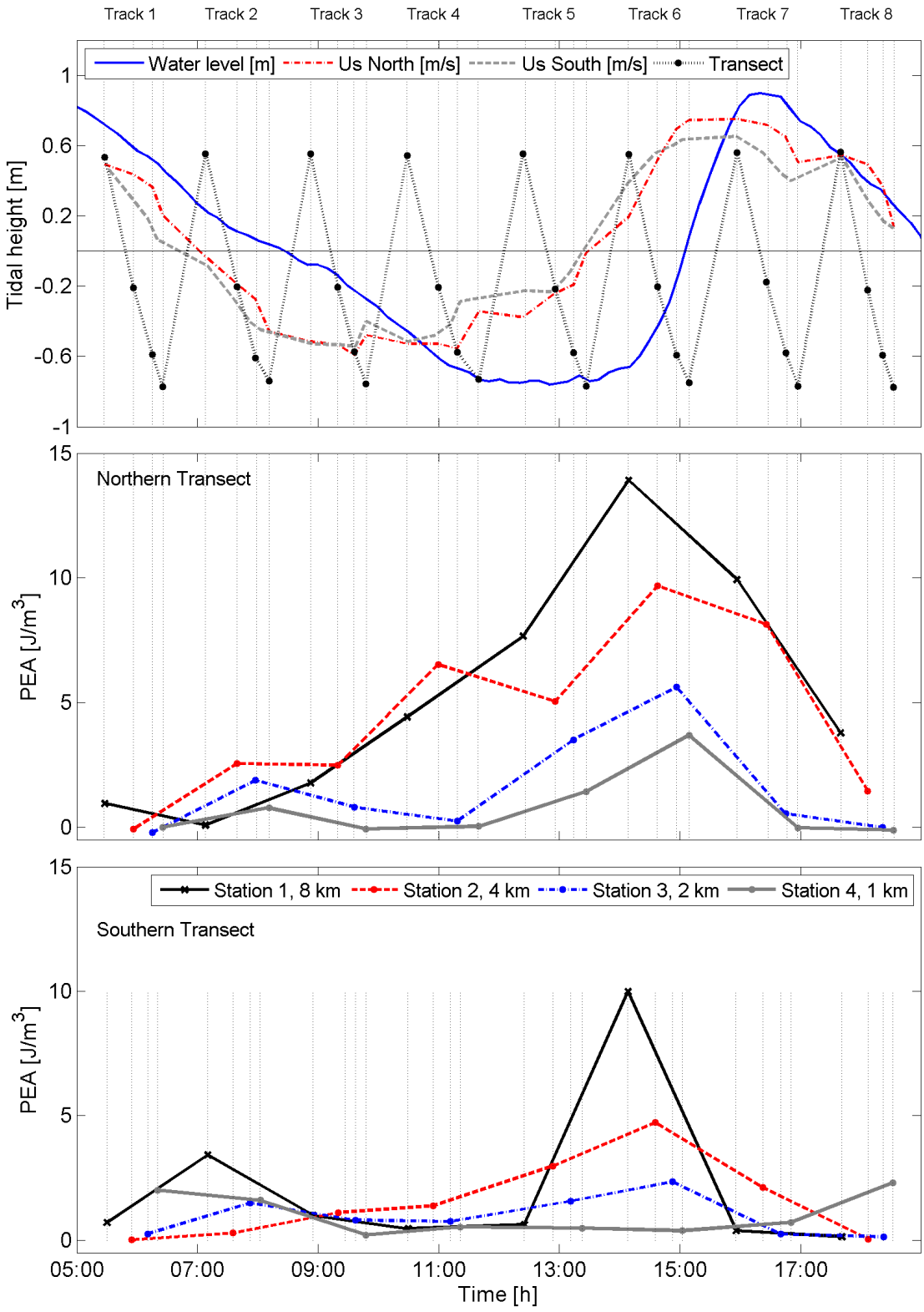

Figure 4.17: The Potential Energy Anomaly (φ) for the Southern and Northern transect. It shows the amount of energy required to mix the water column. The PEA is plotted for each measurement station separate in the time.

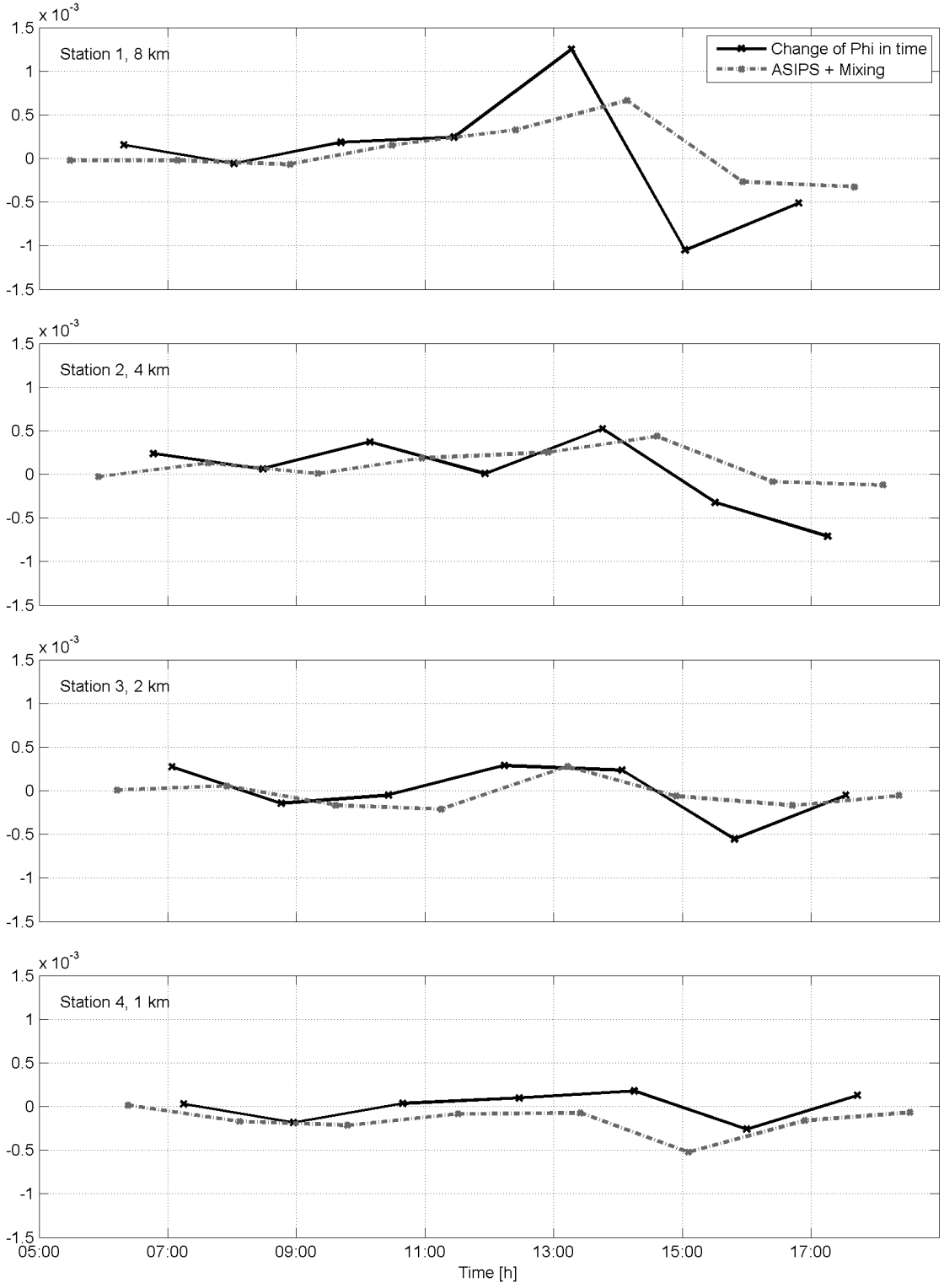

Figure 4.18: The time rate of change of φ and the simplified three-dimensional equation are presented for each station. The black line is the time rate of change of φ (eq. 4.1). The grey dotted line represents the simplified equation, defined as ASIPS+Mixing (eq. 4.2). The terms are expressed in W/m^3.

Simplified three-dimensional equation

Figure 4.19 shows $\frac{\partial \varphi}{\partial t}$ for the simplified equation (eq. 4.2, defined as ASIPS + Mixing). In figure 4.19 a distinction is made between the simplified equation, the change of φ is time, the contribution of advection and straining (ASIPS) and mixing. For each measuring point $\frac{\partial \varphi}{\partial t}$ and the different terms are presented. The Northern and Southern transect together give information about the cross- and alongshore processes, therefore the terms are located between the Northern and Southern transect as shown in figure 3.19.

Each station shows a different behaviour of the ASIPS+Mixing term. Offshore (e.g. 8 and 4 km offshore) ASIPS is dominant and has a large influence on the state of the water column. Negative values for ASIPS+Mixing are observed from the start of the measurements till track 3. The water column is mixing. After track 3, maximum ebb velocities (i.e. LW), ASIPS+Mixing is positive, which means in favour of stratification. After track 6, maximum flood velocities (i.e. HW), ASIPS+Mixing decreases and the water column goes back to a mixed situation. This trend is in line with the tidal straining theory. At 2 km offshore both processes are present and of similar order. In comparison with the two offshore stations mixing energy plays a large role. The water column is only stratifying around track 6 (i.e. maximum flood velocities). At 1 km offshore mixing is dominant. Advection and straining are almost zero and have no influence on the state of the water column.

Advection Straining Induced Periodic Stratification terms (ASIPS)

The total decrease or increase of φ is dependent on cross- and alongshore straining and advection. The ASIPS term in the simplified three-dimensional PEA equation is split into these four processes. Figure 4.20 shows the different terms for each station. Onshore, at station 4, the different advection and straining processes have hardly any influence. For the other stations cross-shore straining is a large contributor. For the stations 1 through 3 this process is in favour of stratification from HW slack (after track 2) till maximum flood velocities. The mixing energy reduces the cross-shore straining, whereas in the end the water column starts stratifying in line with the tidal straining theory, after LW water. After maximum flood velocities cross-shore straining becomes negative, inducing mixing. At station 3 only at track 6 the other processes come into play. More offshore, at station 1 and 2, all the terms have a clear contribution with respect to mixing or stratification. Especially during the tracks four till seven all terms play a role (i.e. from LW till HW).

As concluded before, all the four processes are evident at station 1 and 2 (8 and 4 km offshore). Here, alongshore straining is negative from HW slack (after track 2) till LW slack (after track 5). The velocity shear has higher surface velocities and pushes the fresher surface water southwards. This movement is in favour of mixing. After LW slack (track 5) alongshore straining becomes positive and acts in a stratifying manner. Fresher surface water is transported northwards. This is in line with figure 2.6 from De Boer et al. (2008). Figure 4.20 shows an opposite behaviour of alongshore advection. During ebb (i.e. between track 2 and 5) the alongshore advection is positive, the water column is stratifying. During flood, after track 5, this process becomes negative and tries to get a vertical mixed water column in alongshore direction. This opposite behaviour is not expected in the first place. It is expected that the two processes reinforce each other. Cross-shore advection is visible as well. This process has an influence during track 6 through 8 (during flood). It starts to work in favour of stratification when the water column is already a bit stratified caused by the cross-shore straining term.

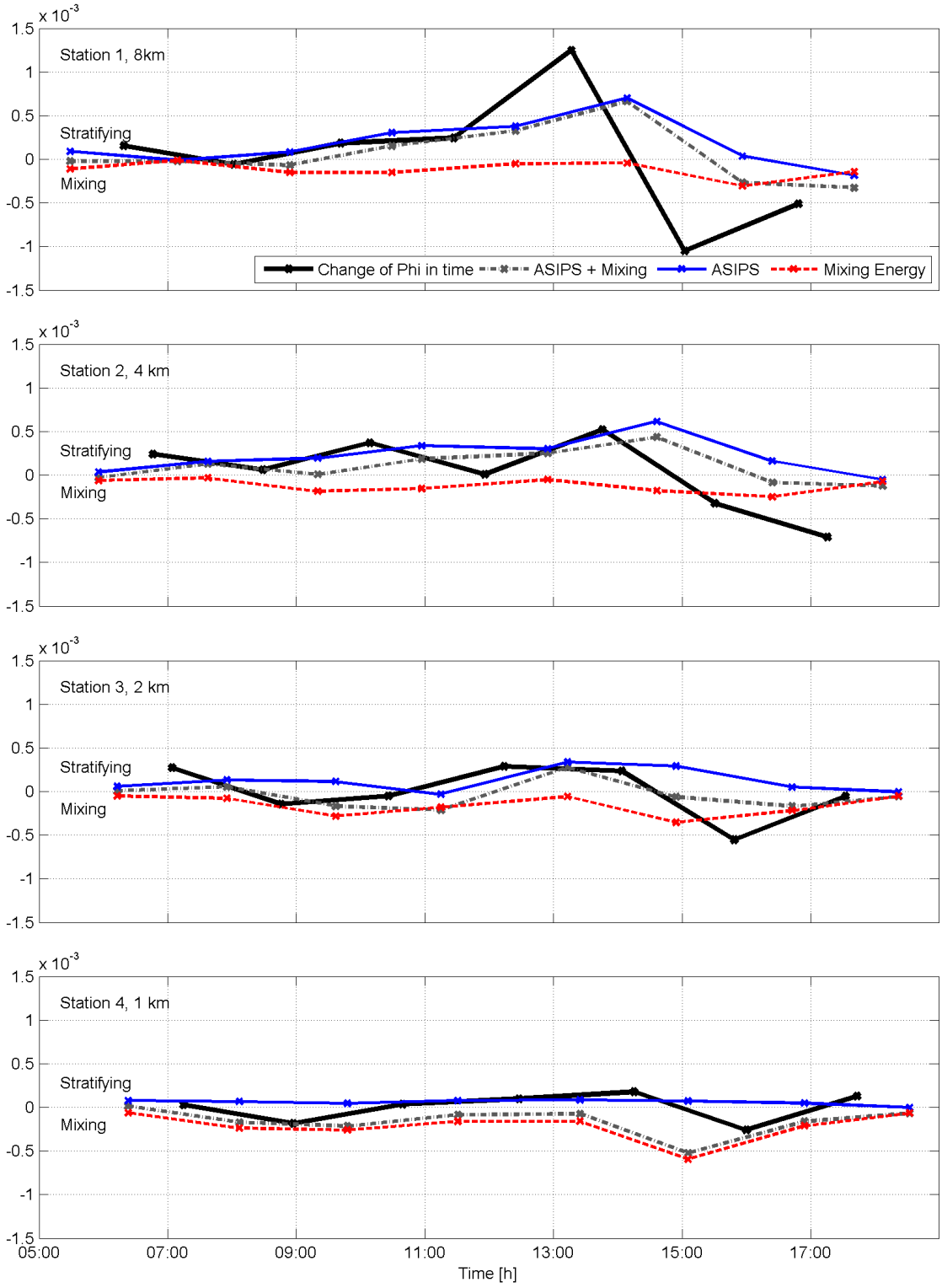

Figure 4.19: The simplified equation (ASIPS+Mixing, eq. 4.2) with the contribution of ASIPS and Mixing separate. The change of φ in time is also drawn in black. The graph shows for each station in grey ASIPS+Mixing with a dotted line , in blue ASIPS and in red with a dotted line the Mixing part. The terms are expressed in W/m^3.

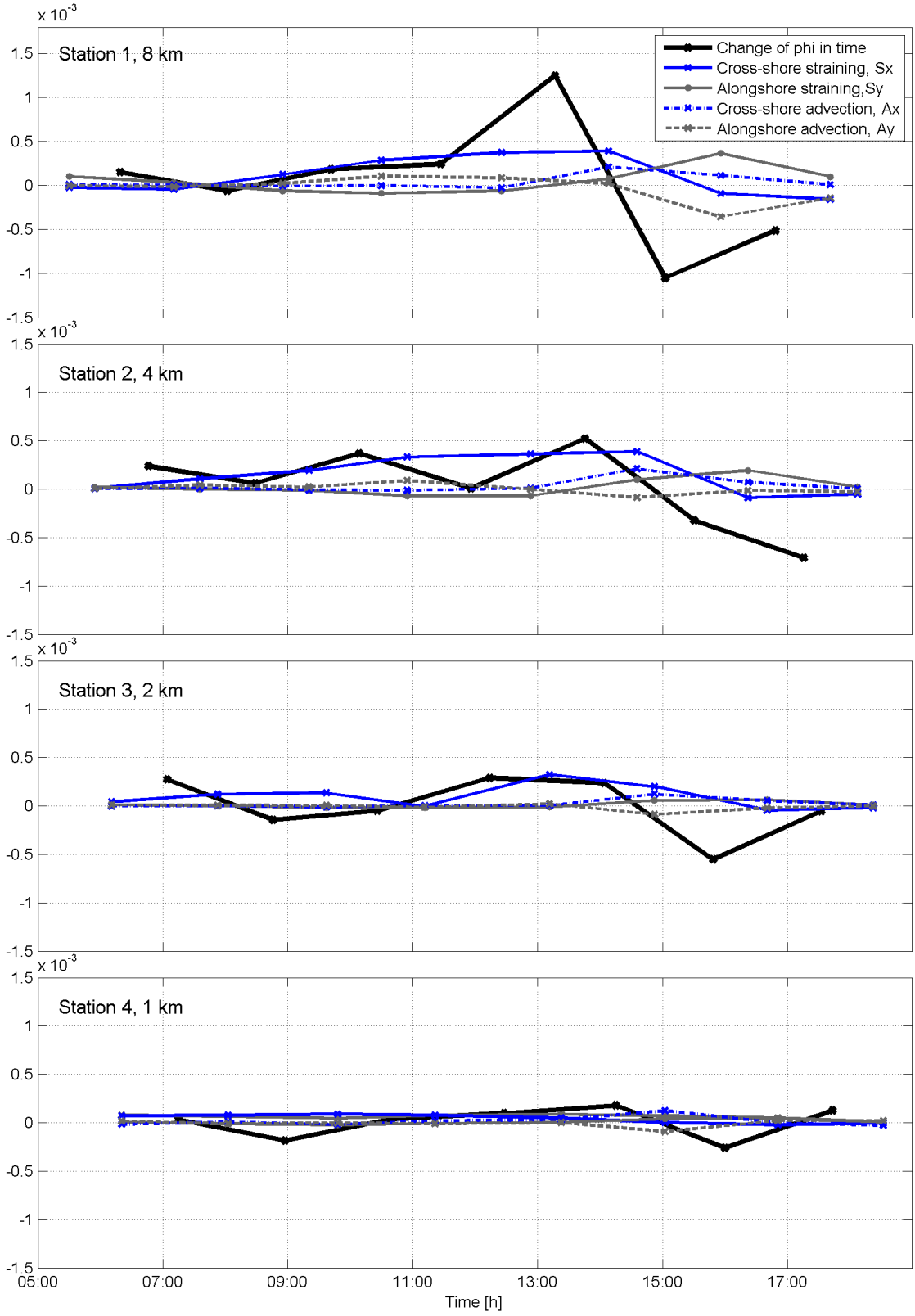

Figure 4.20: The change of φ over time for each measuring station, based on the straining and advection terms (i.e. ASIPS). In black the change of φ over time (eq. 4.1), in blue the cross-shore straining term is presented, in grey alongshore straining, with a blue dotted line the cross-shore advection and with a grey dotted line the alongshore advection. The terms are expressed in W/m^3.

Mixing terms

The different mixing components, M_z, are shown in figure 4.21. Tidal mixing seems to be the dominating factor. Especially the offshore stations show a large contribution of the tide and almost no wind and wave energy. Station 4 shows a different behaviour. Wind and especially waves come into play. The tidal energy seems also larger near shore than offshore. Due to the Kelvin wave the tidal amplitude is highest near shore and decays offshore (subsection 2.4.1). This could be the explanation for the higher tidal mixing energy closer to the coast. From figure 3.14 it is known that during track 3, 5 and 6 the wind increased from 3.5 to 4.5 m/s. The wind mixing for these measurements show a slight increase. Where the wind velocity decreases the wind mixing follows the same pattern and decreases. Wind mixing is low in comparison with tidal mixing. At station 4 the contribution is somewhat larger than offshore. During these measurements the wind velocity was moderate. Near shore, at station 4, wave mixing becomes more important. During track 5 an increase of wave energy is observed. This is in agreement with the increasing wind (figure 3.15 and 3.14), resulting in an increase of the significant wave height and wave period thus in larger mixing energy. The greater influence of waves onshore can be explained by the fact that waves have a larger impact in shallow water. The orbital velocities near the bottom cause higher bed shear stresses which enhance wave mixing.

Comparing ASIPS terms between Northern and Southern transect

For each transect the cross-shore processes can be observed as well. This is presented in the figures 4.22 and 4.23. Figure 4.22 shows the comparison between ASIPS and Mixing between the two transects. The total quantity of mixing energy for both transects appear to be similar. The stratifying terms, on the other hand, seem to differ. The Northern transect shows overall larger values for ASIPS. Figure 4.23 presents that the cross-shore straining term causes this difference. The Northern transect shows a larger contribution of cross-shore straining, than the Southern transect. At station 4, 1 km offshore, no difference between North and South is observed, all the terms are close to zero. During track 4 through 6 (i.e. LW slack till maximum flood) the cross-shore straining at the Northern transect is twice as high as at the Southern transect, at station 1 (8 km offshore). Figure 4.14 shows stratification during track 3 through 5 for the Northern transect, whereas the Southern transect has a vertical mixed water column. Stronger cross-shore surface currents inducing higher cross-shore straining can be the explanation of the difference in stratification between both transects. The cross-shore advection term, which comes into play around track 6, shows slightly larger values for the Northern transect than for the Southern transect.

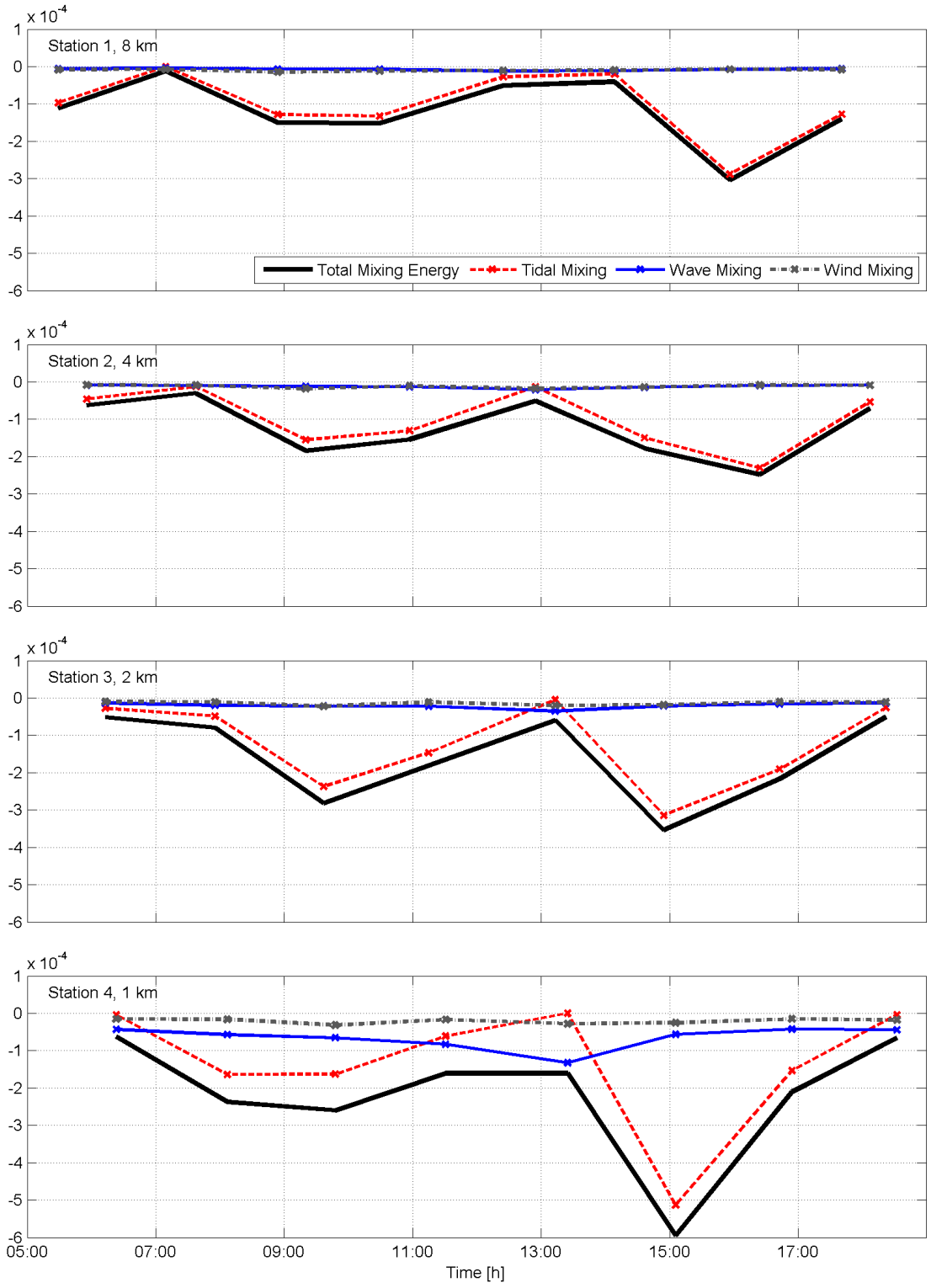

Figure 4.21: For each station the different mixing terms are presented. The black line is the total mixing energy, the red dotted line the tidal energy, the blue line wave mixing and the dotted grey line wind mixing. The terms are expressed in W/m^3.

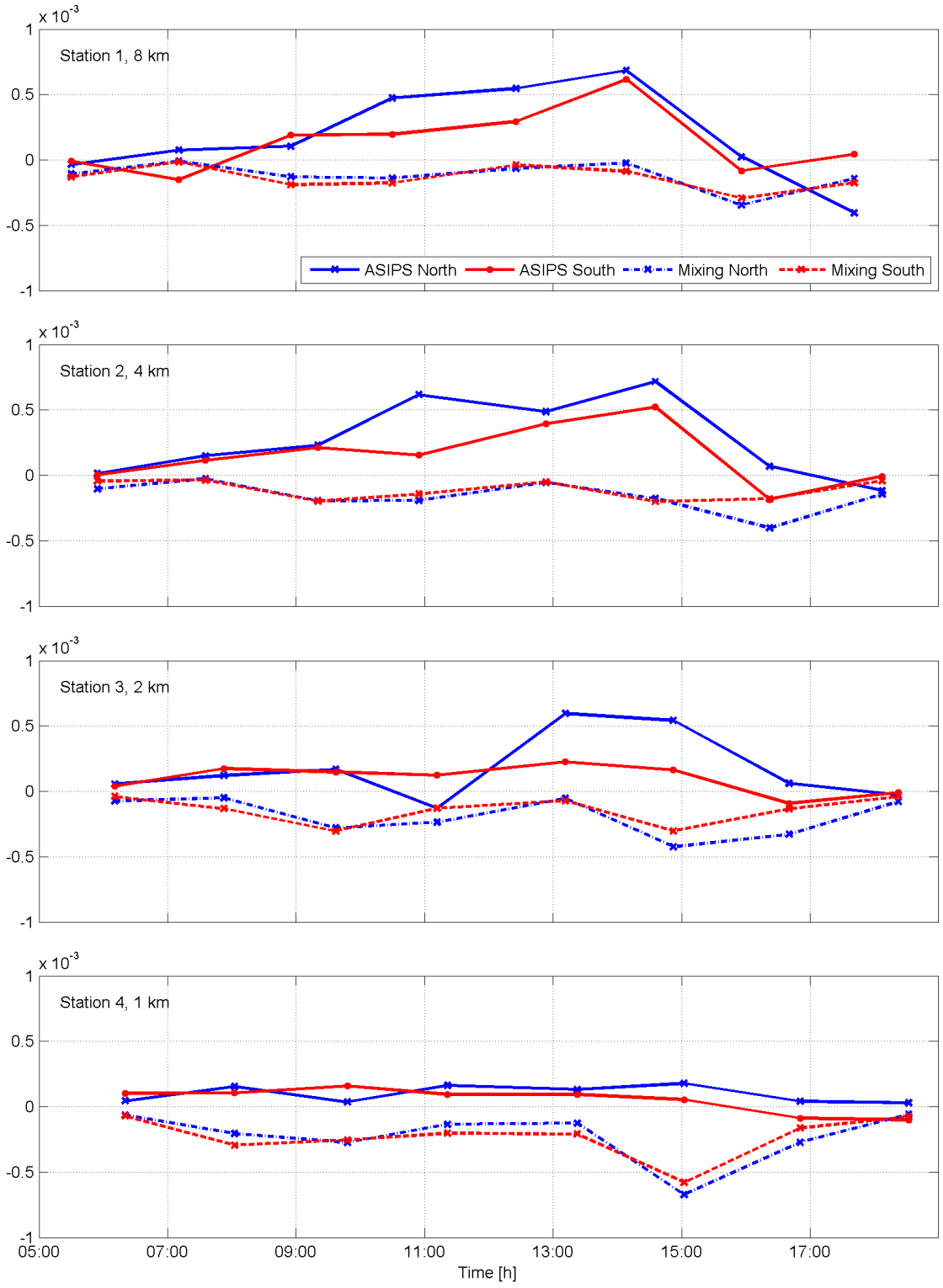

Figure 4.22: The cross-shore ASIPS terms are compared with the mixing terms for the Northern and Southern transect. The terms are presented per station. In red the terms for the Southern transect and in blue for the Northern transect. The terms are expressed in W/m^3.

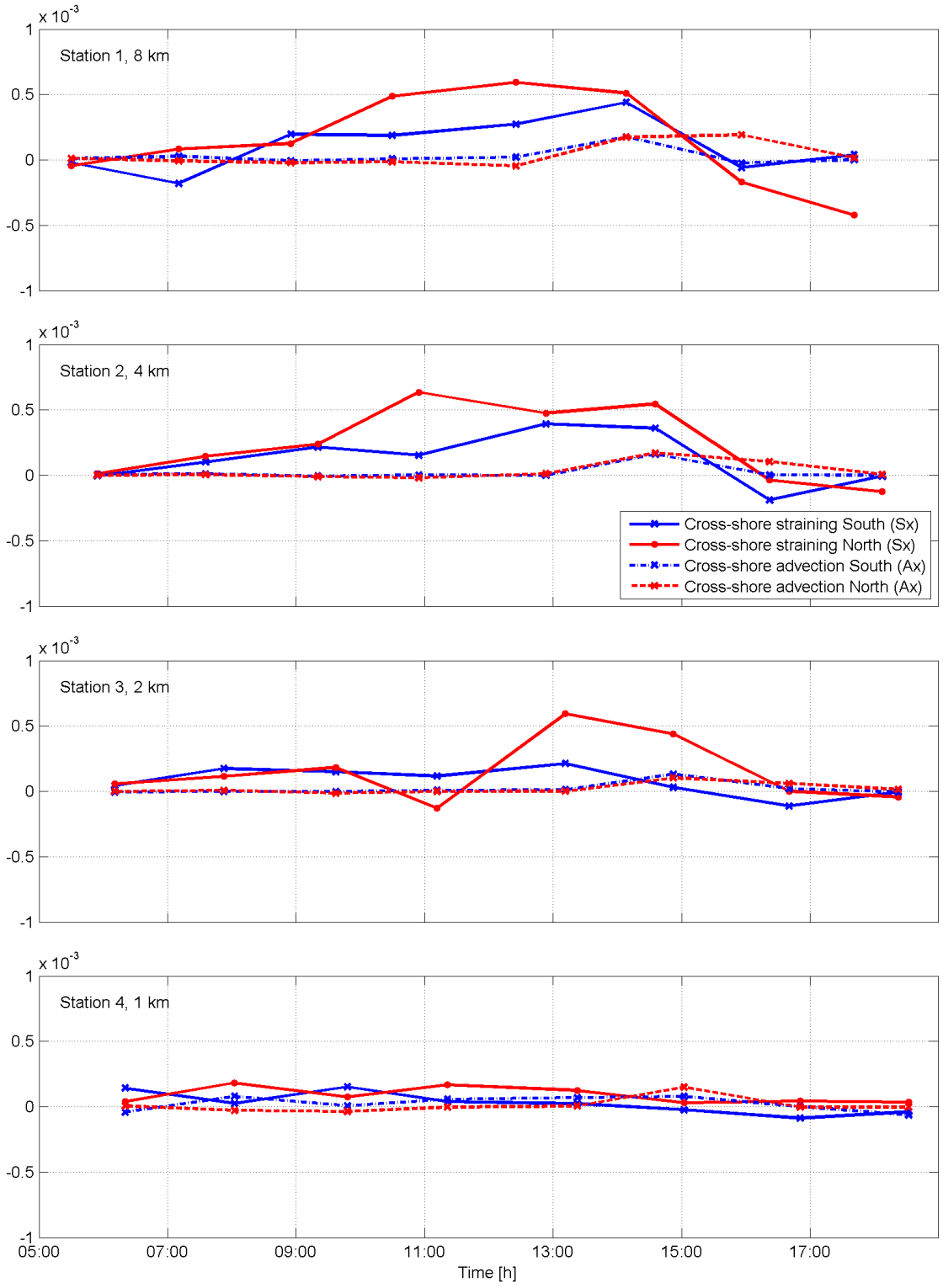

Figure 4.23: The cross-shore terms for each transect are presented. In red the straining and advection terms of the Northern transect and in blue for the Southern transect. The terms are expressed in W/m^3.

4.6 Suspend Particulate Matter

Figures 4.24, 4.14 and 4.15 (lower panel) show the measured SPM values in mg/l. These results will be analyzed qualitatively. Figure 4.25 shows the measured bottom and surface concentrations per station. The Northern and Southern transect will be observed separately because of problems with the calibration between the OBS sensors and the determination of the depth for the NIOZ measurements.

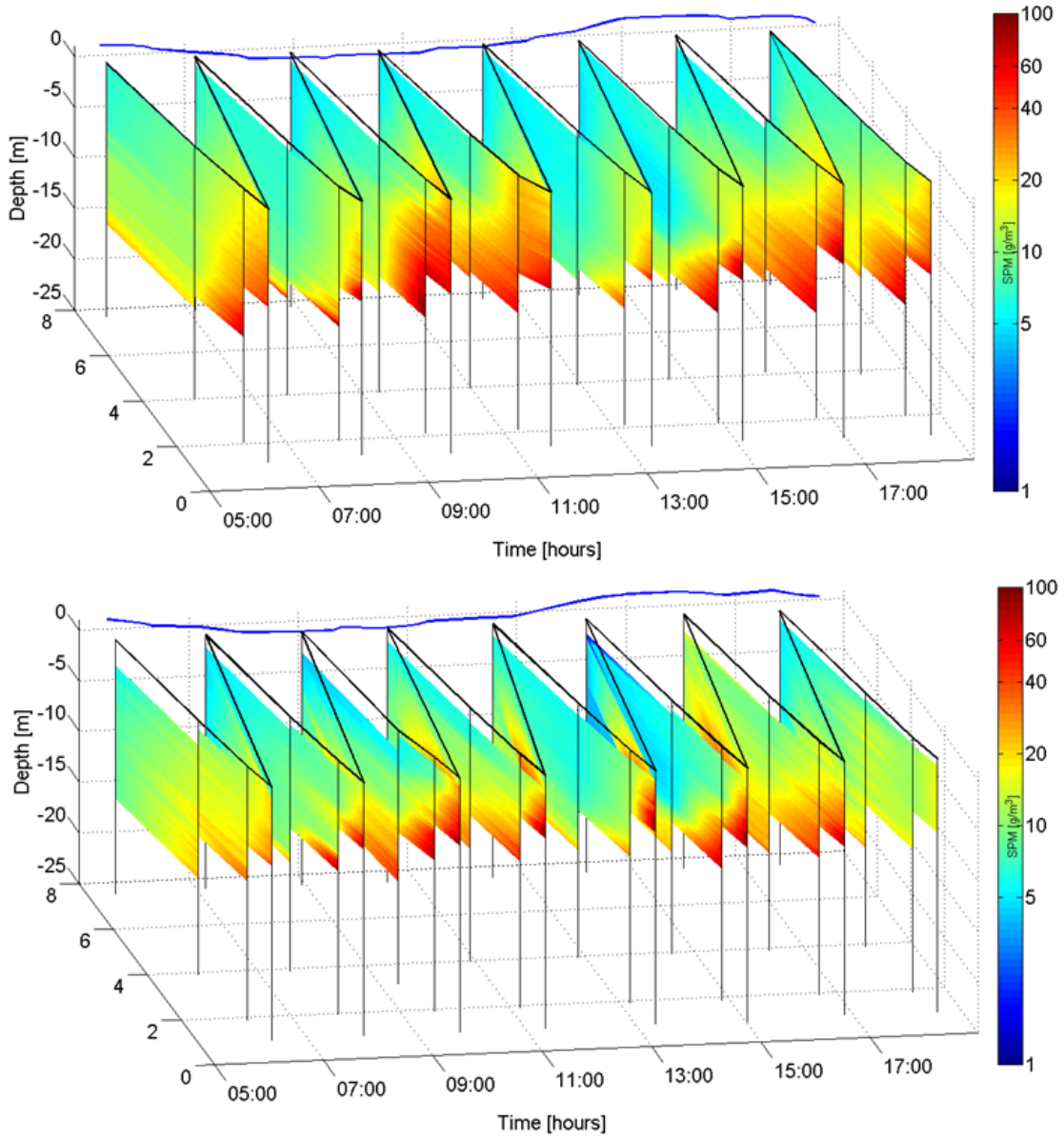

Figure 4.24: The SPM profile during the measurements in three-dimensions is shown. The upper panel shows the profile of the northern transect measured by PoR. The lower panel presents the southern transect measured by NIOZ. The SPM values ranges from 0 till 100 mg/l. The vertical axis represents the depth. The horizontal axes are the distance to the shore and the time.

High concentrations are found near the bottom onshore (at the third and fourth stations, 2 and 1 km from the shoreline), which is in line with Van der Hout et al. (subm.). The bed concentrations are at least 30 mg/l and maximum values exceeding 100 mg/l are found. These high concentrations are observed at the Northern as the Southern transect. At the onshore stations the largest surface concentrations are found as well, which are mostly less than one fourth of the bottom concentra-

tions. Therefore, at the onshore stations concentrations over the entire water column are present. Offshore the concentrations are much lower. The influence of waves and tides is less because of larger depth.

Near the bottom higher concentrations are observed than near the surface, during the entire campaign. This is in line with a rouse profile which is common for sediment, also for silt. The surface concentrations reach a maximum value of 25 mg/l, which is observed at the onshore stations (at 1 and 2 km). Offshore the concentrations are much lower, near the bottom and near the surface. The influence of waves and tides is less because of larger depth.

Figure 4.25 shows a different trend for the different stations, for each transect, for the bottom SPM concentrations is time. The data shows the following behaviour. When the ebb current is increasing and reaching its maximum (track 2, 3 and 4), the bottom concentrations increase (figure 4.25). During track 5 the ebb current decreases. This decrease goes in accordance with a decrease of SPM concentrations near the bottom, resulting in low concentrations of SPM (in order of < 25 mg/l). A high tidal current, track 7, shows again larger values of SPM in the water column. The response of SPM during stratified conditions is difficult to examine from the results.

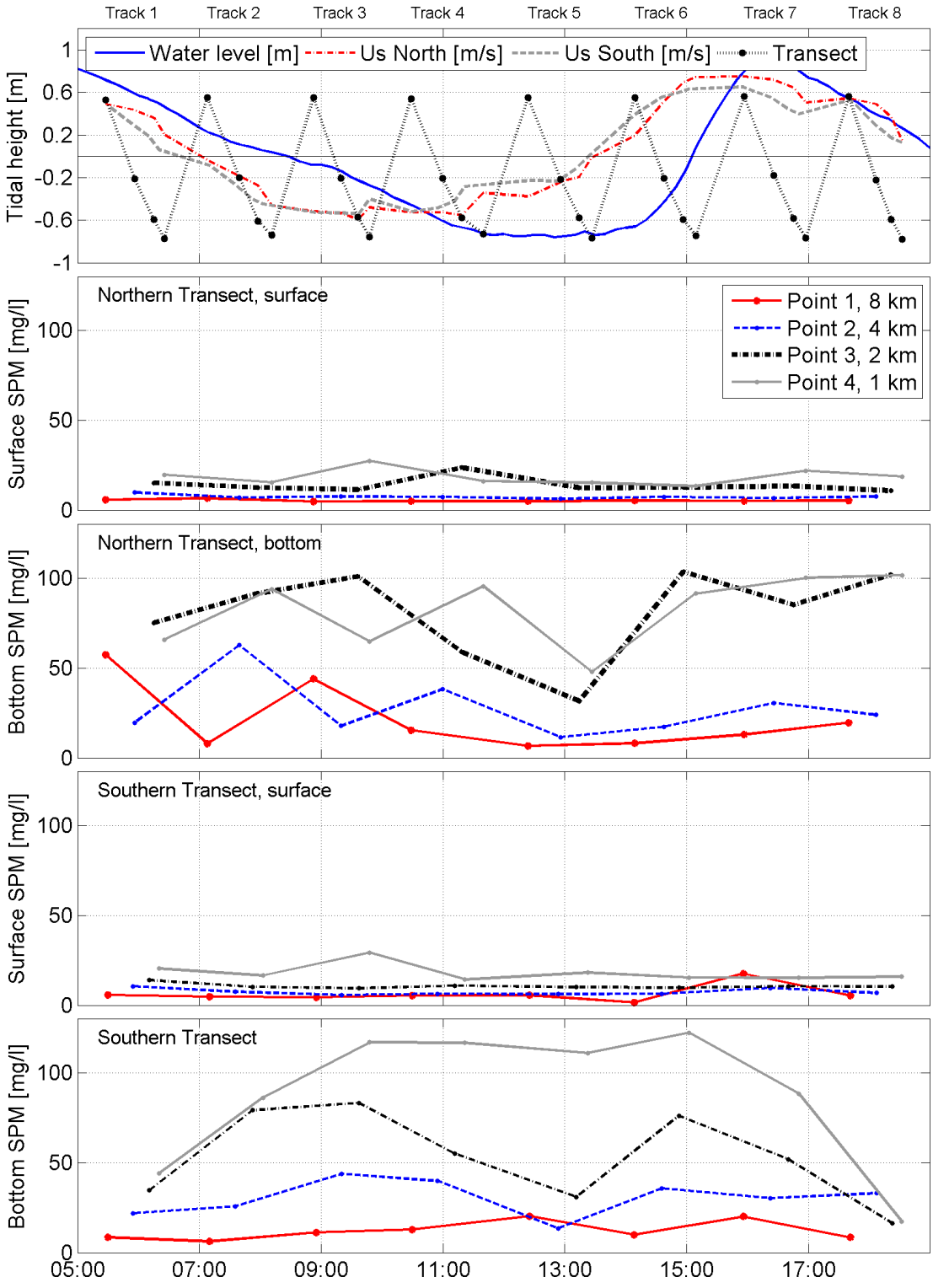

Figure 4.25: Bottom and surface SPM for Northern and Southern transect. The panels show from top to bottom the following information: (1) The tidal height and the sailed transect in time. The blue line is the tide near IJmuiden Buitenhaven in m. The red and grey dotted line are the measured depth mean alongshore velocities at both transects in m/s, where positive is northward (2) Surface SPM concentrations in mg/l, Northern transect (3) Bottom SPM concentrations in mg/l, Northern transect (4) Surface SPM concentrations in mg/l, Southern transect (5) Bottom SPM concentrations in mg/l, Southern transect.

Chapter 5

Discussion

A unique in-situ dataset was used to study the complex four dimensional nature of the Rhine river plume. The competition between the stratifying and mixing processes on the behaviour of the plume 80 km downstream the river mouth has been investigated with the Potential Energy Anomaly analysis. The analysis is performed in four dimensions by using a dataset collected with two vessels. The influence of the alongshore straining and advection on the river plume is investigated with this dataset. The measurement campaign was performed one day before spring tide. Stratification is not only controlled by the spring-neap tidal cycle, but also by wind and fresh water discharge. Throughout this chapter, the maximum flood current is defined as High water (HW) and the maximum ebb current as Low water (LW).

During the measurements there was an east and northeast wind with a magnitude between 3.5 and 4.5 m/s. Based on the theory mentioned in section 2.5 the wind causes an ageostrophic (or frictional) response in the direction of the wind. When the water column is (weakly) stratified the wind causes an Ekman response to the right. This resulted in an offshore ageostrophic movement and a northwards Ekman response during the measurement campaign. Pietrzak and De Boer (in prep.) and Van Wiechen (2011) showed that weak offshore winds (perpendicular to the coast) displace the entire ROFI offshore and northwards. This movement enhances stratification. From this we can expect that the wind can lead to a displacement of the plume offshore and to the north (when weak stratification is present).

Figure 5.1 shows the expected range in which direction the surface water is displaced. On the left the situation for an offshore wind as discussed by Pietrzak and De Boer (in prep.); Van Wiechen (2011) is sketched, on the right the situation for an eastern wind is sketched. During the measurement campaign both the direction of the wind, and the state of the water column change. As a result, the response of the plume changes. Larger stratification results in a larger Ekman response. Figure 5.2 shows a sketch of the expected influence of the wind on the plume during the campaign. The movement of the plume by the wind can work in favour of stratification.

Temperature and salinity

Salinity and temperature data show the presence of water with a salinity of 30 PSU at 1 and 2 km offshore, which is an indication of the presence of water from the Rhine River. The existence of the plume 80 km downstream is in accordance with De Ruijter et al. (1997), who observed the plume even at a distance of 100 km from the river mouth. The data indicates that the ROFI is narrow, well-mixed and located close to the coast at the start of the measurements. The location of the plume can be explained by the storms of the previous days. Wind speeds of 12 m/s from the West-South-West direction displaced the plume towards the coast and southwards, resulting in a narrow well-mixed plume against the coast (Pietrzak and De Boer, in prep.). The day before the campaign, the wind speed decreased and veered into a moderate easterly wind (this is illustrated in figure 3.12).

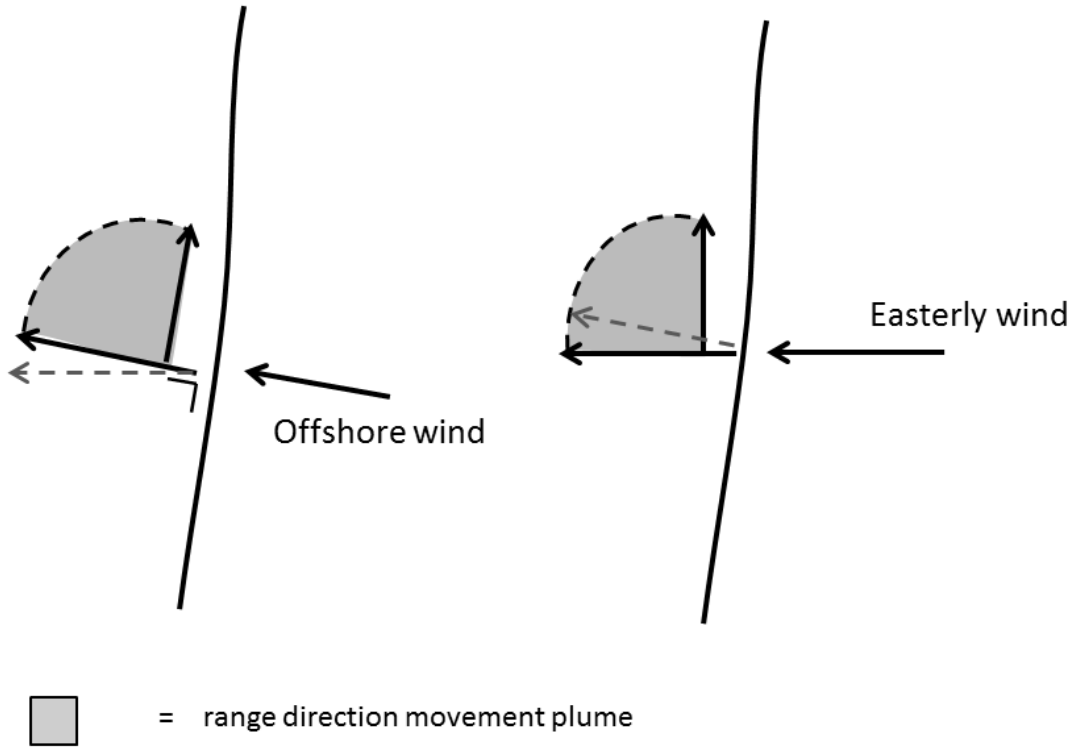

Figure 5.1: A sketch of the influence of the wind in the plume. The black arrows indicate the frictional response (in the direction of the wind) and the Ekman reponse of the water. The left figure represents the possible movement of the plume as a result of an offshore wind, as investigated by Pietrzak and De Boer (in prep.); Van Wiechen (2011). The grey dotted line is the direction of an eastern wind. The right figure shows the possible movement of the plume as a result of an easterly wind, as the case for this study.

The data shows horizontal stratification, both in the cross-shore and the alongshore direction. An alongshore salinity gradient is observed. Despite the short distance between the transects (12 km), differences in salinity are found, the differences are largest offshore at Station 1. The water at the northern transect is more dense than at the southern transect. The salinity difference is between 0.5 and 1.0 PSU, which is small. Figure 5.3 shows a sketch of the isohalines during the measurements. These isohalines show the presence of the density differences between both transects. The salinity differences, between the two transects, can be ascribed to the shape of the plume. The plume is much narrower at 80 km distance from the mouth than at 30 km (e.g. Suijlen and Duin (2002), De Boer (2009), Van Wiechen (2011)).

The presence of breakwaters at IJmuiden can have an influence on the distribution of the plume as well. Due to the disruption of the coastline, extending about 1.60 km into the sea, the plume is forced to bend around the breakwaters. However, there is no clear indication how the plume bends around the breakwaters and if it has an effect 7.50 km northwards at the southern transect. The North Sea Channel at IJmuiden sluices an amount of 120 m^3/s freshwater into the North Sea at the 13th of October and the days before. This discharge can influence the distribution of the plume as well, due to the flow of low saline water.

Vertical stratification is observed during the measurement campaign as well. The maximum salinity difference over the vertical is about 1 PSU at both transects. This indicates weak stratification. The plume mixes when it moves northwards. As a result, the plume becomes more saline and the salinity difference with the seawater decreases. The observation is in line with De Kok (1996), who

Figure 5.2: The sketch shows the expected movement of the plume during the measurements. Four periods during the campaign are sketched. The sketches are based on the Northern transect. For the Southern transect the same principle holds. Only the second figure deviates. The plume moves in the direction of the wind, the Ekman response depends on the state of the water column. An Ekman response occurs only when the water column is (weakly) stratified. The black arrows indicate the range of the expected movement of the plume.

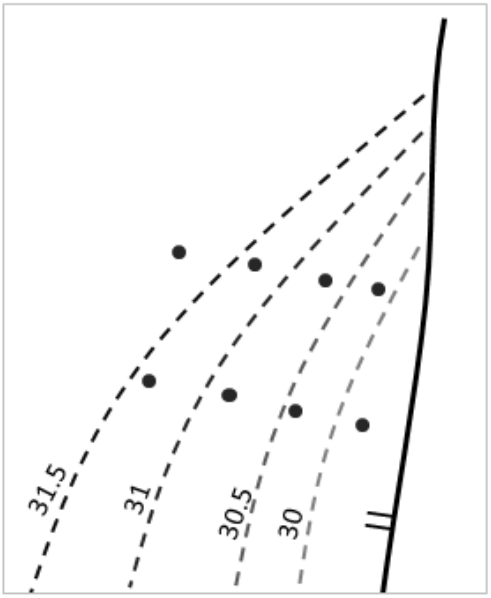

Figure 5.3: A sketch of the isohalines based on the 13 hours measurements. At every station of the Northern transect is slightly more saline than at the Southern.

found vertical salinity differences of less than 2 PSU at a distance of 50 km downstream of Hoek van Holland. It is also in agreement with De Ruijter et al. (1993) who found weak stratification at Callantsoog (100 km downstream the river mouth).

During the 13 hours an alternation between a well-mixed and stratified water column is observed.

The onset and breakdown of stratification is in line with the tidal straining theory as found in the Rhine ROFI (Simpson and Souza, 1995). Maximum stratification occurs at HW and both transects are well-mixed during LW. The measurements were performed close to spring tide. Spring tide means large tidal energy, which mixes the water column. Following (Simpson et al., 1993) the water column is well-mixed during spring tide.

The weak stratification around spring tide can be the result of the weak easterly wind, which enhances stratification. In addition the discharge of 120 m^3/s at the North Sea Channel at IJmuiden could enhance weak stratification as well, due to the flow of low saline water. Nauw and van der Vegt (2012) found evidence for stratification during spring tide near IJmuiden as a result of a weak offshore wind and a peak in the discharge at IJmuiden. However, their situation was more extreme, in the sense they found stronger stratification in combination with a higher discharge.

Moreover, a different trend regarding vertical stratification is observed between the Northern and Southern transect (this difference is clearly shown by the figures D.1 and D.2 in Appendix D). The Northern transect shows stratification from LW until HW, especially at the offshore stations. The southern transect behaves differently, stratification is only observed during HW. Thus, the Northern transect shows stratification over a longer period. As a result the cross-shore velocities can be larger, inducing larger cross-shore straining at the Northern transect, enhancing stratification.

Potential Energy Anomaly

The potential energy anomaly, φ, is large 8 km offshore and shows smaller values closer to the coast. High values of φ coincide with a peak in vertical stratification. The trend of a larger φ offshore and smaller values of φ onshore is observed at both transects. In contrast, De Ruijter et al. (1997) found highest vertical stratification 3 to 5 km offshore, instead of 8 km offshore. The stronger stratification offshore and the weaker stratification onshore can be explained as follows. Onshore, mixing processes become more dominant, because of the smaller water depth the tide and the waves are more influenced by the bottom. The wind plays a role in this phenomenon as well. An easterly wind displaces the plume offshore and alongshore. As a result φ decreases near the coast and increases with distance from the shoreline (Van Wiechen, 2011).

A simplified form of the three-dimensional Potential Energy Anomaly equation is used to investigate the contribution of the stratifying and mixing processes. The stratifying processes are enhancing stratification and within this study the cross-shore straining, cross-shore advection, alongshore straining and alongshore advection are investigated. The mixing processes are governed by tidal, wind and wave stirring. At the stations offshore (at 4 and 8 km) the advection and straining processes are dominating and determine the periodic stratification. From LW till HW they work in favour of stratification, while after HW the processes are in favour of stirring the water column and enhance the kinetic energy available for mixing. Onshore, the mixing processes are dominant. The same phenomenon is described by De Ruijter et al. (1997), who found maximum stirring energy at distances less than 3 km from the shoreline. Tidal stirring is the strongest mixing process at all the stations. Onshore (at 1 km), wave and wind mixing have a contribution as well, while offshore these processes are negligible. The higher stirring energy onshore is caused by the shallower water, such that bed friction has a larger influence on the tides and the waves. Increased wind velocity results in higher waves. Consequently, energy for mixing the water column due to waves increases.

The simplified three-dimensional Potential Energy Anomaly equation shows that cross-shore straining is the dominating process inducing periodic stratification. This is in line with Simpson et al. (1993) and De Boer (2009). The cross-shore straining works, as expected, by the tidal straining theory (Simpson and Souza, 1995). The process works in favour of stratification from LW till HW. From HW untill the end of the measurements cross-shore straining works in favour of stirring the water column (see figure 2.5). The cross-shore advection comes into play around HW, it works in favour of stratification around HW at every station. The timing of the cross-shore advection is in line with the expectations. Stratification in cross-shore direction first has to be induced by cross-shore straining before advection can enhance stratification.

The study shows the presence of alongshore straining and advection as well. The alongshore straining works in favour of mixing during ebb and in favour of stratification during flood. This is in line with the theory (De Boer, 2009) (figure 2.6) and can be explained as follows. During flood, the higher surface currents push the fresher surface water northwards (i.e from south to north) over the denser bottom water, inducing stratification. During ebb the reverse occurs; the ebb current is directed southwards and pushes the fresher surface water back southwards, inducing a mixed water column.

Based on De Boer et al. (2008) it was expected that alongshore advection works in favour of stratification during flood, i.e. directed from south to north, as the water column is expected to be more mixed northwards. Therefore, the flood current advects a more stratified density profile northwards, enhancing stratification. However, within this study the alongshore advection works in favour of stratification during ebb, i.e. directed from north to south. Hence, the advection works in the opposite direction of what was expected. Figure 5.4 shows the expected working of the alongshore advection and the observed behaviour.

The unexpected working of the alongshore advection is caused by the fact that the Northern transect is more stratified than the Southern transect. The two transects do not provide enough information in the alongshore direction to conclude whether it is general for this location that the Northern transect is more stratified than the Southern transect, or whether it is coincidence.

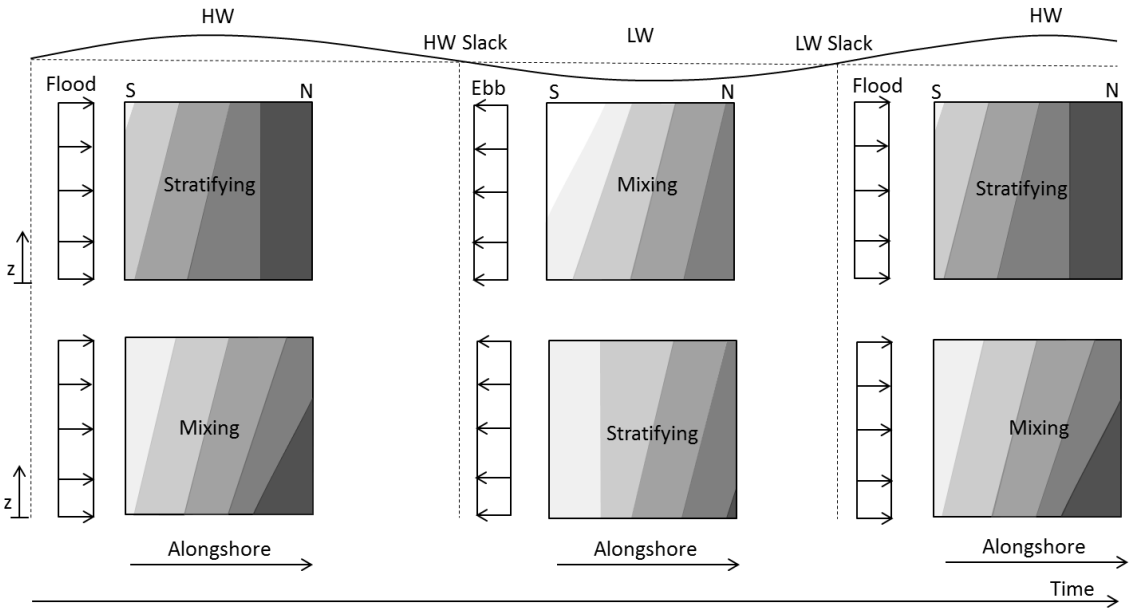

Figure 5.4: Explanation of the alongshore advection term. Within the figure the density field is frozen, it does not deform, it only moves. (1) The upper panel shows the expected situation following the theory by De Boer et al. (2008). At the Southern transect the water column is more stratified than at the Northern transect. Therefore, during flood advection works in favour of stratification and during ebb in favour of mixing. The maximum stratification in alongshore direction occurs at HW slack and well-mixed at LW slack. (2) The lower panel shows the observed situation. The Northern transect is more stratified than the Southern transect. Therefore, advection works in favour of mixing during flood. During ebb, advection works in favour of stratification.

Tidal ellipses

The vertical velocity structure shows the existence of cross-shore velocities. In line with the classical theory (Souza and Simpson, 1996) the surface velocity turns anti-cyclonically and near the bottom

cyclonically. The shape of the ellipses is oblong at the surface. Near the bottom more circular shaped ellipses are formed. Ellipticities of -0.1 and 0.1 are observed. An ellipticity of 0.1 is small, resulting in oblong ellipses. Around neap tide ellipticities of 0.4 normally occur. Around spring tide the ellipticity is generally around zero (i.e. only alongshore velocities are present). So, according to the ellipses the situation is near spring tide, yet there still is some stratification. Between both transects the different behaviour with respect to stratification is also observed in the shape of the tidal ellipses. The ellipses at the Northern transect have more of a circular shape, indicating stronger stratification.

Suspended Particulate Matter

A first step is taken towards the understanding of the distribution of SPM along the Dutch coast. The SPM data is analysed qualitatively in order to have a first analysis of its distribution. High concentrations are found onshore near the bottom, at 2 and 1 km from the shoreline (stations 3 and 4). This is in agreement with the observations of Van der Hout et al. (subm.). This confirms the existence of a narrow band of high SPM concentration within 3 km from the North Holland coastline. However, more insight into the shape and behaviour of the hotspots is not obtained because of the limited resolution of the dataset.

In addition, the observations indicate an influence of the tidal current on the SPM concentrations. In general the SPM concentration varies with the movement of the tidal current, however the velocity at which the silt is displaced is lower than the depth averaged tidal velocity (de Kok, 2004). The response time of SPM depends on different factors, e.g. the settling velocity, the water depth, the asymmetry of the tide and the composition of the particles. This suggests that more data is needed to determine the response of the SPM on the tidal current.

No clear evidence was found for the influence of stratification on the SPM distribution for the measured period. Distinct sinking of SPM as a reaction on stratification, as found by Joordens et al. (2001), cannot be determined from the data. The stratification was weak and only a thin upper layer of fresher water was present. It can be questioned whether the stratification was strong enough and whether the measured time was long enough to observe the response of SPM. More data in time is needed to investigate the influence of the tidal current and stratification on the distribution of SPM. With more data in time and a proper relation between both OBS sensors advection and the movement of SPM in alongshore direction can be investigated.

Large scale dataset

The analysis of the two parallel transects gives insight into the area far downstream from the river mouth and is only a small part of the large scale dataset obtained by PoR. However, this knowledge can be used to understand the response of the ROFI and to help to interpret the large scale dataset. The large scale dataset obtained by PoR contains a wide range of data collected under many field conditions. The first analysis of this large scale dataset can be found in Appendix B and indicates that the ROFI is very dynamic and variable. The scatter plots highlight the complex interplay between all the physical processes in the Rhine ROFI. However, the plots show some trends, they indicate where freshwater exist and where resuspension of SPM occurs. The scatter plots show a distinct fresh water plume extending about 100 km downstream (figure 5.5, upper left panel). This is in agreement with earlier findings by De Ruijter et al. (1997) and Suijlen and Duin (2002). It is also in agreement with the analysis of the two parallel transects (see section 4.3). Note that the PoR transect is included in figure 5.5 and the NIOZ transect is not. Figure 5.5 (upper right panel) shows large density differences around the river mouth and downstream close to the coast. In general density differences decay northwards. South of the river mouth the water column is generally well-mixed, especially in the region south of the Westerschelde (Fettweis and Nechad (2010)), which is not within the large scale dataset. However, a few times evidence of freshwater is found in the region south of the Rhine river mouth. In general the times series at Wijk and Egmond aan Zee analysed here compared to the results of Noordwijk as described in Smolders (2011) give the same results, and are in agreement with De Ruijter et al. (1997) and

Giessen et al. (1990).

Additionally, the scatter plots indicate the influence of the season on the behaviour and state of the plume (figure B.3). Thermal radiation becomes important during the summer and reinforces stratification (figure B.4). The scatter plots support the findings of Joordens et al. (2001) and De Nijs et al. (2010), which indicate that stratification shuts down turbulence and lead to an decrease of SPM at the surface. When the plume is stratified the surface SPM has decreased and the bottom SPM has increased (figure 5.5, lower panels). Highest SPM values are found along the coast in a narrow band.

It can be concluded that the scatter plots just indicate the region influenced by the ROFI. However, the plots do not indicate where it is at any a given time or why. Statistical methods, such as multivariate analysis, could be a tool to analyse the large scale dataset to obtain more insight into the behaviour of the Rhine ROFI and the distribution of SPM. In the framework of environmental studies by PoR, the studies done by Smolders (2011) and Van Wiechen (2011) together with the analysis of the two parallel transects near IJmuiden in this study give a better understanding of the Rhine ROFI. Therefore, these studies can be used in the analysis of the large scale dataset and used in future research.

Summary

In short, the Rhine ROFI is present 70 to 82 km downstream. Wind has an impact on the position of the plume. As a result of the high wind conditions the days before the measurement campaign, the plume was narrow and well-mixed. During the measurement campaign the wind varied between an eastern and north-eastern wind. At the beginning of the measurements, the wind displaces the plume to the west, when stratification becomes larger the plume is also displaced more northwards, as a result of the Ekman component. The two transects behave differently with respect to stratification. The Northern transect shows a longer period of stratification. This results in larger offshore directed currents at the surface, which enhances stratification. Tidal ellipses are observed at both transects, in accordance with the tidal straining theory. The potential energy anomaly analysis shows that cross-shore straining is the dominant process inducing stratification. However, the other processes are present as well. All the cross- and alongshore processes work as expected (De Boer et al., 2008), except for the alongshore advection. The alongshore advection works in favour of mixing during flood and in favour of stratification during ebb, as a result of the more stratified Northern transect. Furthermore, the alongshore processes are present 80 km downstream the river mouth and not only in the bulge region.

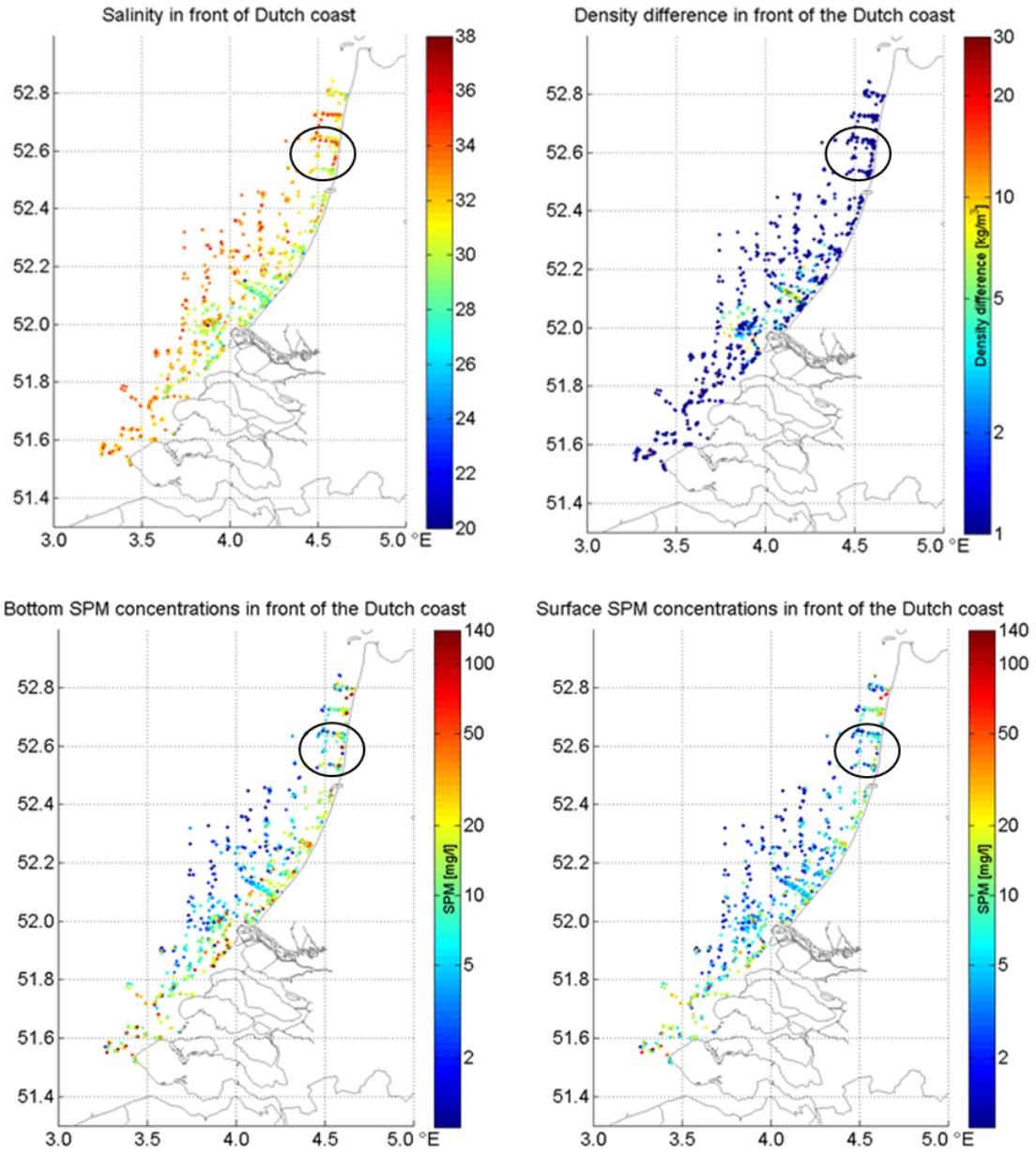

Figure 5.5: An overview of the large scale dataset by scatterplots. The upper left panel shows the salinity data in front of the Dutch coast in psu, the upper right panel the density difference (in kg/m^3) and the lower panels the bottom and surface SPM respectively in mg/l.

Chapter 6

Conclusions and recommendations

The unique in-situ dataset of the PoR and NIOZ led to new insights into the dynamic four dimensional nature of the Rhine ROFI, 80 km downstream of the river mouth (Hoek van Holland). The use of two vessels simultaneously for obtaining information in four dimensions is on the verge what is actually possible with ships. Hence, it can be concluded that this first attempt to measure in four dimensions with two vessels is an innovative approach, and has led to more insights on the subject. The study is valuable for future studies regarding the impact of human interferences and the understanding of the distribution of SPM and turbidity in the Rhine ROFI. Since the distribution of SPM is dependent on different physical processes, more insight into the hydrodynamics in the Rhine ROFI is indispensable. Here, the conclusions of this study are presented. Furthermore, the implications of the findings for the PoR and future recommendations are discussed.

Conclusions

The dataset shows that two transects, only 12 km apart, can have a distinctly different response. Before the study, it was expected that the Northern transect is mostly-well-mixed and homogeneous. However, the results presented here have demonstrated that stratification is present at this location and that it is more stratified that the Southern transect. As a result of this phenomenon the alongshore advection works in favour of stratification during ebb, when the advection is directed from the north to the south. This is not inline with expectations beforehand based on De Boer et al. (2008), where it is expected that the alongshore advection works in favour of stratification from south to north,during flood. Whether or not the Northern transect is always more stratified than the Southern transect cannot be concluded from a measurement campaign of 13 hours. More research is needed in order to gain a better understanding what is happening and why North is more stratified than South.

Furthermore, the ROFI alternates between mixing and weak stratification. The tidal analysis shows the presence of tidal ellipses at both transects, with an ellipticity of 0.1. An ellipticity of 0.1 is small, but around spring tide an ellipticity of zero is expected. So, according to the ellipses the situation is close to spring tide, but weak stratification is observed. Another explanation is that the weak offshore wind and freshwater discharge from the North Sea Channel at IJmuiden enhanced this weak stratification. The onset and breakdown of stratification, and the sense of rotation of the ellipses is in accordance with tidal straining theory.

The simplified three-dimensional PEA equation appears to be a good method to obtain insight into the contribution of the different processes inducing stratification. This is the second time this equation has been used on data (Smolders, 2011) and the first time it is used with cross- and alongshore information. As expected, cross-shore straining dominates. However, the other processes also have significant influence on stratification and cannot be neglected. This analysis showed that alongshore straining and advection do not only occur in the bulge region but also in the river plume far downstream.

The PoR is interested in the impact of their dredging activities and the construction of the Maasvlakte 2 on the distribution of SPM in the Dutch coastal zone. This study led to an improved knowledge regarding the processes controlling the stratification and the current structure of the Rhine ROFI. Here, the data showed that the system near Egmond and Wijk aan Zee generally responds as expected. However, unexpected behaviour is observed as well, which shows that the Rhine ROFI is very dynamic and variable, making the system difficult to predict. The knowledge acquired during this research can be used to analyse the other data from the large scale dataset (see Appendix B). In addition, this study can be used as a building block for future research regarding the distribution of SPM. An important next step for PoR will be to couple the hydrodynamics with the observed SPM distribution.

Recommendations

The data was obtained by two different instruments. Therefore, a calibration between the sensors of PoR and NIOZ was performed on site. However, this calibration was not very accurate because of the specific field conditions and the sensitivity of the OBS sensor. For future research it is recommended to calibrate the different instruments within the laboratory. In that case both instruments have exactly the same conditions.

The change of φ in time is calculated from the data and is compared with a simplified form of the three-dimensional PEA equation, in which only the advection, straining and mixing are remained. The mixing term contains an assumption for wind, wave and tidal stirring. Differences between the change of φ in time and the simplified three-dimensional energy anomaly equation are observed, which can be ascribed to the simplification of the three-dimensional equation and the discretization method chosen to calculate the different terms. However, both follow the same trend. This approach allows us to obtain a qualitative insight into the different processes and to determine which are the most important processes. Therefore, it is a useful method for a first analysis of the system. For further research a closer look to the simplification and the discretization method is advised. In addition, the current analysis with the two vessels can be improved in future work by displaying the data on z-layers.

What is discovered with the two transects, is at the limit of what is possible with two vessels available to the Dutch community. The data shows that measuring the dynamic variability of the plume with vessels is not so straightforward. The plume changes significantly during the time it takes to complete one transect, which leads to large effects on the discretization method chosen. This results in effects on the PEA analysis. In addition, the resolution in time is very small, since the transects are sailed only eight times with about one and a half hour between each track. To get the synoptic of the response of the plume, more measurements are needed, both at a higher frequency and over a longer period of time. It is recommended that Therefore, for future research it is recommended to use a couple of fixed moorings. A couple of fixed moorings would provide a continuous signal in time and space. From which alongshore and cross-shore response can be determined. Furthermore, some data that could affect the analysis is missing. Therefore, applying different analysis processes may lead to a slightly different interpretation. For a general understanding of the area further research is recommended.

Appendix A

Mathematical support

A.1 Steady-state equations/Navier-Stokes Equations

The Navier Stokes Equations are the basic equations governing fluid dynamics. These equations are derived from Newton's Second Law and the principles of mass and energy conservation. The continuity equation for an incompressible fluid, i.e. fluid particles move without a change in density, can be expressed as

$$\frac{\partial u}{\partial x} + \frac{\partial v}{\partial y} + \frac{\partial w}{\partial z} = 0 \tag{A.1}$$

The momentum equations, using the f-plane approximation and discarding the Coriolis term in the z direction, can be defined as follows

$$\frac{\partial u}{\partial t} + u\frac{\partial u}{\partial x} + v\frac{\partial u}{\partial y} + w\frac{\partial u}{\partial z} = -\frac{1}{\rho}\frac{\partial p}{\partial x} + fv + \text{other forces} \tag{A.2}$$

$$\frac{\partial v}{\partial t} + u\frac{\partial v}{\partial x} + v\frac{\partial v}{\partial y} + w\frac{\partial v}{\partial z} = -\frac{1}{\rho}\frac{\partial p}{\partial y} - fu + \text{other forces} \tag{A.3}$$

$$\frac{\partial w}{\partial t} + u\frac{\partial w}{\partial x} + v\frac{\partial w}{\partial y} + w\frac{\partial w}{\partial z} = -\frac{1}{\rho}\frac{\partial p}{\partial z} - g + \text{other forces} \tag{A.4}$$

The f-plane approximation assumes a constant Coriolis force within the Cartesian co-ordinate system. This approximation is used in studies where the region is in the order of 10 - 100 km.

A.2 Heaps

The steady-state equations of continuity and motion are the starting point of Heaps (1972). These equations are presented in section A.1. Heaps assumed a straight infinitely long coast with the same geometry for the sections normal to the coast. The steady-state equations of continuity and motion can be rewritten in the following form

$$\frac{\partial}{\partial x}\int_{-\zeta}^{h} u dz + \frac{\partial}{\partial y}\int_{-\zeta}^{h} v dz = 0 \tag{A.5}$$

$$-\frac{1}{\rho}\frac{\partial p}{\partial x} - N\frac{\partial^2 u}{\partial z^2} = -fv \tag{A.6}$$

$$-\frac{1}{\rho}\frac{\partial p}{\partial y} - N\frac{\partial^2 v}{\partial z^2} = fu \tag{A.7}$$

$$-\frac{1}{\rho}\frac{\partial p}{\partial z} + g = 0 \tag{A.8}$$

Where x,y and z are the Cartesian coordinates, with x in onshore direction, y in alongshore direction and z is the depth below the surface. U and v are the components of the current at depth z in the directions x and y. ρ is the density of the water and p is the pressure at any

position in the Sea. N is a coefficient of eddy viscosity and f is the geostrophic coefficient, which is equal to $2\omega\sin\varphi$. Where ω is the angular speed of the Earth's rotation and φ is the latitude. The acceleration of the Earth's gravity is denoted with g. With use of the hydrostatic pressure assumption

$$p = p_a + g\int_{-\zeta}^{z} \rho dz \tag{A.9}$$

Where p_a is the atmospheric pressure on the sea surface, considered to be constant. The alongshore dependency of y can be eliminated considering that all conditions in the cross-shore sections are identical. This elimination gives the following steady state equations of continuity and motion:

$$\frac{\partial}{\partial x}\int_{-\zeta}^{h} u dz = 0 \tag{A.10}$$

$$N\frac{\partial^2 u}{\partial z^2} = -fv + g(z+\zeta)\frac{1}{\rho}\frac{\partial \rho}{\partial x} + g\frac{\partial \zeta}{\partial x} \tag{A.11}$$

$$N\frac{\partial^2 v}{\partial z^2} = fu \tag{A.12}$$

From equation A.11 it follows that when friction is limited, the force induced by the pressure gradient can only be balanced by the Coriolis force. The flow will be deflected towards the right and results in an alongshore flow towards the north (for the Northern Hemisphere). This balance is also known as the "Thermal wind balance". When friction is the dominating force the pressure gradient is balanced by internal friction, a non-linear velocity shear. This results in a cross-shore current which is directed offshore at the surface and directed onshore at the bottom. This limit case is called "estuarine circulation". Heaps (1972) combines these two cases in equation A.11 in one residual current.

A.3 Prandle

Prandle (1982a,b) studied the vertical structure of tidal currents in seas and estuaries. He neglected vertical acceleration, convective and density terms to describe the first order tidal propagation. The equations of motion, displayed on a Cartesian grid, may be written as:

$$\frac{\partial u}{\partial t} - fv = -g\frac{\partial \zeta}{\partial x} + \frac{\partial}{\partial z}N\frac{\partial u}{\partial z} \tag{A.13}$$

$$\frac{\partial v}{\partial t} + fu = -g\frac{\partial \zeta}{\partial y} + \frac{\partial}{\partial z}N\frac{\partial v}{\partial z} \tag{A.14}$$

Where N is the vertical eddy viscosity, z is the vertical axis positive upwards, u and v are the velocities along the x and y axis respectively. The Coriolis parameter is denoted with f ,the gravitational acceleration with g, ζ is the surface elevation and ρ is the density. De Boer et al. (2006) defined two boundary conditions, based on Prandle (1982b). The linearised bottom friction is defined as $s = 8kU/3\pi E$, where k is a friction constant (Prandle, 1982b), U is the depth averaged velocity and E is a constant vertical eddy viscosity. The boundary conditions are

$$z = 0 : \frac{\partial u}{\partial z} = 0, \frac{\partial u}{\partial z} = 0 \tag{A.15}$$

$$z = -D : \frac{\partial u}{\partial z} = su, \frac{\partial v}{\partial z} = sv \tag{A.16}$$

For solving the equations a homogeneous water column with a vertically uniform eddy viscosity is assumed. For further investigation of the structure and solving the equations the current vector R can be divided into the sum of a clockwise rotating and an anti-clockwise rotating component. The pressure gradient vector G is defined in the same way, as the rotational component.

$$R = R^+ + R^- = u + iv \tag{A.17}$$

$$G = G^+ + G^- = \frac{\partial \eta}{\partial x} + i\frac{\partial \eta}{\partial y} \tag{A.18}$$

$R^{\pm}$ and $G^{\pm}$ can be defined in the complex plane as:

$$R^{\pm} = |R^{\pm}|\exp(i\phi_{\pm})\exp(\pm i\omega t) \tag{A.19}$$

$$G^{\pm} = |G^{\pm}|\exp(i\phi_{\pm})\exp(\pm i\omega t) \tag{A.20}$$

ω is the angular frequency and ϕ the phase in the complex plane. An expression for the anti-clockwise and clockwise motions is derived by substituting the definitions of R and G into equations A.13 and A.14, giving:

$$i(f+\omega)R^{+} = G^{+} + \frac{\partial}{\partial z}(N\frac{\partial R^{+}}{\partial z}) \tag{A.21}$$

$$i(f-\omega)R^{-} = G^{+} + \frac{\partial}{\partial z}(N\frac{\partial R^{-}}{\partial z}) \tag{A.22}$$

The solution for $R^{\pm}$ is assumed as $R^{\pm} = [a\exp(-\alpha z) + b\exp(\alpha z) + c]\cdot\exp(\pm i\omega t)$. When the expression for $R^{\pm}$ is divided by the depth-averaged current $\langle u\rangle = \int_{-D}^{0} u(z)dz$ (neglecting the integral over $D \pm \eta$) the following solution is obtained (De Boer et al., 2006)

$$\frac{R^{\pm}}{\langle R^{\pm}\rangle} = \frac{\cosh(\alpha^{\pm}[z-D]) - [\cosh(\alpha^{\pm}D)] - \frac{\alpha^{\pm}}{s}\cdot[\sinh(\alpha^{\pm}D)]}{-[\cosh(\alpha^{\pm}D)] + \left(\frac{1}{\alpha^{\pm}D} - \frac{\alpha^{\pm}}{s}\right)\cdot[\sinh(\alpha^{\pm}D)]} \tag{A.23}$$

where $\alpha^{\pm} = (1+i)\sqrt{(f\pm\omega)/2E} \equiv 1/\delta^{\pm}$ is the inverse of the boundary layer height. The solutions of $R^{\pm}$ can be used to define the ellipse properties:

$$\begin{aligned}
A_{major} &= |R^{+}| + |R^{-}| && \text{Major axis}\\
A_{minor} &= |R^{+}| - |R^{-}| && \text{Minor axis}\\
\psi &= \frac{1}{2}(\phi_{-} + \phi_{+})| && \text{Inclination}\\
\phi &= \frac{1}{2}(\phi_{-} - \phi_{+})| && \text{Phase}\\
E = \frac{A_{minor}}{A_{major}} &= \frac{|R^{+}| - |R^{-}|}{|R^{+}| + |R^{-}|} && \text{Ellipticity}
\end{aligned} \tag{A.24}$$

where A_{major} is the major axis of the ellipse, A_{minor} is the minor axis, ψ is the inclination of the maximum current with the horizontal axis, φ is the phase and E is the ellipticity. According to Souza and Simpson (1996) the ellipticity can be defined by the ratio between the minor and major axis. When the ellipse is degenerated the ellipticity is zero. For a clockwise (i.e. anti-cyclonic) circular rotation the ellipticity is 1 and -1 for an anti-clockwise (i.e. cyclonic) circular rotation. Figure A.1 shows how a current ellipse can be described by two circular rotating components.

The velocity components can be written in the form of tidal constituents and the combination gives a tidal current vector describing an elliptical path. The u and v velocities can be written as follows:

$$u = a\cdot cos(\omega t) + b\cdot sin(\omega t) \tag{A.25}$$

$$v = c\cdot cos(\omega t) + d\cdot sin(\omega t) \tag{A.26}$$

where a through d are coefficients, which can be used to define the ellipse properties when the u and v velocities are known.The ellipse properties based on a through d are determined as follows:

$$A_{major} = \frac{1}{2}|(a+d) + i(c-b)| + \frac{1}{2}|(a-d) + i(c+b)| \tag{A.27}$$

$$A_{minor} = \frac{1}{2}|(a+d) + i(c-b)| - \frac{1}{2}|(a-d) + i(c+b)| \tag{A.28}$$

$$\psi = \frac{1}{2}\arg\left(\frac{1}{2}[(a+d) + i(c-b)]\right) + \frac{1}{2}\arg\left(\frac{1}{2}[(a-d) + i(c+b)]\right) \tag{A.29}$$

$$\varphi = \frac{1}{2}\arg\left(\frac{1}{2}[(a+d) + i(c-b)]\right) - \frac{1}{2}\arg\left(\frac{1}{2}[(a-d) + i(c+b)]\right) \tag{A.30}$$

$$E = \frac{A_{minor}}{A_{major}} \tag{A.31}$$

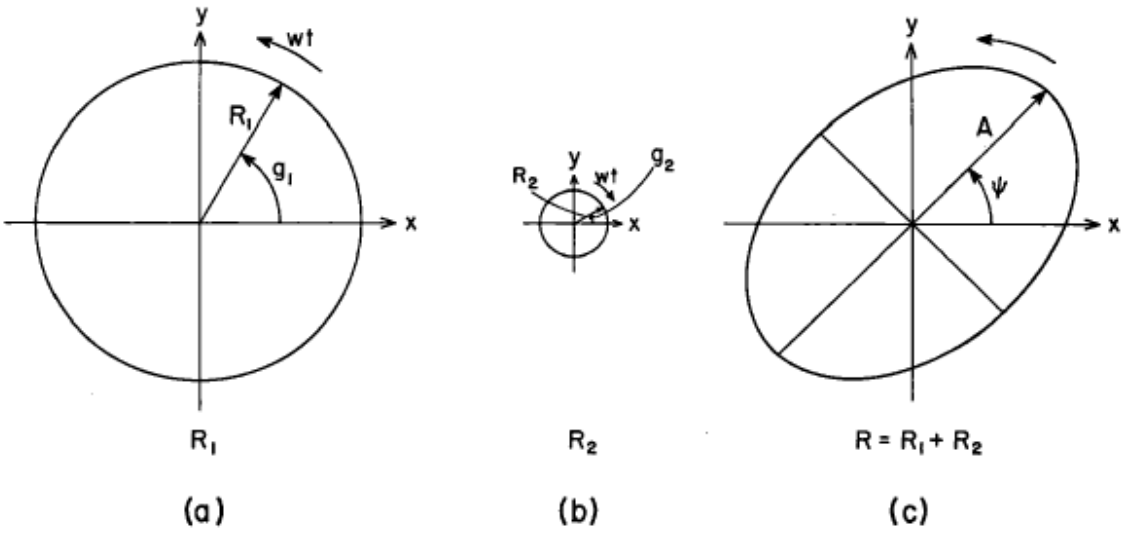

Figure A.1: Current ellipse component consist of (a) an anti-clockwise (i.e. cyclonic) component,(b) a clockwise (i.e. anti-cyclonic) component, (c) the resultant ellipse (Prandle, 1982a)

.

A.4 Wave Theory

Section 2.6 explains the general and most relevant information about waves and their impact. Within this section the mathematical background and derivations of equations is reviewed. Different theories, equations and views are derived about waves during the past years. As explained earlier, waves play an important role in stirring up sediments and causing current motions which transport these sediments. The most simple form of water waves are regular, monochromatic, waves. The waves are mutually identical. When the wave length is much (GIVE PROPORTION,FORMULA!!) larger than the wave height, the waves approximate a sinusoidal form. In this case linear wave theory can be used for the determination of the wave properties, which is more straightforward to use than non-linear theory. Sea-waves are irregular and a spectrum of waves with different heights, periods and directions are observed. The wave data for this study is obtained from Rijkswaterstaat (www.waterbase.nl). These data contain locally-generated irregular waves, common in the North Sea. Important for the stirring of sediment by waves is the orbital velocity at the sea bed induced by waves propagating in shallow water. For shallow water determined as

$$h < 0.1gT^2 \tag{A.32}$$

Were h is the local water depth, T is the wave period and g is the gravitational acceleration. Non-breaking waves are assumed. Within this research the procedure for non-linear waves by Soulsby were analyzed.

Non-linear Wave Theory

The wave data contains irregular waves, therefore the assumption is made that the waves correspond to the JONSWAP spectrum. This is a widely used wave spectrum and based on many wave measurements in the North Sea. With use of this assumption, Soulsby (1997) derived a procedure to compute the orbital velocity and bed shear stress for irregular sea waves. This procedure is used in this section. The orbital velocity is calculated first followed by determination of the bed shear stress due to waves. The JONSWAP curve is used to obtain the standard deviation of the bottom orbital velocity (U_{rms}) beneath a JONSWAP spectrum. The U_{rms} is used for determination of the bottom orbital velocity amplitude U_w. First the significant wave height H_s, the zero crossing

period T_z and the local water depth h are obtained. With these quantities the value $T_n = (h/g)_{1/2}$ is calculated and therefore the fraction T_n/T_z can be determined. T_n/T_z in combination with the JONSWAP curve (Soulsby (1997), page 73 figure 14) gives the value of the standard deviation of the bottom orbital velocity U_{rms}. The bottom orbital velocity is derived by

$$U_w = \sqrt{2} U_{rms} \tag{A.33}$$

The next step is to calculate the wave bed shear-stress τ_w. With the use of the orbital velocity U_w and a wave friction factor f_w the bed shear stress can be obtained:

$$\tau_w = 0.5 \rho f_w U_w^2 \tag{A.34}$$

The wave friction factor has to be determined and depends on the flow, if it is laminar, smooth turbulent or rough turbulent. The type of flow depends on the wave Reynolds number R_w and the relative roughness r. The bed is assumed to be flat, without ripples. For a rough turbulent flow the rough bed friction factor can be determined by

$$f_{wr} = 1.39 (\frac{A}{z_0})_{-0.52} \tag{A.35}$$

with $A = U_w T / 2\pi$ and $z_0 = k_s/30$. The smooth friction factor can be obtained with the use of

$$f_{ws} = B R_w^{-N} \tag{A.36}$$

Where the wave Reynolds number can be derived by $R_w = \frac{U_w A}{\nu}$ and B = 2, N = 0.5 for laminar flow, B = 0.0521, N = 0.187 for smooth turbulent flow. The bed shear stress due to waves can now be calculated. For the friction factor f_w the largest value of f_{wr} and f_{ws} is used.

Mixing Energy Waves

The mixing energy caused by waves is of interest for the Potential Energy Anomaly equation, and thereby for the effect of waves on the state of the water column. Smolders (2011) derived an equation for the mixing energy due to waves. This equation is based on the bed shear-stress and the dispersion rate U_w/h. He applied the same coefficient for mixing efficiency as for the mixing energy due to tidal current. The derived equation for wave mixing energy is

$$\frac{\partial \phi_{waves}}{\partial t} = \tau_w \epsilon \frac{U_w}{h} = 0.5 \rho f_w \epsilon \frac{U_w^3}{h} \tag{A.37}$$

The derived equation by Smolders (2011) is used in this study for mixing energy due to waves.

Waves and Currents

In coastal regions, both waves and currents play an important role with respect to sediment dynamics. The combination is used in this study for determining the movement of fine sediment, which can be helpful for the analysis of the SPM distribution. Many different theories are derived for the combined interaction. The method of Soulsby (1997) is used here. The mean bed shear stress is used to derive the current-wave bed shear stress.

$$\tau_m = \tau_c (1 + 1.2 ((\frac{\tau_w}{\tau_c + \tau_w})^{3.2})) \tag{A.38}$$

$$\tau_{cw} = \sqrt{\tau_m^2 + \tau_w^2} \tag{A.39}$$

Appendix B

Snapshot of the entire dataset of the Port of Rotterdam Authority

Different mechanisms in the Rhine ROFI affect each other (see figure 1.3). Straight forward relations therefore are not simple to formulate. The large-scale dataset of PoR within the Rhine ROFI is utilised to find more information on the relation between these different hydrodynamic processes in the Dutch coastal zone. First an overview of all the data is made. The data is analysed by plotting it as scatter plots. These scatter plots clearly show that different processes are involved and that clear relations are complex.

B.1 Scatter Plots

Scatter plots are made as a first exercise with the dataset. The data points are divided into five different areas. This breakdown yields a more optimal interpretation of the scatter plots. These areas are respectively, (a) the most northern area located north of IJmuiden, (b) the area between IJmuiden and Katwijk, (c) the area between Katwijk and Hoek van Holland, (d) the area around the mouth of the Rotterdam Water way and (e) the area offshore Zeeland. Figure B.1 presents the different locations. The variables used for the scatter plots are divided in two categories, the dependent and independent variables. The dependent variables are the relative density difference, the Potential Energy Anomaly(PEA) and suspended particulate matter (SPM). These variables are expected to be dependent on the location, the depth, the wave height, the wind speed, wind direction and the tide, as explained in chapter 1 and 2. The SPM distribution is influenced by stratification. Therefore the SPM distribution is dependent on the relative density difference and the PEA.

Independent	Dependent
Location	Relative density difference
Depth	PEA
Wave height	SPM
Wind direction	
Wind speed	
Tide	

Table B.1: Dependent and independent variables

The derived scatter plots do not show distinct relations between the different dependent and independent variables. The plots show a complex area where different factors are influencing the hydrodynamics. An explanation could be the choice of the simple variables, e.g. the significant wave height or the tidal envelope. General relations are visible in certain plots. These plots and relations are presented and discussed. The PEA is chosen as a dependent variable, it is determined

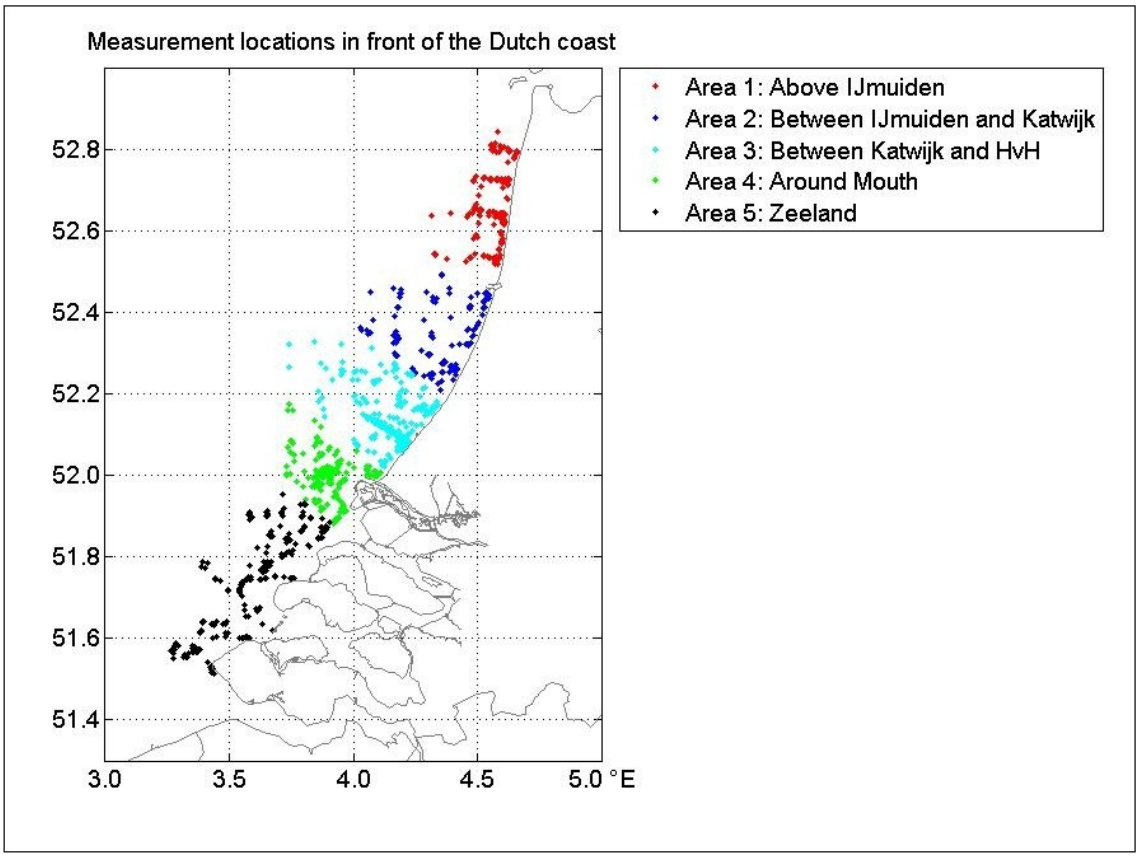

Figure B.1: Measurement locations in front of the Dutch coast divided in five different areas.

from the density. This variable gives a good indication about the state of the water column. It is in line with the relative density difference and salinity difference. Sometimes this parameter gives a more distinct view.

Unexpected points are observed in the scatter plots, e.g. "outliers". These strange points can be attributed to different causes. The location of the measurement is an important cause, e.g. the coastal zone of Zeeland is a different area than the Rhine estuary or the northern area. The deviation of the different areas, explained above, helps to interpret the figures. The weather is another important factor, which can cause strange outliers. Weather is a seasonal factor and has a large impact on the state of the water column. During the winter storms are expected, which cause high waves and wind speeds. The response of the salinity, temperature and SPM profile is influenced by the season. Local weather conditions, unrelated to the season, have an influence as well. To improve the interpretation of the seasonal influence, the plots are made per season. The accuracy of the data can be an explanation for unexpected values as well. Using measurement devices some errors and deviations can be expected.

The largest density differences are observed around the river mouth and northwards close to the coast, i.e. area 4 and 3. A density difference stands for vertical stratification, large density differences cause larger vertical stratification. The density differences and the salinity distribution are presented in figure B.2. It shows the presence of the freshwater plume. This figure, together with figure B.3 (upper left panel), show that the river outflow turns right, due to Coriolis, and extends northwards. Resulting in the form of a bulge and a downward plume, mentioned before. Heading northwards the freshwater plume tapers off and the density differences decay. Figure B.2 (left panel) shows that horizontal salinity differences are observed. Further offshore the water density increases. The same tendency is visible going north or southwards. The scatter plot of the PEA against the depth (B.3) shows the clear distribution of stratification. The largest vertical

stratification occurs in area 3 and 4. The values are lower for area 2 and even lower for the first and fifth area. The high PEA values and density differences observed at large depth can be ascribed to the sand extraction area, located in area 4.

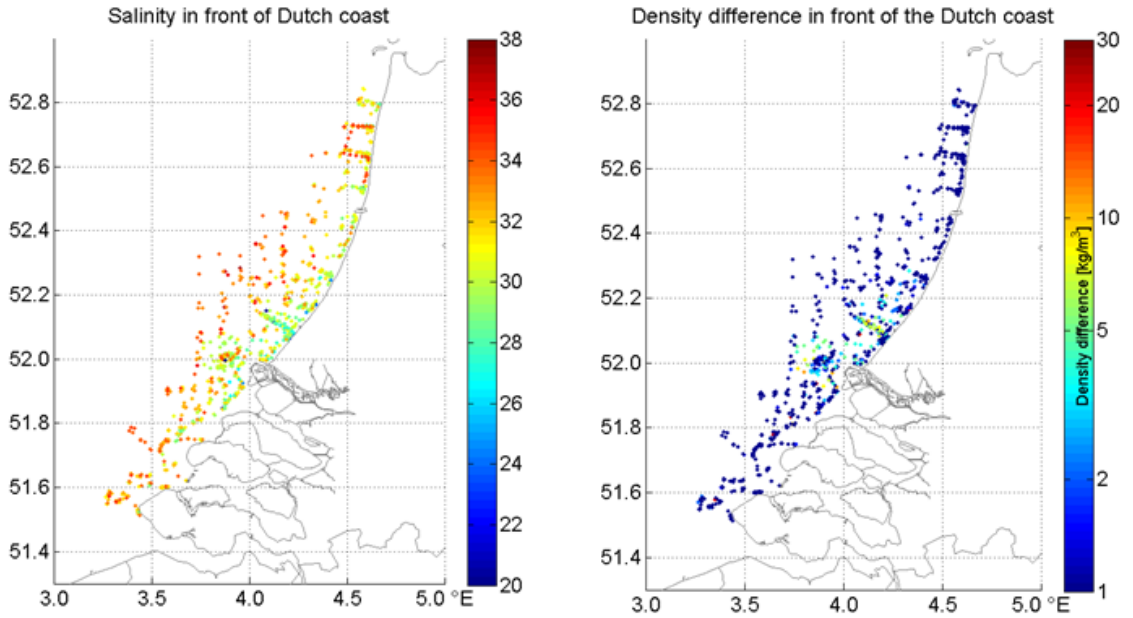

Figure B.2: The upper left panel shows the salinity in front of the Dutch coast. The upper right panel presents the relative density difference in front of the Dutch coast.

During the summer larger density differences are observed, therefore larger PEA values. One of the reasons is the heating up of the surface. During the summer solar radiation is stronger. The freshwater plume heats up during the day, resulting in a larger temperature gradient, which enhances the vertical stratification. Solar radiation and its influence on the temperature is presented in figure B.4. A negative temperature difference signifies warmer water flowing over colder water. It can be linked with the explanation in section 2.2. The ROFI has a higher temperature than the surrounding waters, during spring and summer. The warmer ROFI flows over colder surrounding water. A positive temperature difference stands for colder water flowing over water with a higher temperature. It can be explained by the fact that during the autumn and winter the freshwater plume is colder than its surroundings. Colder water flows over warmer water, due to that river water flows at higher elevation in sea, resulting in vertical stratification.

The plots doe not show a distinct relation between the significant wave height and the PEA (figure B.5). For high waves a low PEA is observed, which results in a vertically mixed water column. High PEA values occur for low waves, resulting in vertical stratification. Deviations are present naturally. The significant wave height is not a proper parameter for the influence of the waves, mixing energy due to waves is a more suitable parameter for stratification. For a North and North-East wind high values for the PEA are presented by figure B.6. The dominant wind direction, between South and West, shows high PEA values too. Vertical stratification with respect to North and North-East wind can be explained by Ekman Dynamics, pushing the surface layer offshore (see section 2.5). The freshwater plume moves offshore and gives rise to vertical stratification.

The concentration of SPM at the surface and bottom is investigated separately. The concentration of SPM in the water column fluctuates during the day caused by different processes. The interest for this research is the distribution of the SPM in vertical and horizontal sense, i.e. where is the SPM located in the water column and in front of the coast. The use of bottom and surface SPM gives a clearer view of its response. Figure B.7 (upper panels) shows high SPM values near shore

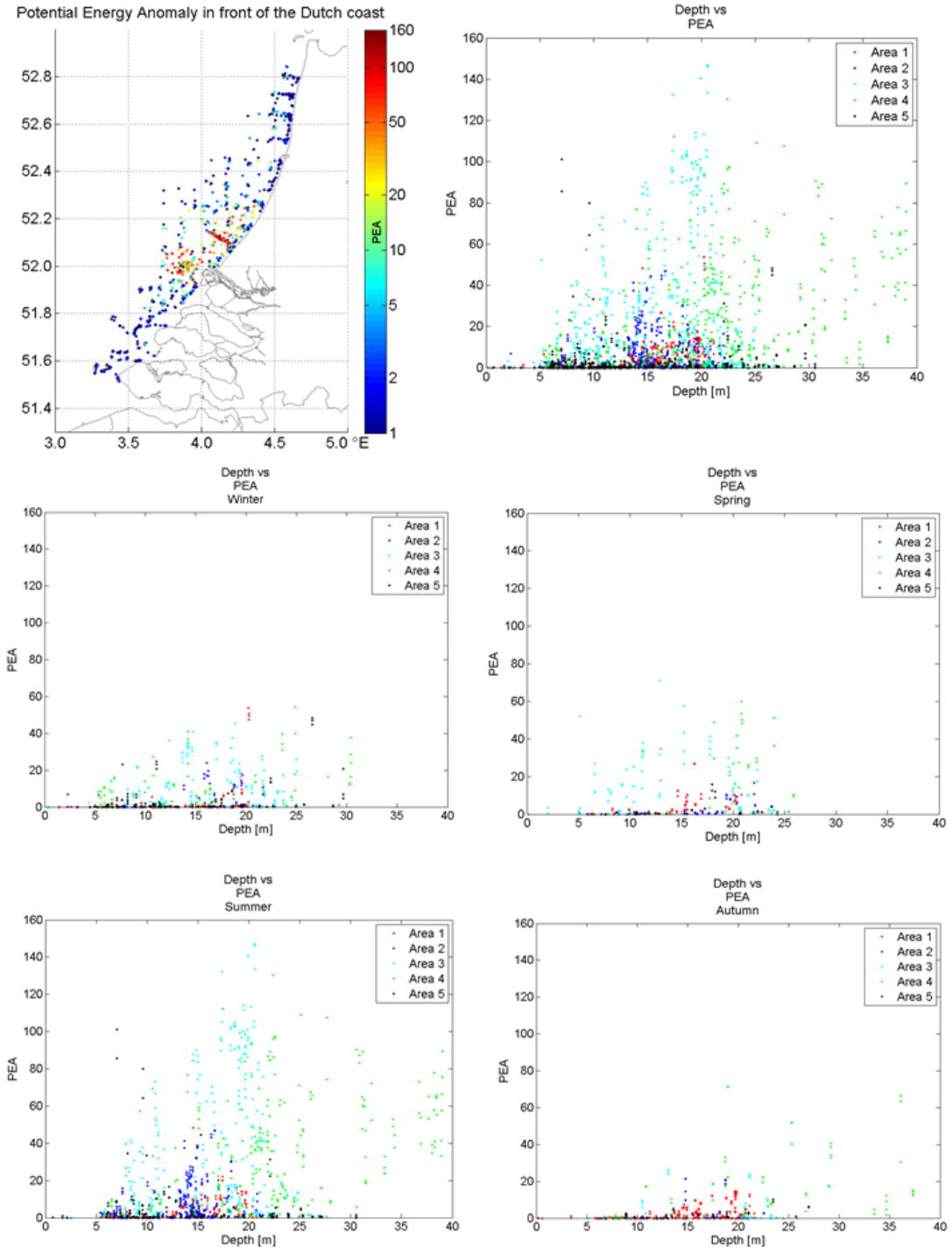

Figure B.3: The PEA versus the location and depth. The upper left panel shows the PEA in front of the Dutch coast. The upper right panel presents the PEA versus the depth. The other four panels show the PEA versus the depth per month, winter, spring, summer and autumn respectively.

and low values offshore, at the bottom and at the surface. A narrow band of high surface SPM values is observed clearly, the band is more narrow than for bottom SPM. The high values of the surface SPM range mostly from 20 - 50 mg/l, further offshore the concentration decreases from 20 to 1 mg/l. Deviation is showed with figure B.7 (middle panel on the right) where concentrations larger than 50 mg/l occur, close to the coast. The high values at 22.5 m depth occur around the

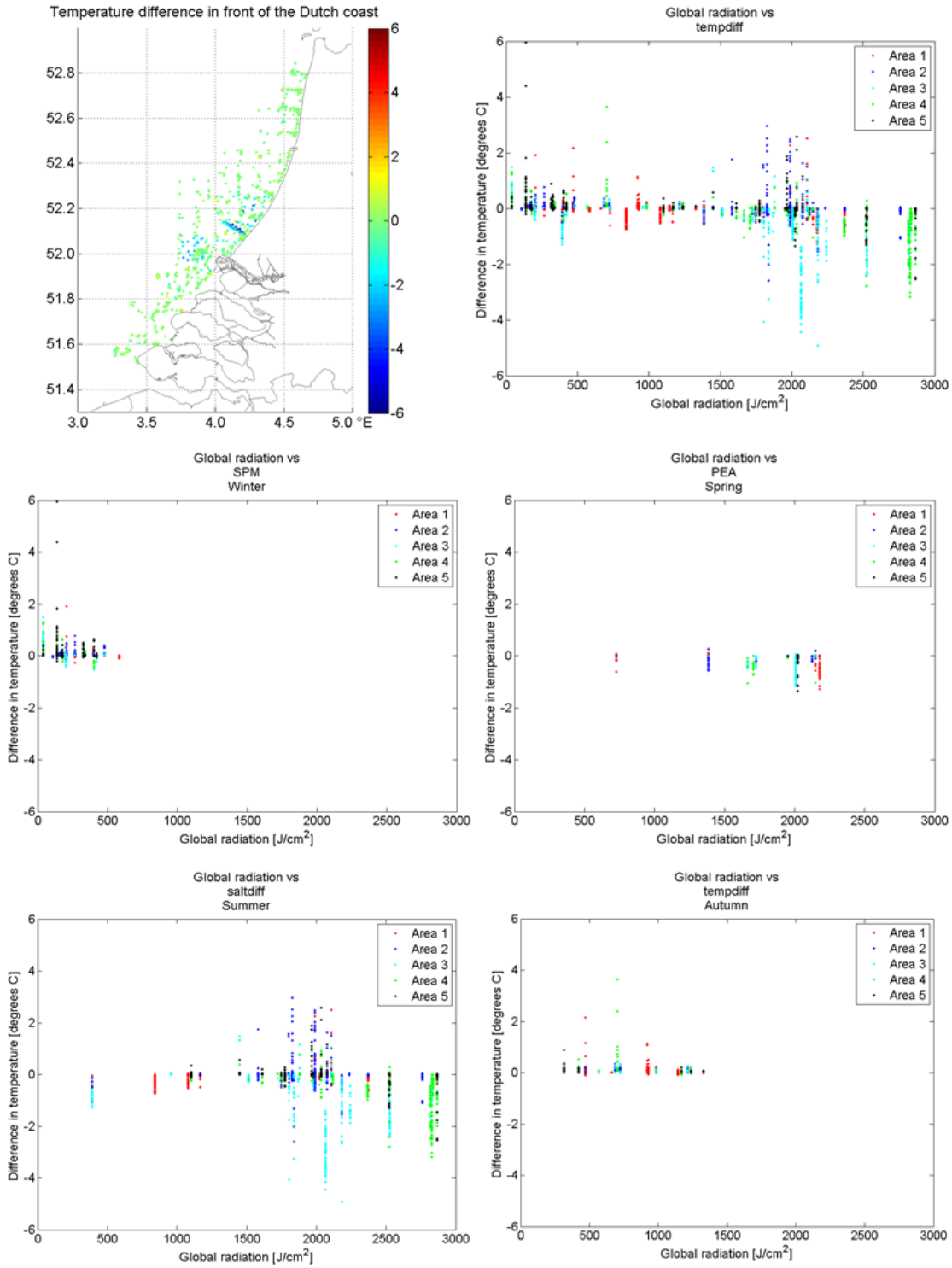

Figure B.4: The temperature difference between bottom and surface in front of the Dutch coast is presented on the upper left panel. The upper right panel shows the temperature difference versus the global radiation. The other four panels show the temperature difference versus the global radiation per month, winter, spring, summer and autumn respectively.

river mouth at Hoek van Holland, where these are expected. Whereas for the bottom SPM the high values are in the order of 100 up to 140 mg/l. Both high values occur in the northern and southern part of the study area near shore, i.e. the areas 1 till 5 all along the coast. The seasons

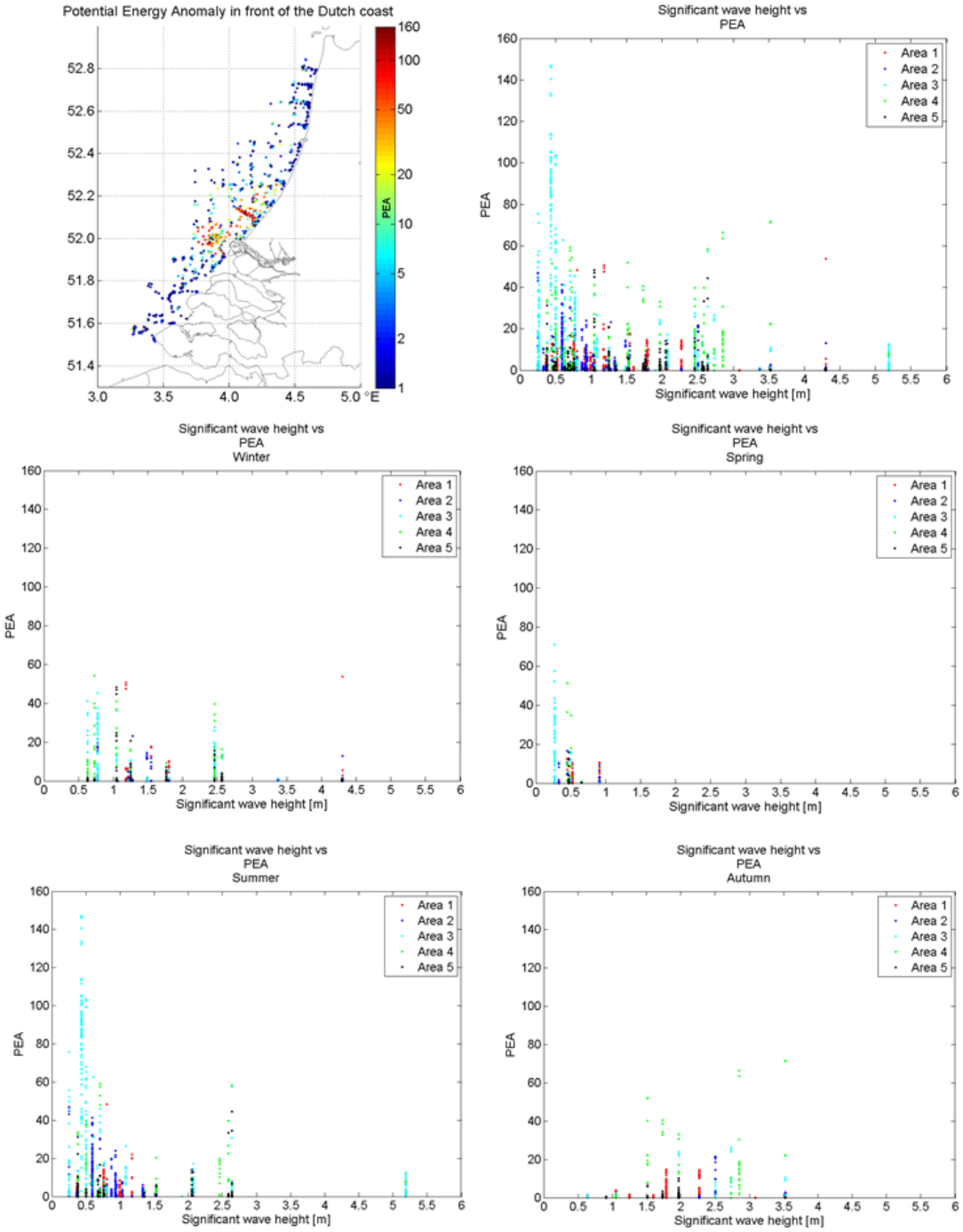

Figure B.5: The upper left panel shows the PEA in front of the Dutch coast. The upper right panel presents the PEA versus the significant wave height. The other four panels show the PEA versus the significant wave height per month, winter, spring, summer and autumn respectively.

appear to influence the amount of SPM in the water column. The high concentrations of SPM at the surface during the winter, the red dots, can be ascribed to stormy weather. In December 2009 the BRA-7 took measurements during a storm around Egmond aan Zee. Due to the heavy weather, turbulence increased, stirring up silt particles into the water column. In autumn high values near the bottom are found combined with low values near the surface. In the bottom SPM figure (figure B.7, middle panel left) a distinct line around 20 mg/l is shown. For the surface SPM there is not such a distinct line, the values are mainly lower.

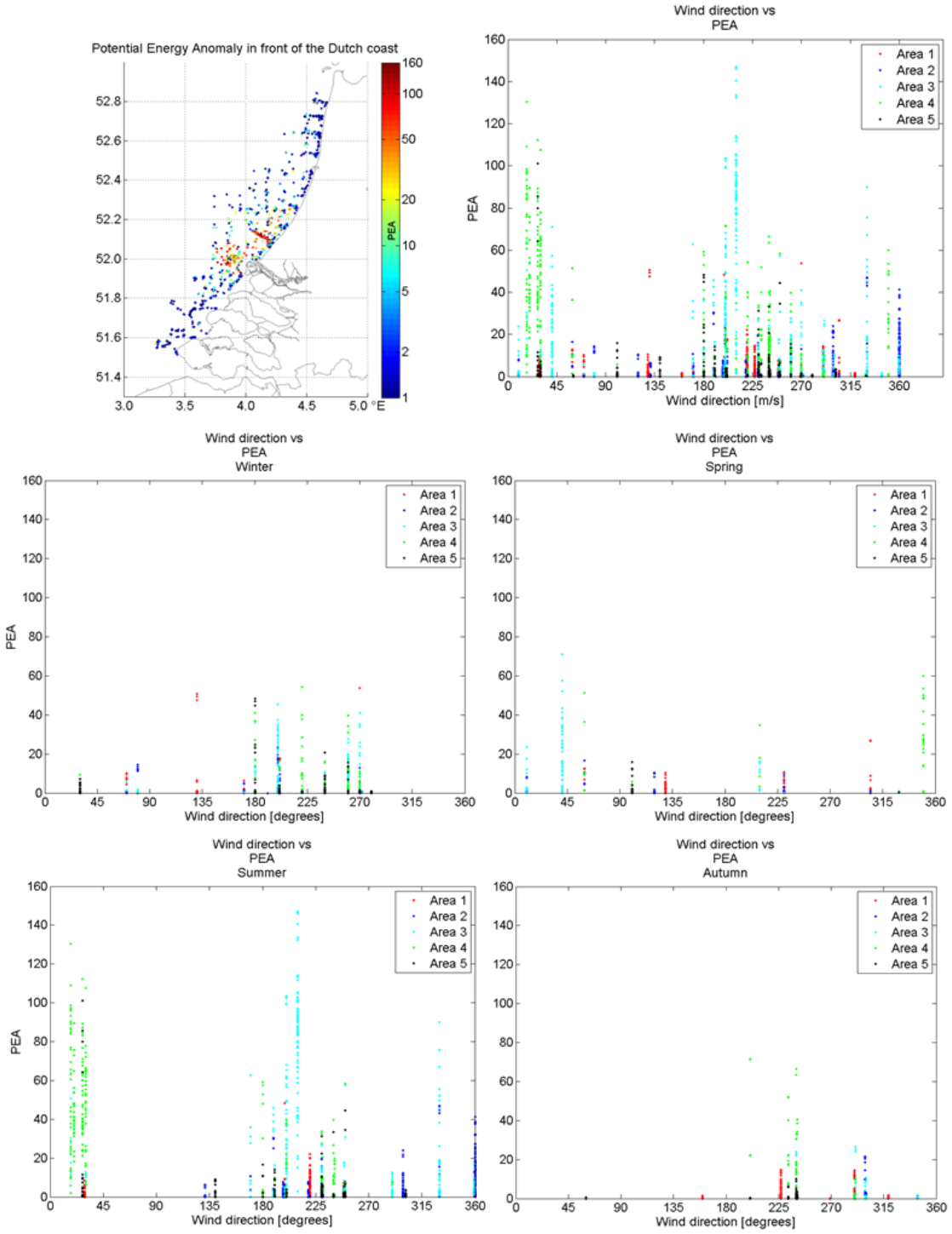

Figure B.6: The upper left panel shows the PEA in front of the Dutch coast. The upper right panel presents the PEA versus the wind direction. The other four panels show the PEA versus the wind direction per month, winter, spring, summer and autumn respectively.

The significant wave height in relation to the surface and bottom SPM does not show a distinct relation. High waves cause low and high SPM concentrations. For low waves it is the same, causing high and low concentrations. This figure clearly shows that other processes are involved and that the significant wave height is not the most proper parameter for the influence of waves on SPM.

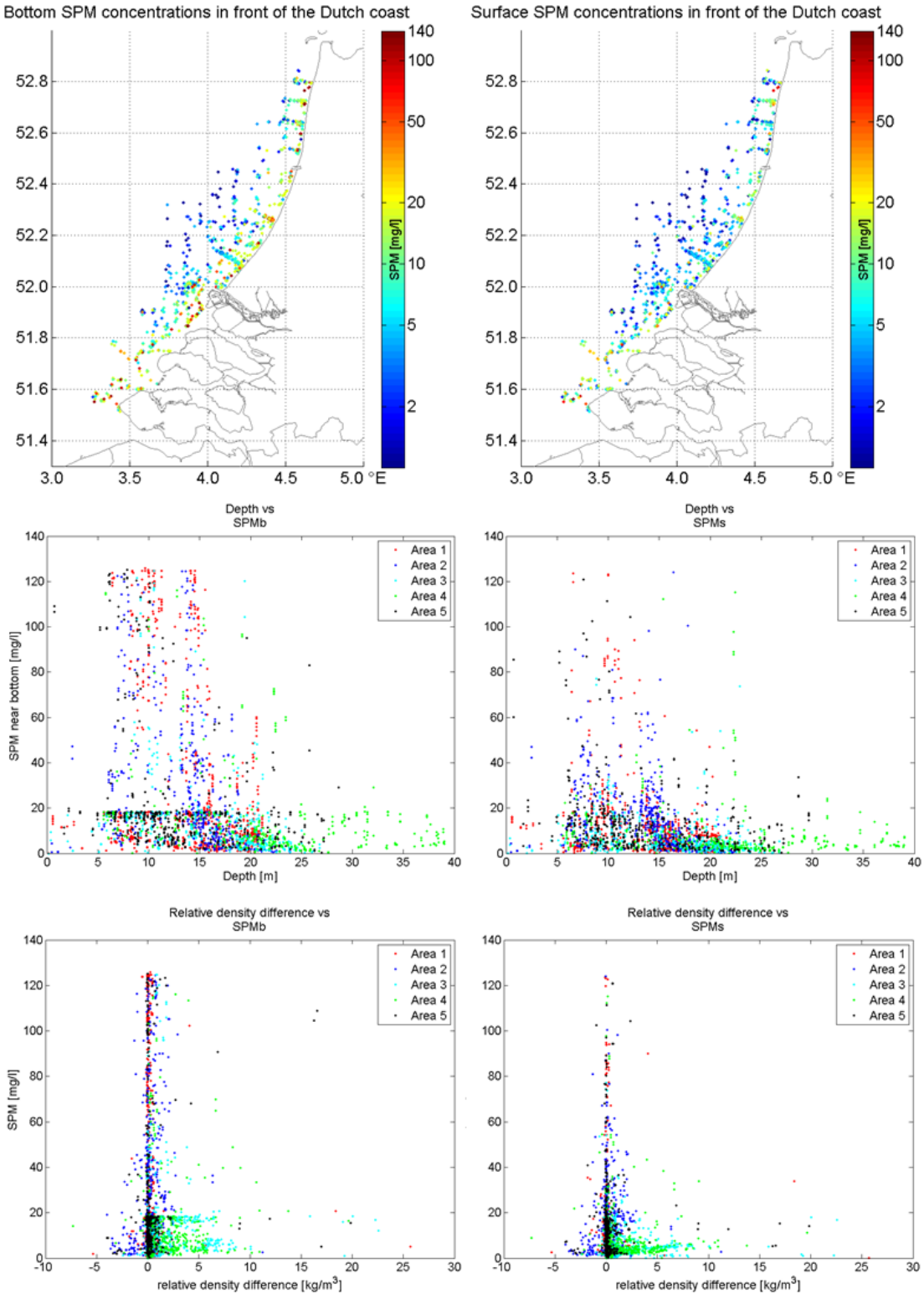

Figure B.7: The scatter plots of the bottom and surface SPM. The left panels show the bottom SPM and the right panels the surface SPM. The upper panels shows the bottom and surface SPM in front of the Dutch coast. The middle panels presents the bottom and surface SPM versus the depth. The lower panels show the bottom and surface SPM versus the relative density difference.

The density difference versus the surface and bottom SPM is presented in figure B.7 in the lower panel. It shows a relation for the surface SPM. High SPM values are found for a density difference of zero, i.e. when the water column is mixed. The SPM concentrations are low when a density difference is present, i.e. when the water column is stratified. This observation is in line with the theory explained in Chapter 1. When a pycnocline is present turbulence is suppressed and silt particles settle down. It is still possible to have silt particles above the pycnocline. For bottom SPM a slightly different result is found. High values of bottom SPM are found for situations with density differences. It is expected that during vertical stratification the concentration of silt is high near the bottom. For area 3 and 4 a cloud is observed with low concentrations near the bottom ($<$ 20 mg/l) in stratified conditions. Area 4 is the region with river outflow, enhancing stratification and turbulence. This could be an explanation for these low bottom concentration in area 4. The PEA shows the same trend for the concentrations.

Appendix C

Measurement Campaign Port of Rotterdam Aurthority

This appendix presents some pictures to get an impression about the measurement campaign of PoR. The measurements were implemented on the BRA-7, a fishing boat. Source: Port of Rotterdam Authority (O. van Tongeren and W. G. Borst).

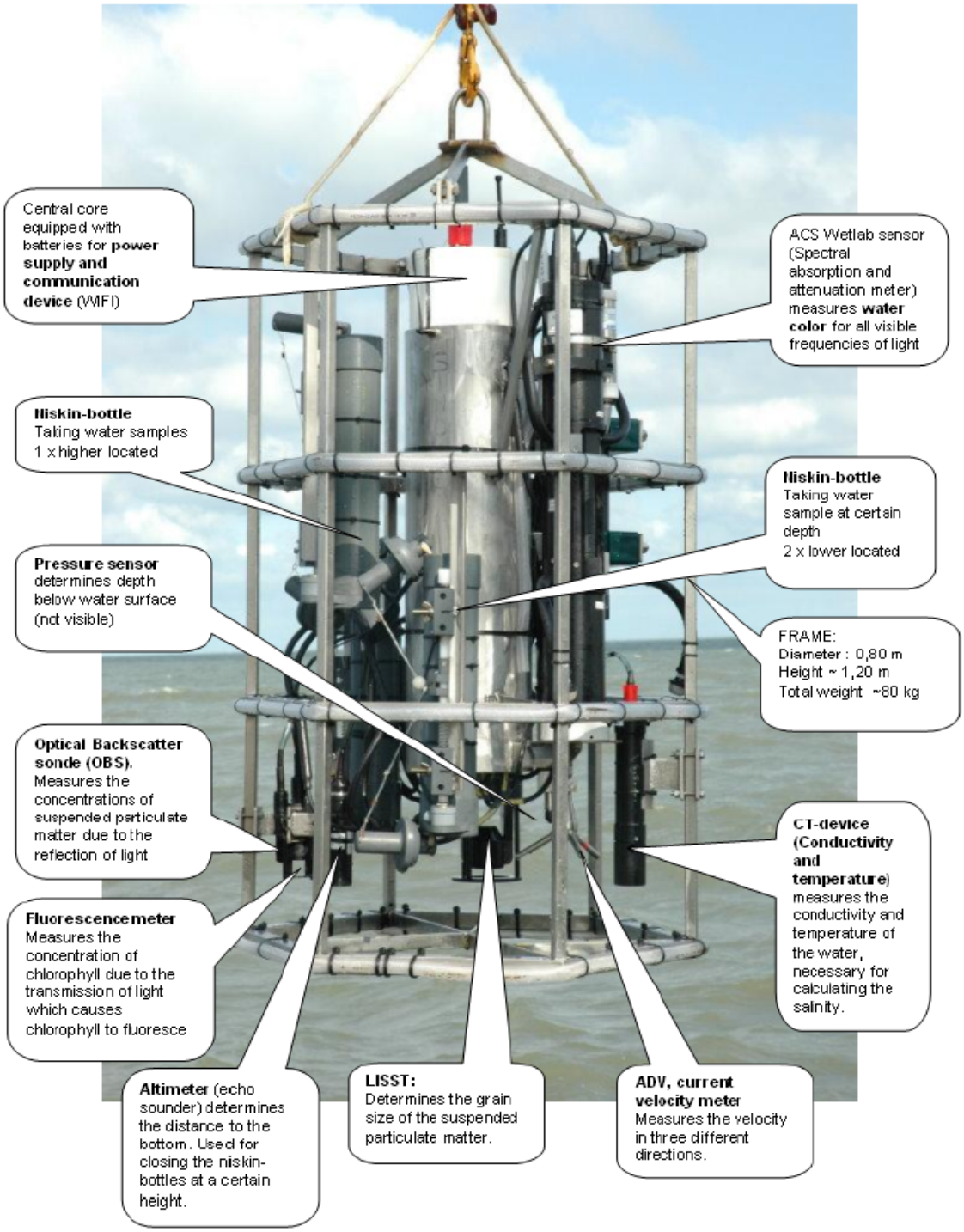

Figure C.1: The Siltprofiler of PoR with its 12 devices. A short description is given about each device.

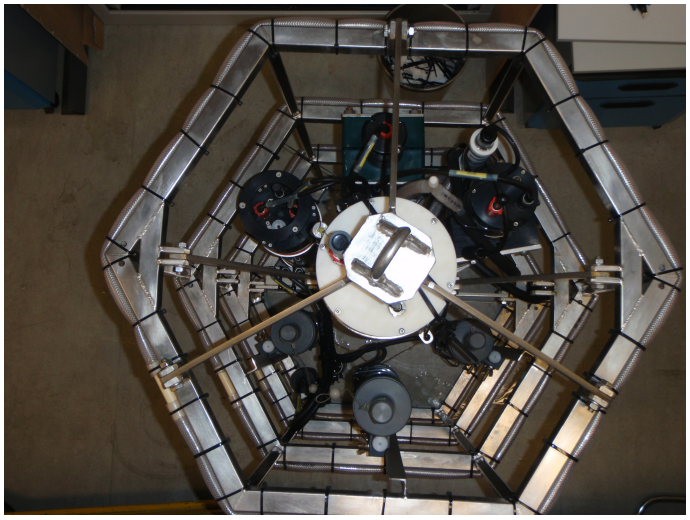

(a)

(b)

Figure C.2: The Siltprofiler of PoR during a measurement campaign. The siltprofiler (a) from above (b) above the water surface, before lowered into the water.

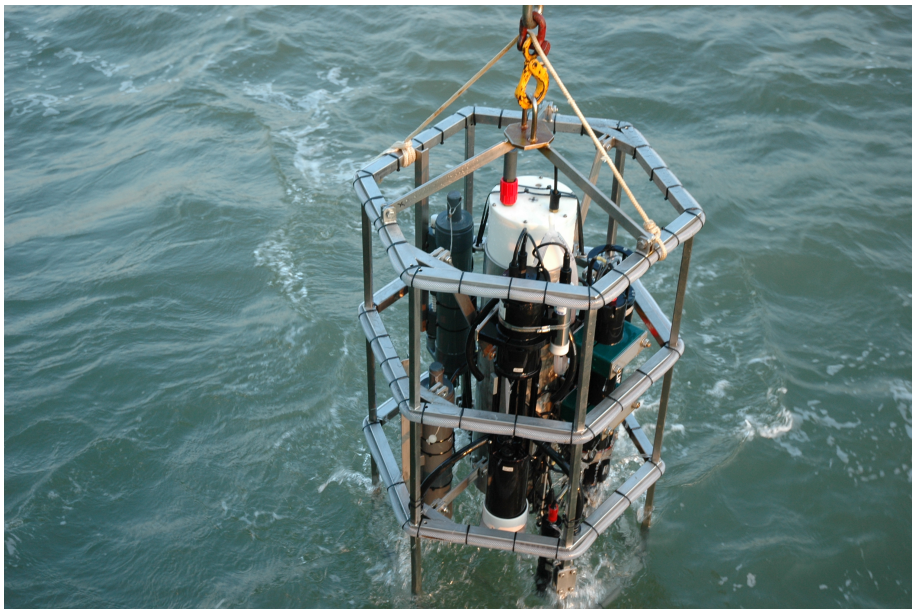

(a)

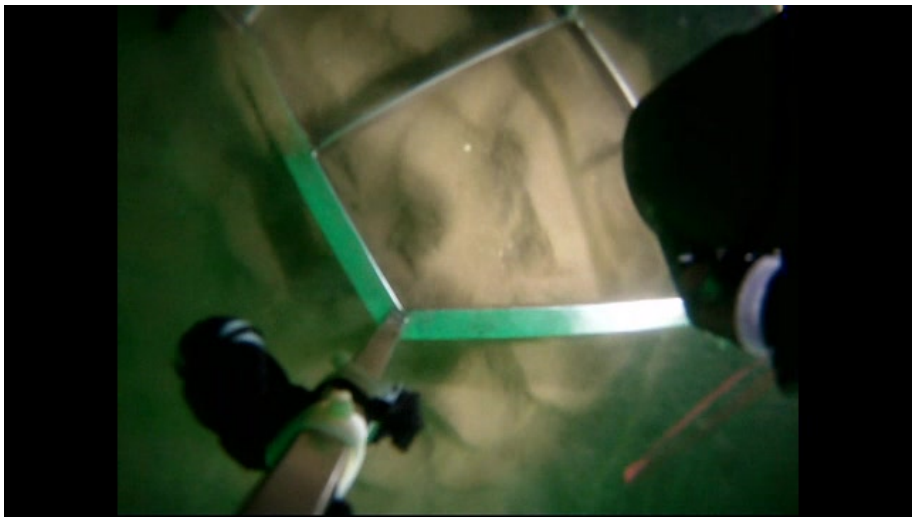

(b)

Figure C.3: The Siltprofiler of PoR during a measurement campaign. The siltprofiler (a) in the water (b) standing on the seabed.

(a)

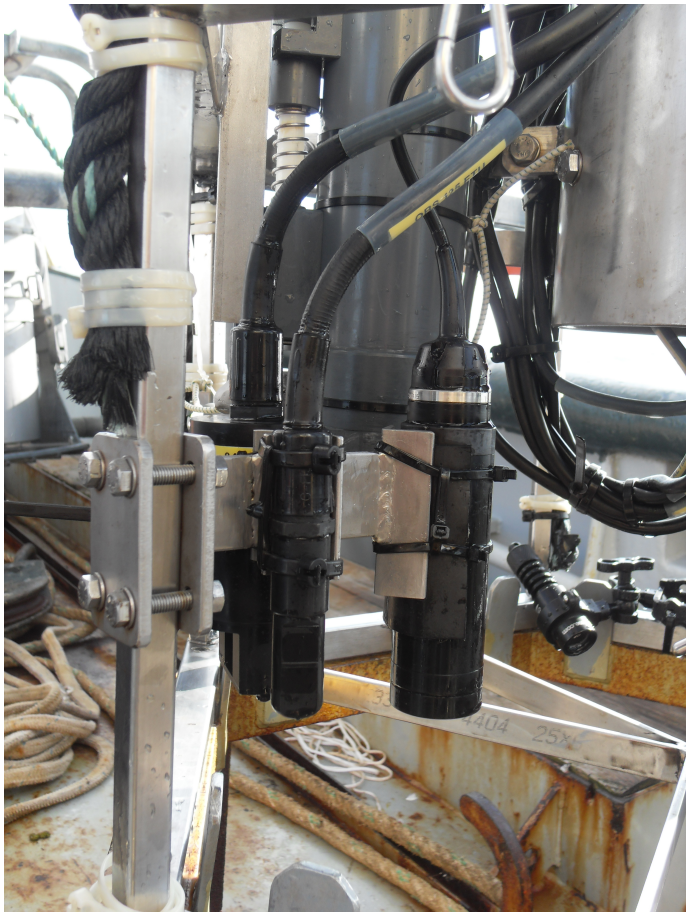

(b)

Figure C.4: The Siltprofiler of PoR during a measurement campaign. The siltprofiler (a) lifted out of the water (b) the OBS sensor on the left and the fluorescence meter on the right.

(a)

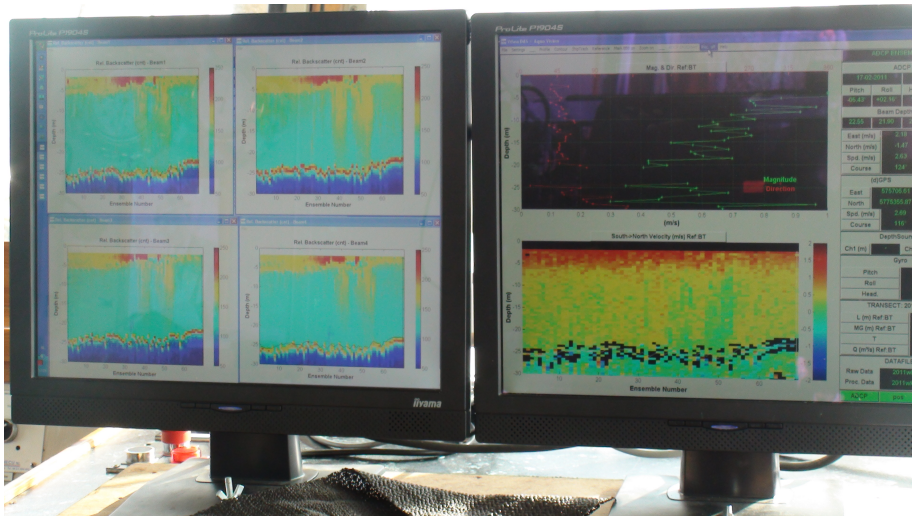

(b)

Figure C.5: (a) The laboratory on board to determine the amount of SPM from the taken water samples (b) The output on the computer during the measurement, output from the ADCP is shown on the right screen.

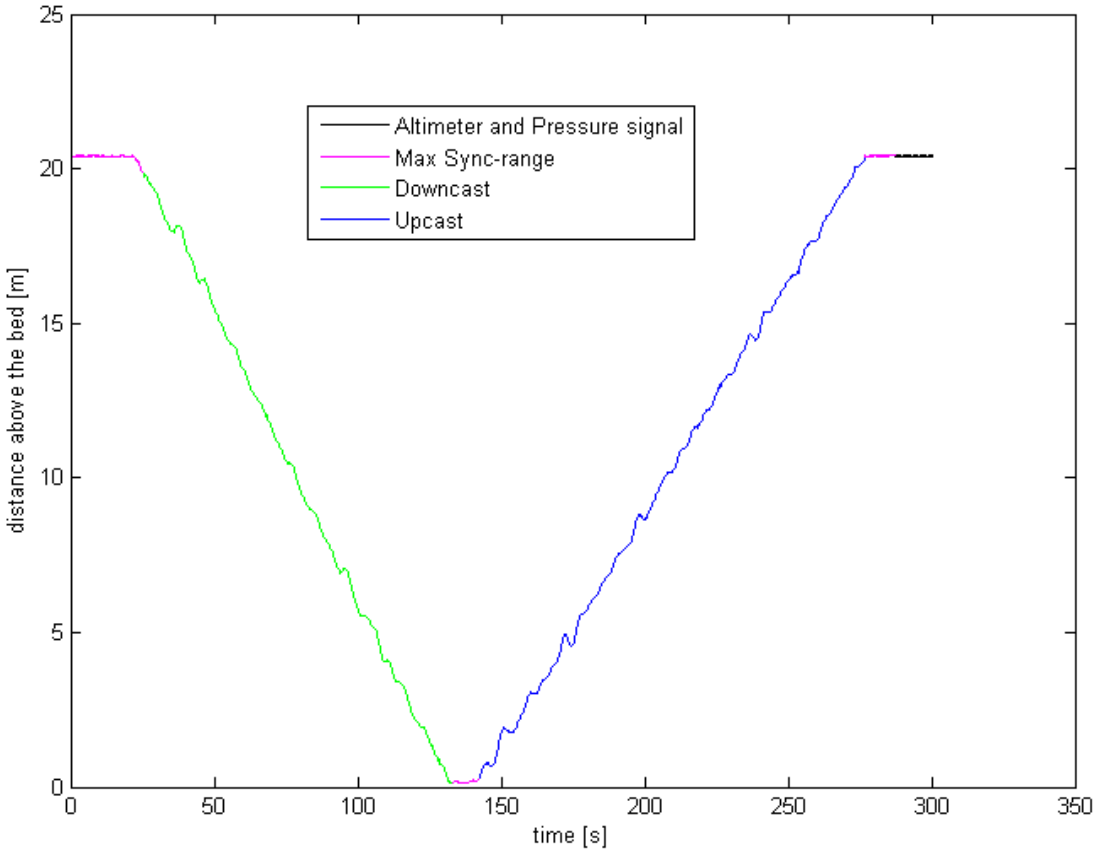

Figure C.6: The vertical trajectory of the Siltprofiler during the measurements. The time is displayed on the horizontal axis in seconds. The distance of the Siltprofiler with respect to the seabed is presented on the vertical axis in meters. The greenline is the downcast and the blue line the upcast.

Appendix D

Supporting figures

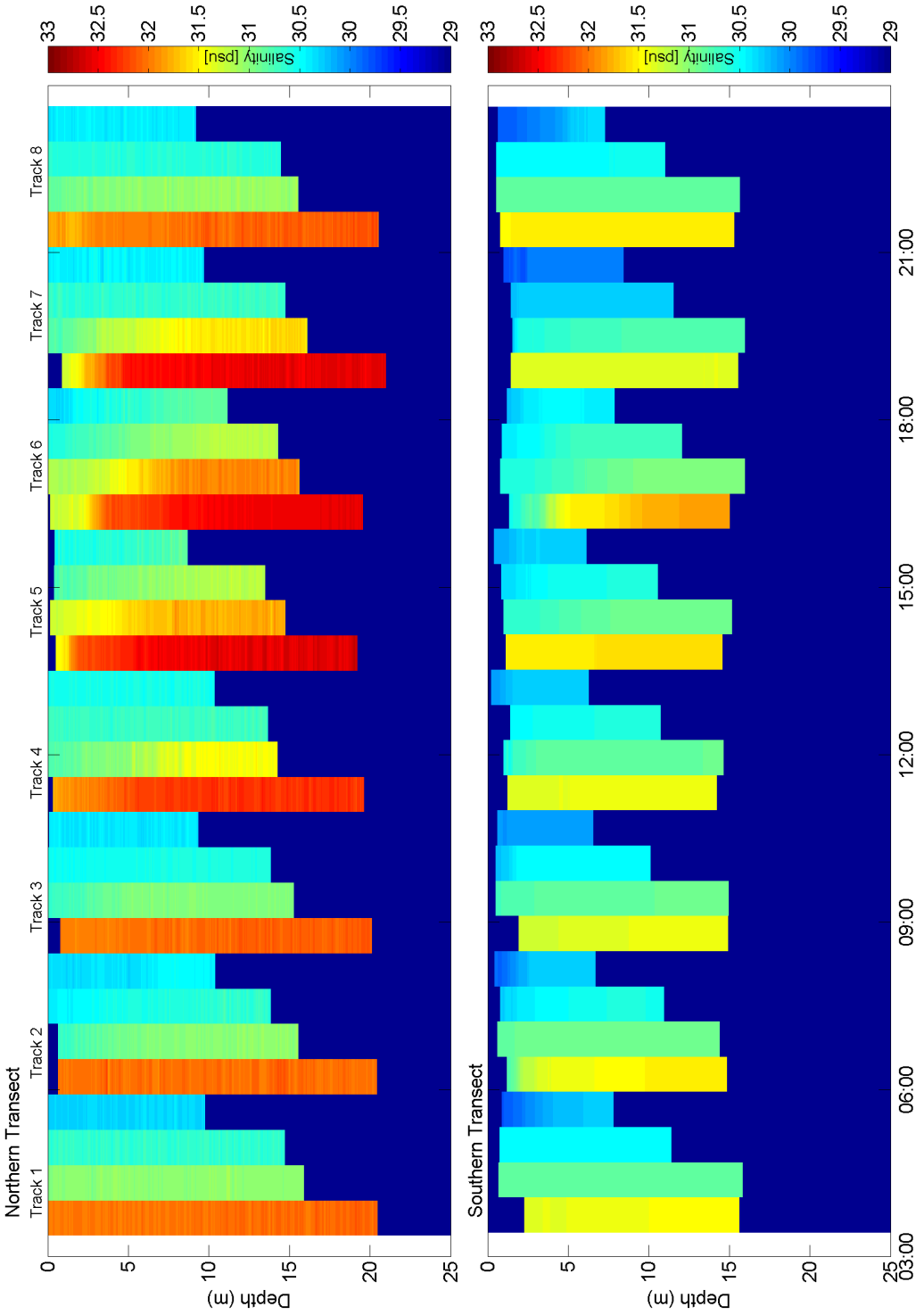

Figure D.1: Salinity profile per station from the Northern (upper panel) and Southern transect (lower panel) in time. At each station the profile is presented, for all the eight tracks.

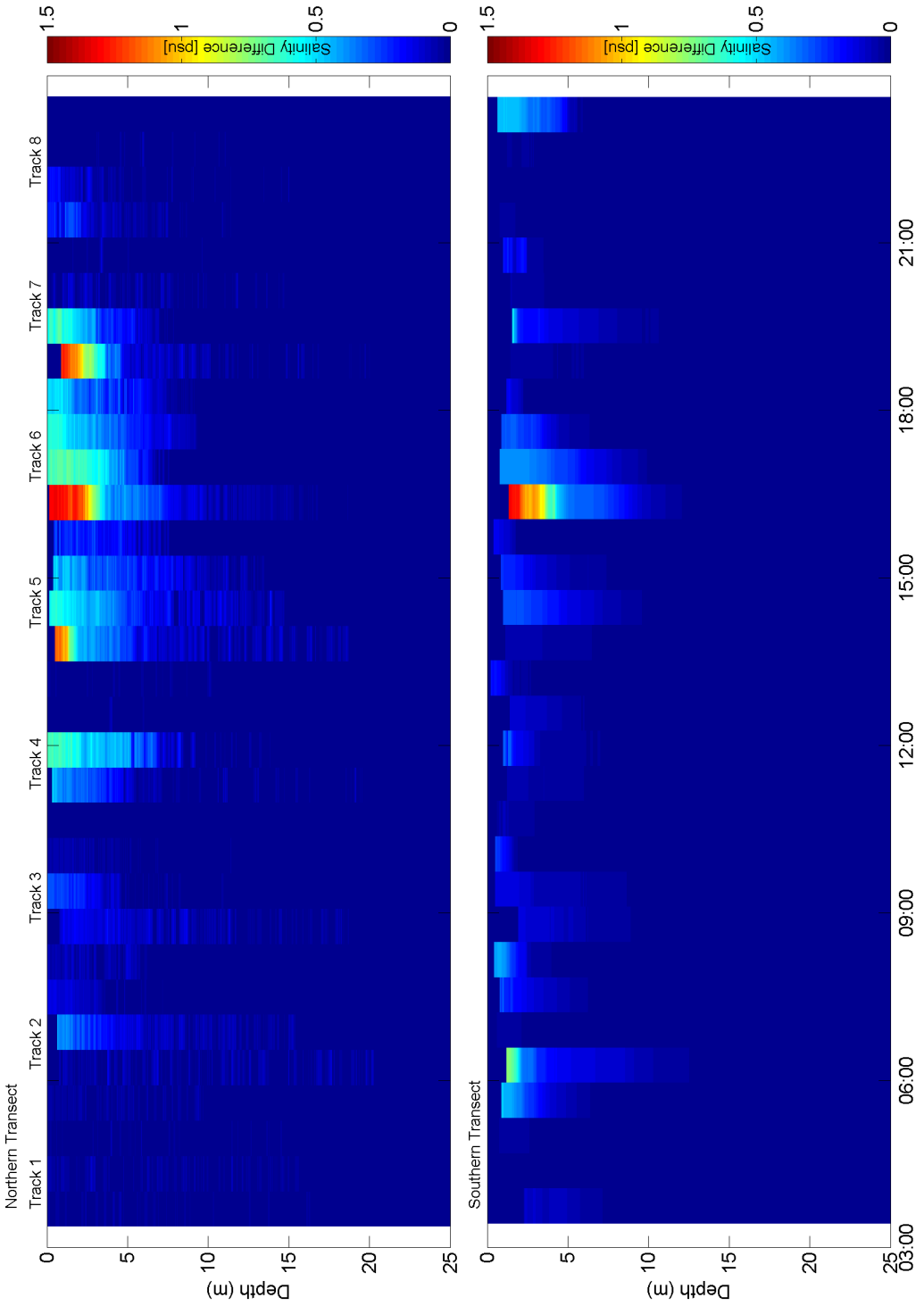

Figure D.2: Profile of the difference in salinity per station from the Northern (upper panel) and Southern transect (lower panel) in time. At each station the profile is presented, for all the eight tracks.

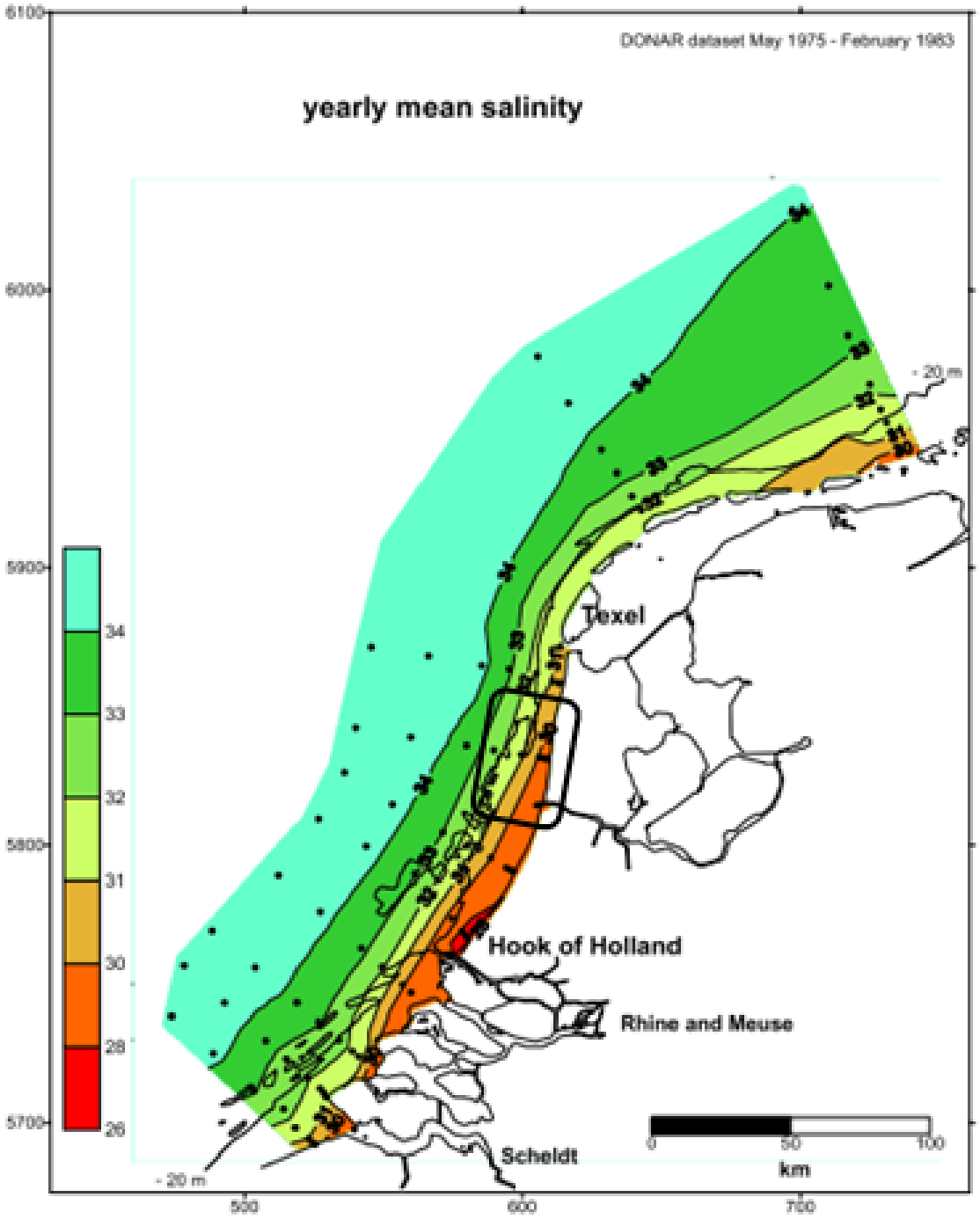

Figure D.3: Yearly mean salinity gradient (Suijlen and Duin, 2002)

Bibliography

I. Berdeal, B. Hickey, and M. Kawase. Influence of wind stress and ambient flow on a high discharge river plume. *Journal of Geophysical Research*, 2002.

J. Bosboom and M. Stive. *Coastal Dynamics I.* VSSD, 3rd edition edition, 2012. ISBN 978-90-6562-286-0.

H. Burchard and H. Baumert. The formation of estuarine turbidity maxima due to density effects in the salt wedge. a hydrodynamic process study. *Journal of Physical Oceanography*, 28:309–321, 1998.

H. Burchard and R. Hofmeister. A dynamic equation for the potential energy anomaly for analysing mixing and stratification in estuaries and coastal seas. *Estuarine, Coastal and Shelf Science*, 77: 679–687, 2008.

S. Chao. Wind-driven motion of estuarine plumes. *Journal of Physical Oceanography*, 18, 1988.

S. Chao and W. Boicourt. Onset of estuarine plumes*. *Journal of Physical Oceanography*, 16, 1986.

G.T. Csanady. *Circulation in the Coastal Ocean.* D. Reidel Publishing Company, 1982. ISBN 90-277-1400-2.

G. De Boer. *On the interaction between tides and stratification in the Rhine Region of Freshwater Influence.* PhD thesis, Delft University of Technology, 2009.

G. De Boer, J. Pietrzak, and J. Winterwerp. On the vertical structure of the rhine region of freshwater influence. *Ocean Dynamics*, 56:198–216, 2006.

G. De Boer, J. Pietrzak, and J. Winterwerp. Using the potential energy anomaly equation to investigate tidal straining and advection of stratification in a region of freshwater influence. *Ocean Modelling*, 22:1–11, 2008.

G. De Boer, J. Pietrzak, and J. Winterwerp. Sst observations of upwelling induced by tidal straining in the rhine rofi. *Continental Shelf Research*, 29:263–277, 2009.

J. De Kok. A two-layer model of the rhine plume. *Journal of marine Systems*, 8(3-4):269–284, 1996.

J. de Kok. Slibtransport langs de nederlandse kust. bronnen, fluxen en concentraties. Technical report, RIKZ, 2004. RIKZ/OS/2004.148w.

J. De Kok, C. De Valk, J. Van Kester, E. De Goede, and R.E. Uittenbogaard. Salinity and temperature stratification in the rhine plume. *Estuarine, Coastal and Shelf Science*, 53(4):467–475, 2001.

M. De Nijs, J. Winterwerp, and J. Pietrzak. The effects of the internal flow structure on spm entrapment in the rotterdam waterway. *Journal of Physical Oceanography*, 40(11):2357–2380, 2010.

M. De Nijs, J. Pietrzak, and J. Winterwerp. Advection of the salt wedge and evolution of the internal flow structure in the rotterdam waterway. *Journal of Physical Oceanography*, 41:3–27, 2011.

W. De Ruijter, A. van der Giessen, and F. Groenendijk. Current and density structure in the netherlands coastal zone. *Coastal and Estuarine Studies*, 40, 1993.

W. De Ruijter, A. Visser, and W. Bos. The rhine outflow: A prototypical pulsed discharge plume in a high energy shallow sea. *Journal of marine Systems*, 12:263–276, 1997.

M. Fettweis and B. Nechad. Evaluation of in situ remote sensing sampling methods for spm concentrations, belgian continental shelf (southern north sea. *Ocean Dynamics*, 61(2-3):151–171, 2010.

D.A. Fong and W.R. Geyer. The alongshore transport of freshwater in a surface-trapped river plume*. *Journal of Physical Oceanography*, pages 957–972, 2002.

W. Geyer. The importance of suppression of turbulence by stratification on th eestuarine turbidity maximum. *Estuaries*, 16(1):113–125, 1993.

A. Giessen, W. De Ruijter, and J. Borst. Three-dimensional current structure in the dutch coastal zone. *Netherlands Journal of Sea Research*, 25:45–55, 1990.

N. Heaps. Estimation of density currents in the liverpool bay area of the irish sea. *Geophysical Journal of the Royal Astronomical Society*, :415–432, 1972.

IOC, SCOR, and IAPSO. *The international thermodynamic equation of seawater - 2010: Calculation and use of thermodynamic properties*. UNESCO, 2010. Intergovernmental Oceanographic Commission, Manual and Guides No. 56.

J. Joordens, A. Souza, and A. Visser. The influence of tidal straining and wind on suspended matter and phytoplankton distribution in the rhine outflow region. *Continental Shelf Research*, 21:301–325, 2001.

J. Nauw and M. van der Vegt. Hydrodynamics of the rhine rofi near ijmuiden. In *Jubilee of conference proceedings NCK days 2012: Crossing borders in coastal research*, 2012.

J. Pietrzak and G. de Boer, pers. comm.

J. Pietrzak, G. de Boer, and M. Eleveld. Mechanisms controlling the intra-annual mesoscale variability of sst and spm in the southern north sea. *Continental Shelf Research*, 31:594–610, 2011.

J.D. Pietrzak and G. De Boer. On wind influence in a tidally dominated river plume, the rhine rofi. in prep.

D. Prandle. The vertical structure of tidal currents. *Geophysical and Astrophysical Fluid Dynamics*, 22:37–41, 1982a.

D. Prandle. The vertical structure of tidal currents and other oscillatory flows. *Continental Shelf Research*, 1:191–207, 1982b.

J. Simpson. Physical processes in the rofi regime. *Journal of Marine Systems*, 7963:3–15, 1997.

J. Simpson and D. Bowers. Models of stratification and frontal movement in shelf seas. *Deep-Sea Research*, 28(7):727–738, 1981.

J. Simpson and J. Hunter. Fronts in the irish sea. *Nature*, 250:404–406, 1974.

J. Simpson and A. Souza. Semidiurnal switching of stratification in the region of the rhine. *Journal of Geophysical research*, 100:7037–7044, 1995.

J. Simpson, J. Brown, J. Matthews, and G. Allen. Tidal straining, density currents, and stirring in the control of estuarine stratification. *Estuaries*, 13:125–132, 1990.

J. Simpson, J. Sharples, and T. Rippeth. A prescriptive model of stratification induced by freshwater runoff. *Estuarine, Coastal and Shelf Science*, pages 22–35, 1991.

J. Simpson, W. Bos, F. Schirmer, A. Souza, T. Rippeth, S. Jones, and D. Hydes. Periodic stratification in the rhine rofi in the north sea. *Oceanologica Acta*, 16(1):23–32, 1993.

E. Sirks. Obtaining turbulence parameters from a moving adv. Internship port of rotterdam authority, Delft University of Technology, 2012.

T. Smolders. Stratification in the rhine rofi. Master's thesis, Delft University of technology, 2011.

R. Soulsby. *Dynamics of marine sands*. Thomas Telford, 1997. ISBN 978-0-7277-2584-X.

A. Souza and J. Simpson. The modification of tidal ellipses by stratification in the rhine rofi. *Continental Shelf Research*, 16(8):997–1007, 1996.

A. Souza and J. Simpson. Controls on stratification in the rhine rofi system. *Journal of Marine Systems*, 7963(96):311–323, 1997.

A. Souza, J. Holt, and R. Proctor. Modelling spm on the nw european shelf seas. *Coastal and Shelf Sediment Transport*, 274:147–158, 2007.

J. Suijlen and R. Duin. Atlas of near-surface total suspended matter concentrations in the dutch coastal zone of the north sea. Technical report, RIKZ, 2002. Report RIKZ/2002.059.

J. Van Alphen, W. De Ruijter, and J. Borst. Outflow and three-dimensional spreading of rhine river water in the netherlands coastal zone. *Physical processes in estuaries*, pages 70–92, 1988.

C. Van der Hout, T. Gerkema, J. Nauw, and H. Ridderinkhof. Observations of narrow zone of high suspended particulate matter (spm) concentrations along the dutch coast and its temporal variation. *Continental Shelf Research*, subm.

O. van Tongeren, pers. comm.

J. Van Wiechen. Modelling the wind-driven motions in the rhine rofi. Master's thesis, Delft University of Technology, 2011.

A. Visser, A. Souza, K. Hessner, and J. Simpson. The effect of stratification on tidal current profiles in a region of fresh-water influence. *Oceanologica Acta*, 17(4):369–381, 1994.

M. Visser. *On the transport of fine sediment in the Netherlands coastal zone*. PhD thesis, Universeit of Utrecht, 1993.

M. Visser, W. de Ruijter, and L. Postma. The distribution of suspended matter in the dutch coastal zone. *Netherlands Journall of Sea Research*, 27(2):127–143, 1991.